Ultratrace Neurotransmitters SERS Sensing

UNIVERSITY OF CAMBRIDGE

Wenting Wang

Christ's College

University of Cambridge

This dissertation is submitted for the degree of Doctor of Philosophy

August 2021

In memory of my supervisor Prof. Chris Abell.

Declaration

This thesis is the result of my own work and includes nothing which is the outcome of work done in collaboration except as declared in the Preface and specified in the text. I further state that no substantial part of my thesis has already been submitted, or, is being concurrently submitted for any such degree, diploma or other qualification at the University of Cambridge or any other University or similar institution except as declared in the Preface and specified in the text. It does not exceed the 60,000 words limit, as prescribed by the Degree Committee for Physics and Chemistry.

Wenting Wang

August 2021

Abstract

Surface-enhanced Raman scattering (SERS) spectroscopy is a powerful analytical technique for ultrasensitive detection of chemicals and biomolecules. As the high sensitivity of SERS requires analytes to be in close contact with a plasmonic substrate, the detection of analyte molecules with low chemical affinity towards the substrate is thus limited, for example dopamine molecules as well as other neurotransmitters (NTs), which are the focus within this thesis. Two binding methods of NTs to SERS substrates will be covered: by Cucurbit[n]uril (CB[n]) and by Fe(III) ions. The fundamental resonance modes of NTs molecules and ultratrace NTs SERS sensing are discussed in detail. Further exploration of SERS substrates in the format of oil/water interfacial film will also be reported. The SERS application integrated with microfluidic techniques will be discussed in the final part of this thesis.

In chapter 2, a simple and efficient 'mix-and-measure' method is used to form a liquid sensing platform by Raman/SERS. The exploration of dopamine Raman/SERS sensing in water solution is covered. Dopamine is one of the important catecholamine NTs, however its concentration in body fluid system is only 0.01-1 µM, and there are many kinds of interfering substances such as amino acids, nucleic acids, glucose, therefore it is difficult to distinguish dopamine from other molecules in body fluids by conventional detection methods. Raman/SERS can identify corresponding molecules based on the characteristic peaks of substances, so is a useful method to detect dopamine or other NTs.

Firstly, dopamine Raman spectra at different pH environments is discussed. Density functional theory (DFT) calculations are carried out to help understand the dopamine molecules' chemical bonds resonance modes. Dopamine concentration series for Raman spectroscopy are carried out to determine the limit of detection (LOD) of dopamine in pure water which is measured to be in the range of 100 mM to 250 mM.

In order to improve the LOD of dopamine, the Raman signal is enhanced by SERS. Gold nanoparticles (AuNPs) were used as the SERS substrates for dopamine detection. The AuNPs assembly process, dopamine-AuNPs binding methods by either CB[n] molecules or weak binding directly by dopamine molecule to Au surface is discussed. Dopamine LOD is 1 µM for NaCl-induced AuNPs aggregates SERS, and is 0.1 to 1 µM for CB[n]-induced AuNPs aggregations SERS, which reaches the level of physiological dopamine concentration in urine.

Iron (III) is also introduced as a binding molecule for dopamine and AuNPs. Two distinct protocols ('PreNP' and 'PostNP') are compared, which differ in the steps for forming SERS sensing complexes, affecting both the LOD and the DA SERS intensities. Characterising complexation of Fe(III) and

dopamine (DA) in different pH suggests that Fe(III)DA2 dominates in PostNP detection, whilst in PreNP it is the monomeric Fe(III)DA that is seen. The dopamine LOD is 0.001 to 0.01 µM by dopamine-Fe(III)-AuNPs complex SERS, which enables one to perform fast detection of multiplexed neurotransmitters (NTs) at physiological concentrations.

In chapter 3, other NTs including Norepinephrine (NEPI), DOPA, epinephrine (EPI) and serotonin (Sero) are tested by SERS using the same complexes scheme of AuNPs-Fe(III)-NT. DA, NEPI and EPI can all reach a LOD of 1 nM, which is in the range of physiological concentration. SERO however, is less sensitive and the LOD is around 100 nM.

In chapter 4, Au nanoparticle 2D arrays are developed with the CB[n] molecules and by using NaCl, and the arrays are analysed as SERS sensing substrates in different forms. The stability of the interfacial arrays is studied in terms of the influences from AuNPs surface wettability and AuNPs/clusters sizes. AuNPs covered CB[7] or citrate tend to stay at the water/chloroform interface and show high desorption energy. AuNPs clusters assembled by CB[7] are more stable at the interface than un-aggregated single AuNPs, due to higher Helmholtz energy change. Quantitative SERS sensing is carried out on wet and dried AuNPs interfacial arrays, both of which showing a LOD down to nM scale.

Furthermore, microdroplets interfaces are used as the gold nanoparticle array templet for SERS sensing, which provide huge potentials for its applications in microfluidic SERS sensing. SERS sensing of analytes from multiple phases are also analysed in this chapter to further widen its application scenarios. This method provides a versatile protocol for direct SERS sensing of various of analytes.

In chapter 5, a number of fundamental problems related to droplet-based microfluidic SERS sensing are discussed. AuNPs aggregated by CB[n] are generated in microdroplets as SERS substrates, which could be used for chemical sensing in a high throughput way. The AuNPs aggregating process has been analysed systematically by dark field and bright field microscopy. SERS in microdroplets has been furtherly explored. Methyl viologen (MV), as a SERS marker, is tested in flowing microdroplets when the AuNPs are in high concentration. The position of aggregates in microdroplets has been explored based on the images, videos and spectra, which can furtherly help to get the strongest spectrum of analytes. Then the inverse relationship between signal of MV and oil is observed by SERS scanning online in flowing droplets, when the integration time is as short as 0.01 to 0.05s.

In the final concluding chapter of the thesis, it summarises the presented work and also gives a brief outlook of the potential future work.

<div align="right">Wenting Wang</div>

<div align="right">*Ultratrace Neurotransmitters SERS Sensing*</div>

Acknowledgements

I would like to express my gratitude to many people who have provided encouragement, support and help to me during my PhD study in the University of Cambridge.

Firstly, I would like to thank my supervisors, Prof. Chris Abell and Prof. Jeremy Baumberg for giving me the opportunity to study in the world's best university and conduct research in both excellent groups. They both offered great support for my research, guiding me to grow up as a mature researcher gradually. The working experience with them will be my life treasure, which will always encourage me to be a hardworking, strong-minded, supportive, kind-hearted and upright human being, no matter where I go and what kind of job I do in the rest of my life.

I also would like to acknowledge my co-workers as well as my colleagues in both groups, who helped me and let me work in such enjoyable environment. First big thanks go to Dr Anthony Coyne, Dr Ziyi Yu in Chris's group and Dr Bart de Nijs, Dr Wilson Chan in Jeremy's group, they all kindly offer great help to my PhD research from the beginning to the end, and offer valuable advices on manuscript writing skills to my PhD thesis. Without their help, my PhD thesis would not be possible. I also want to express my gratitude to Dr Oliver Pambos, Dr Zhijun Meng, Dr Andrew Salmon, Tina Leontidou, Dr Marlous Kamp, Dr Rohit Chikkaraddy, David-Benjamin Grys, Dr Jialong Peng, Dr Junyang Huang, Dr Ivana Lin, Dr Shu Hu, Dr Yidong Hou, Charlie Readman, Alex Huang and other colleagues who offered their kind support during my PhD study. I also want to thank Dr Katherine Abell, who has been excellent as the group administrator and offered strong back support for both my study and life during my stay in Cambridge.

In addition, I am indebted to the Winton Scholarship, which offered me financial support and the chance to dig out more in the field of SERS. I want to thank Dr Nalin Patal for his support while dealing with my funding.

Finally, and most crucially, I owe my deepest gratitude to my father Runguang Wang and my mother Yurong Wang, for their constant concern and inspiration. They always give me unconditional love and the strongest support for whatever I pursue. I also want to thank my fiancé Xin Zhang, who has given me endless love, patience and support during our long-distance relationship. I really love them all.

Contents

Chapter 1 Introduction

1.1 Droplet-based Microfluidics

Microfluidics, which first emerged in the 1950s[1,2] when the development of ink jet printers spurred research in the field of droplet production, offers the possibility for precise control on the manipulation of samples in micro-scale microfluidic channels, as the amount of sample microfluidic devices needed is usually femto-litre to micro-litre in volume. This methodology has been developed into platforms which can explore many functions at the same time, for example, to fluid mixing, [3–5] to liquid pumping,[6–8] and to provide an isolated droplet space for cell culturing.[9–11] It has received much attention from a broad range of fields such as materials,[12] pharmaceutics,[13] organic chemistry[14] and biological science.[15] Microfluidic technology holds great promise as it can perform typical laboratory operations using a fraction of the volume of reagents in significantly less time.

1.1.1 General introduction to droplet-based Microfluidics

As a subcategory of microfluidics is droplet-based microfluidics (also named multiphase microfluidics, plug-based microfluidics or segmented-flow microfluidics) which is a technology for manipulating and processing small (10^{-6} to 10^{-15} L) volume droplets or plugs carried in an immiscible phase.[16] Microdroplets in microfluidic channels can be generated,[17] merged with each other, [18] split, [19] trapped,[20] and sorted[21] with hydrodynamic, electrical, and optical-based droplet manipulation techniques.

Since the droplets in microfluidics platforms can be isolated, each droplet could play a role as a micro-reactor or micro test-tube to perform chemical reactions independently. Figure 1.1 shows the schematics of reactions occurred in a single phase microfluidic channel and a droplet-based microfluidics channel.[22] Droplet-based microfluidic systems share the same advantages as common microfluidic channels including: (1) the ability to process reactions in very small sample volumes (down to femto-litre scale), enabling the monitoring of single cells.[23] (2) various droplet manipulations (including generation, merging, splitting and sorting) enabling multi-step reactions happening inside droplets.[24] (3) ultra-high throughput generation and detection of large amount of droplet reactors (up to 100 kHz), facilitating large-scale screening of samples.[25] (4) dilution of analytes in microdroplets, providing a stable environment and high-fidelity information for long-time monitoring.[26] (5) minimization of adsorption of samples on channel surfaces.[27] and (6) enhanced mixing and heat/mass transfer inside droplets due to high surface area to volume ratios, which could accelerate the chemical reactions.[28]
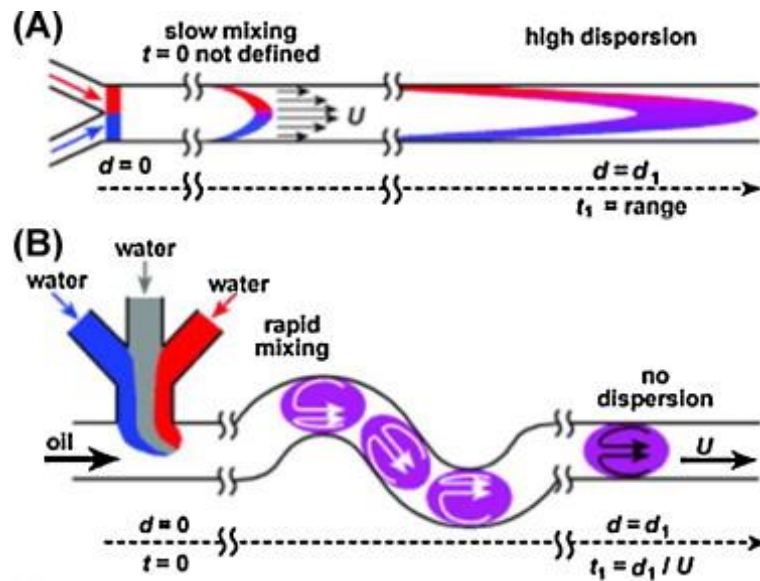
Figure 1.1 Schematic comparison of a typical A + B reaction a) in a conventional single-phase microfluidic system and b) in a droplet-based microfluidic system.[22]

There are two major types of microfluidic geometry designs to generate droplets: T junction[29,30] and flow-focusing.[31,32] In T junctions, the continuous phase and the dispersed droplet phase are injected to two arms of the "T" shape. The shearing force between the two phases and the liquid-liquid interfacial tensions are the main cause of the droplets generation (Figure 1.2 a and b).[33] As for the flow-focusing configuration, the continuous phase is injected through two outside channels and the dispersed phase is injected through a central channel into a narrow orifice (Figure 1.2c[16]). The follow-focusing geometry is widely used especially for ultra-small (a few microns in diameter) droplets or viscous droplets. For both geometries, surfactants are normally added to the continuous phase (or dispersed phase) to stabilize the liquid-liquid interfaces of the droplets.

The droplets size can be influenced by various factors. The orifice dimensions of the T-junction or flow-focusing junction could influence the droplets generation process and the droplets sizes. The properties of the fluids also could determine the droplets sizes, for example, the interfacial tension between two phases (influenced by the type and the amounts of surfactants added) and the viscosity of the two liquid flows phases. The other important influential factor is the operation conditions such as the velocity of two (influencing the shearing force of the droplets), and hydrophilicity of the channel surface. The droplets produced can be controlled by tuning a few factors. For instance, droplet size can be decreased by increasing the surfactant concentration within the system, or changing the ratio of the flows.[34]

2
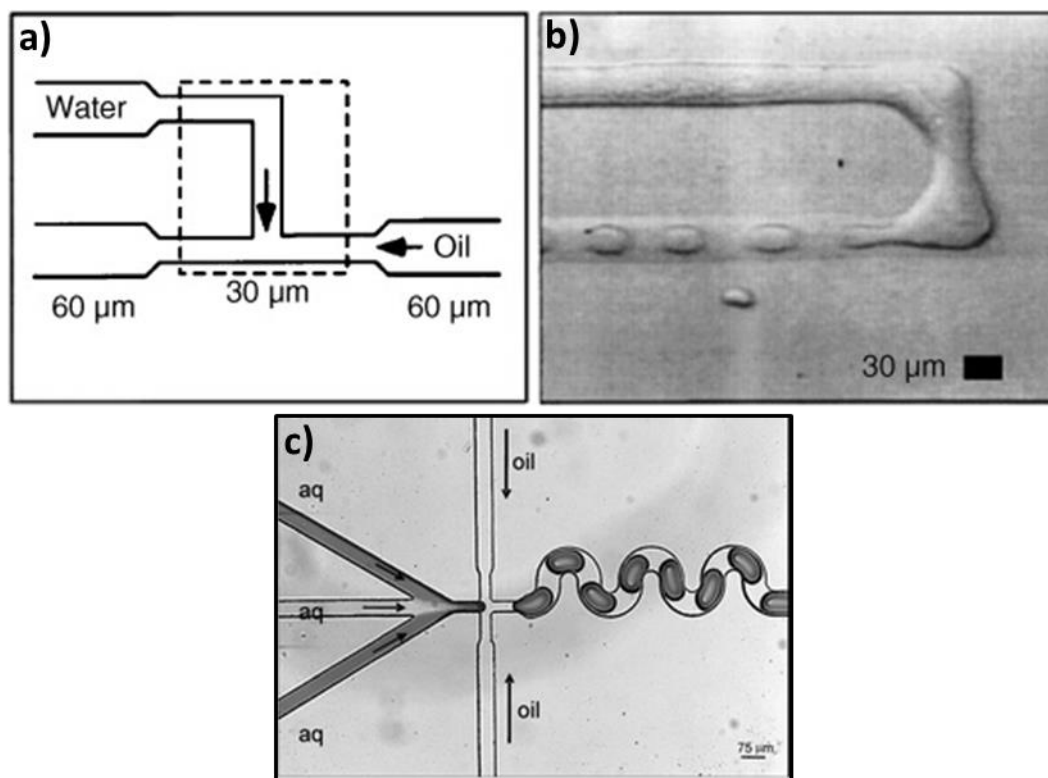
Figure 1.2 a and b) Formation of droplets within a T junction of a microfluidic device.[33] In this case, the oil is a mixture of hydrocarbon and the surfactant Span80. c) A flow focusing device with three aqueous inlets.[16]

1.1.2 Analytical detection in microfluidics droplets

In spite of the advantages and the advancements of droplet-based microfluidics technology, many challenges still remain in order to solve many real-world problems. One of the major challenges is in the detection of the analytes inside droplets both qualitatively and quantitatively with a simple and low-cost protocol. Currently, the analytical detection techniques used in droplet-based microfluidic systems are electrochemical detection, mass spectrometry (MS), nuclear magnetic resonance (NMR) spectroscopy and optical detection. Among which the electrochemical, MS and NMR methods all need complicated sample preparation steps before measuring. Fluorescence optical detection requires fluorescently labelled molecules, which limits its application. Raman could be a supplement to the above mentioned methods due to its simple measuring procedures and no requirement for labelled molecules.
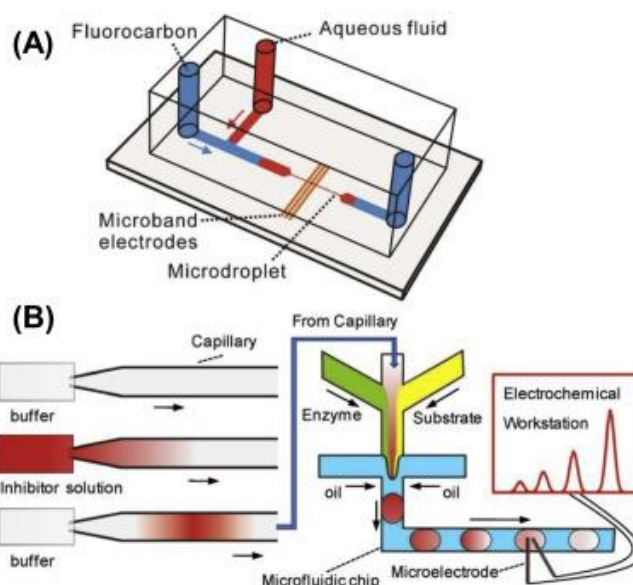
Figure 1.3. a) A microfluidic device with a narrow section used to stretch the droplets for electrochemical sensing.[35] b) A microfluidic device with two wire microelectrodes inserted into the centre of the channel for electrochemical sensing.[36]

Electrochemical detection is a conventional sensing technology which has high sensitivity, quick response, easy integration, and cheap in cost. In order to enable the electrodes to measure target molecules within the droplets, the first step is to eliminate the interference from the continuous phase which prevents direct contact of the dispersed phase with the electrodes embedded in the microfluidic channel walls. Making a part of the channel narrower than the rest can help produce longitudinally elongated droplets, which can lead to desirable intra-droplet mass transfer processing to the electrodes and lead to stable current measurements (See Figure 1.3a[35]). One such example used gold electrodes which were integrated on the narrowed channel section and electronic current was applied while the droplets flowing by the narrow channel. Other chip designs also worked well, for example, two wire microelectrodes were inserted into the centre of the microchannel through the wall of the chip, which was used successfully in the sensing of thiocholine (Figure 1.3b[36]).
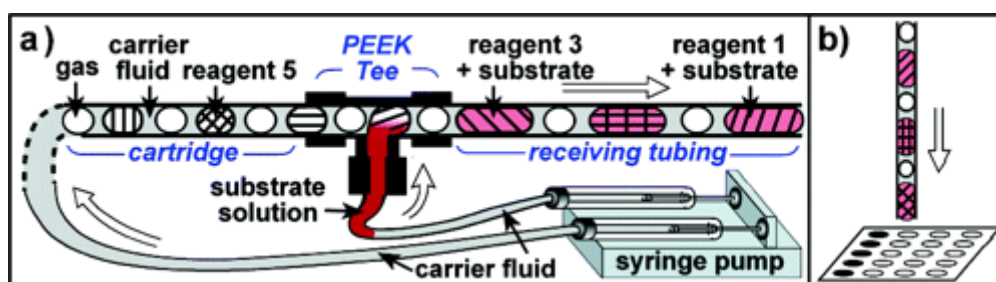
Figure 1.4 This system uses discrete droplets (plugs) as microreactors separated and transported by a continuous phase of a fluorinated carrier fluid. Workflow of the screening system. a) Serial merging of the substrate stream with reagent plugs from a cartridge. (b) After incubation, the reaction plugs are deposited onto a sample plate for MALDI-MS.[37]

Mass spectrometry (MS) detects the analytes by measuring the mass to charge ratio and it shows advantages such as label-free, high sensitivity and simultaneous measurements of multiple chemicals. The use of MS in droplet analysis could greatly broaden the application of droplet-based microfluidics. Hatakeyama[37] reported a combined technique of microfluidic droplets and matrix-assisted laser desorption ionization-mass spectrometry (MALDI-MS) for monitoring chemical reactions (Figure 1.4). However, the surfactants used in microfluidic systems to stabilise the droplets or to provide a biocompatible environment for cell culturing, could inhibit the ionization efficiency in MS electrospray process and contaminate the mass spectrometer. Therefore, apart from the microfluidic systems without surfactants, the application of droplets-MS technique could be strongly limited by the usage of surfactants.

The fluorescence-based detection is the most widely applied optical based technique. It has advantages such as that it is non-destructive and has high sensitivity to targeted analytes by measuring the labels or endogenous fluorescent molecules. It has been widely applied for single-cell analysis in droplets in a simple way to quantify analyte concentrations and distinguish the expression differences among different droplets using a standard fluorescence microscope (see Figure 1.5).[38] A high-speed camera is usually integrated with fluorescent imaging, enabling high throughput screening of flowing droplets. One drawback of fluorescence-based detection is the requirement of fluorescently labelled molecules, which limits its applications in circumstances where non-fluorescent molecules are used.
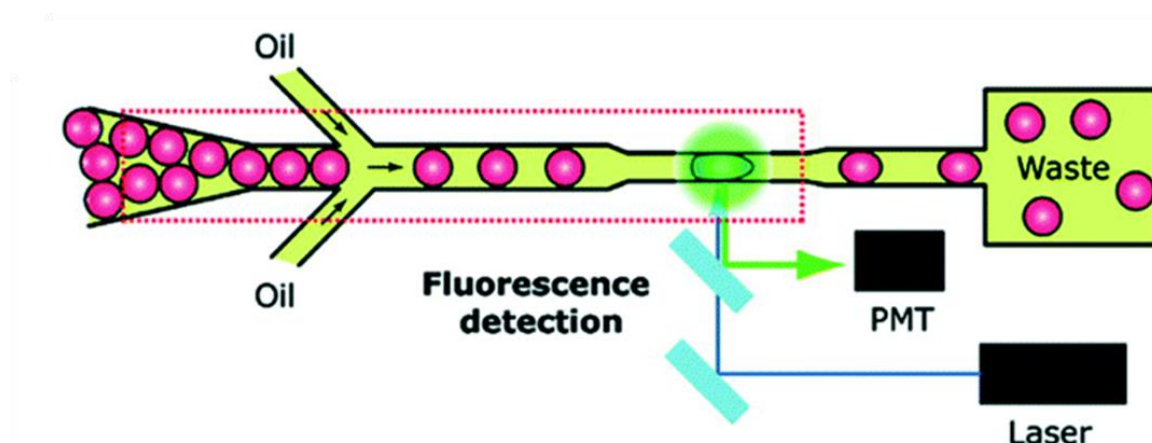
Figure 1.5 Droplets containing single cells were injected into the microfluidics device and separated with fluorinated oil. The fluorescence signal from the cells was monitored using photomultiplier tubes.[38]

Raman spectroscopy can be an alternative optical sensing technique with its label-free detection ability. It provides chemical structural information based on the inelastic scattering phenomena of molecular bonds when irradiated. Analytes can be recognized by the fingerprints of Raman shifts and can be quantified by corresponding peak intensity to concentrations. In addition, surface enhanced Raman spectroscopy (SERS) shows many other advantages such as simultaneous multiple analytes sensing, high throughput detection and high sensitivity. [39] The Raman spectroscopy and SERS will be reviewed in section 1.2. The integration of SERS detection with droplet-based microfluidic will be discussed in Chapter 5.

1.2 Surface enhanced Raman spectroscopy (SERS)

1.2.1 Mechanism of SERS

Raman scattering spectroscopy is a technique to obtain information on the chemical structure of molecules. Discovered in 1928 by the Indian Physicist C. V. Raman, Raman scattering can offer unique signal information for every particular chemical bond, which offers great promise in the detection and analysis field. In Raman scattering, a photon was scattered by exchanging energy with a molecular phonon or a molecular vibrational state (Figure 1.6). However, normally only one out of 10 million incident photons are inelastically scattered on the sample, so the Raman scattering is extremely weak. Therefore, even though Raman scattering can provide finger-printing information, it is not used as widely as Fourier-transform infrared (FT-IR) or UV/Vis spectroscopy. This weakness had long restricted the applications of Raman scattering, until the phenomenon of surface enhanced Raman scattering (SERS)[8] was discovered in 1974 by Fleischmann [3] which opened a new gate for Raman spectroscopy technology.
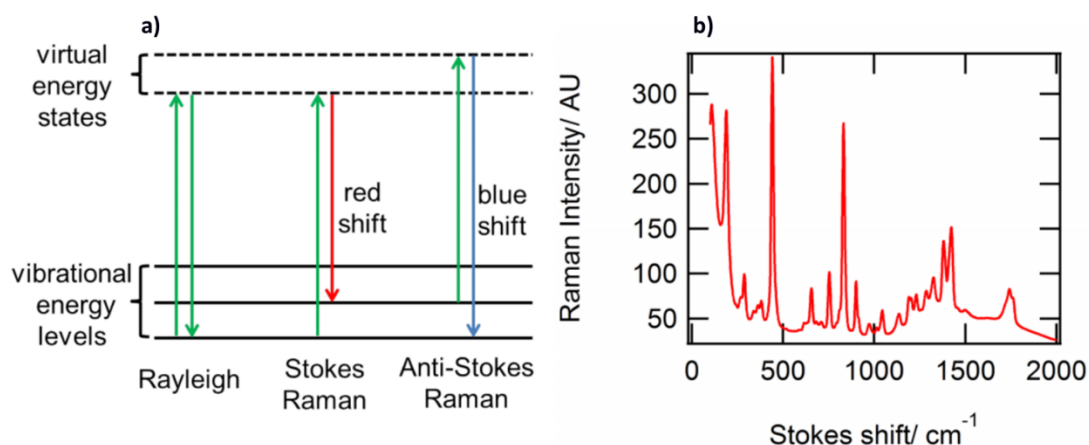
Figure 1.6 a) An energy change of molecular scattering. The photon is inelastically scattered in Stokes or anti-Stokes Raman with the molecules move to a higher or lower vibrational energy level.[41] b) A typical Stokes Raman spectrum of molecule cucurbit[7]uril. Each Stokes shift peak of the scattered light can be correlated to a unique vibrational energy level change, which can be correspond to a unique molecular structure.

In the SERS technique, Raman scattering is enhanced by surface interactions by using a noble-metal (Ag or Au) nanostructured surface with its intense electromagnetic field upon incident excitation. SERS was found to be an extremely sensitive technique (up to 10^{11} enhancement factor) that can be tailored to provide the detection of specific analytes through their unique vibrational fingerprints of molecules, even when the analytes are at ultra-trace concentration. The narrow linewidth of SERS spectra allows for multiple-analyte detection within complex mixtures, including detection down to the single molecule level. [41][42] Due to these advantages, SERS gradually gained attention of optical and material scientists. The interest in SERS was due to a number of factors, such as development of single molecule detection, nanotechnology, instrumentation capabilities and the application of this in diverse areas such as healthcare, safety, and explosive detection.

Though the mechanisms for SERS by metal nanostructure have long been debated, there are two main theories that stand out and are widely accepted, which are electromagnetic enhancement theory[43] and chemical enhancement theory.[44] The electromagnetic enhancement mechanism was proven by the surface plasmon resonance phenomenon.[43] On a metal surface, surface plasmons are vibrations of electrons on a conduction band. These electrons move easily when it is at the surface plasmon resonance frequency, leading to large vibration in the local electric field intensity. Many factors such as the surface morphology of the metal, the dielectric properties, and incident light frequency, can influence the surface plasmon frequency. Chemical enhancement mechanism involves the binding phenomenon of the analyte on the surface of the metal, which helps the charges transfer from the metal surface to the analytes, and this effect increases the analytes molecular polarizability.

Both of the above enhancement mechanisms play important roles in the SERS effects. However, it is widely believed that electromagnetic enhancement might have a greater influence than chemical enhancement. [45,4647]

On a nanostructured surface, the SERS can be described by the optical field enhancement.[48] In order to understand the enhancement mechanisms, the following equations can be inferred:

$$E_s = gE_0$$

where E_s is the surface electric field, g is the field enhancement factor caused by the nanostructure and E_0 is the incident field amplitude.

A molecule sitting near the nanostructure can scatter light by interacting with the local field. The Raman scattered field E_R therefore is related to the polarizability of the molecule (α_R) and the local surface electric field E_s, which can be described as:

$$E_R \propto \alpha_R E_s \propto \alpha_R g E_0$$

Then the Raman scattered field E_R is simultaneously enhanced by the nanostructure with the same enhancement factor g as for the incident field, so the surface enhanced Raman scattering field can be described as:

$$E_{SERS} = gE_R \propto \alpha_R g^2 E_0$$

As the Raman scattering light intensity I_{SERS} is proportional to the square of the Raman scattered field E_R:

$$I_{SERS} \propto E_{SERS}^2$$

$$I_{SERS} \propto \alpha_R^2 g^4 I_0$$

so the SERS intensity is proportional to g^4, which means that the field enhancement plays a significant role in the Raman scattering enhancement. A small field enhancement could cause a remarkable increase of the Raman signal. For instance, a 20 times field enhancement can lead to a 160000 times enhancement of Raman signal.

There are a number of factors to be noted from the above mechanism. Firstly, to obtain highly sensitive SERS signals, nanostructured surface should be designed to provide as high field enhancement factor g as possible. Secondly in order to get consistent intensity of SERS signals, the field enhancement factor g should be under control so that the SERS signals can be reproducible in different measurements, which require the controlled nanostructured metal surface. There are various nanostructures reported which can enhance the field including nanostars, nanotriangles and

nanorodes, etc.[4950] For spherical nanoparticles, the plasmonic coupling is required to enhance the Raman signals. Figure 1.7 shows a nanoparticle dimer and its strongly enhanced optical field in the gap of the two spherical particles.[46] The gaps that show highly enhanced optical field are called plasmonic hot-spots in SERS detection and the nanostructured novel metal material offering plasmonic hot-spots are called SERS substrates.
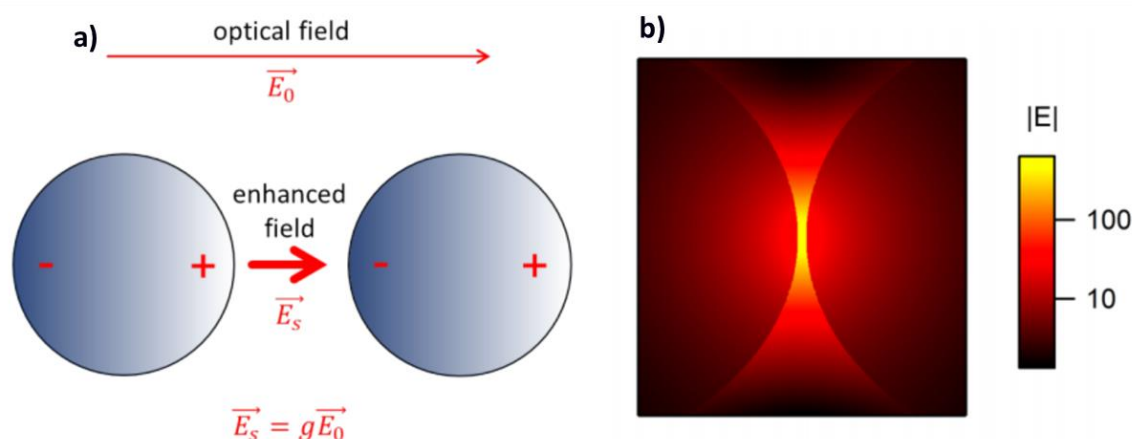
Figure 1.7 a) Schematic of optical field enhancement in the gap defined by an AuNP dimer b) Spatial distribution of the electric field across the gap for a simulated (BEMAX) AuNP dimer. [46]

Further, since the electric field intensity varies significantly at different places on the nanostructure (Figure 1.7), the SERS signal intensity is dependent on the placing of the analyte molecules on the nanostructure. Practically, not all the analytes are ideally located in the hot-spots, instead a statistical localisation of the analytes always happens on the nanostructured metal surface. If the hot-spots are saturated with analytes, the SERS signal detected will not be linear to the added analytes concentration and the upper LOD (limit of detection) is influenced by the amount of plasmonic hotspots offered by the SERS substrates.

In addition, the SERS signal and its reproducibility is also influenced by the polarizability of the molecule (α_R), which indicates that the way that analytes sitting at the hotspots are also very important. Therefore, the SERS signals are also influenced by how strong the molecules bind to the substrate surface and the way the molecules bind to the metal surface. In this aspect, it is helpful for the data consistency if chemically selective binding sites can be controlled at the metal surfaces.[51]

1.2.2 SERS substrates

Most SERS-active substrates are based on noble metals, typically Ag, Au or Cu. All three metals have localised surface-plasmon resonances covering most of the visible and near infrared wavelength range, where most Raman measurements are conducted. The most common SERS substrates can be

arbitrarily classified into 3 categories[52]: (1) metal nanoparticles in suspension; (2) metal nanoparticles immobilized on solid substrates; and (3) nanostructures fabricated directly on solid substrates by nanolithography and template based synthesis.

Metal nanoparticles in suspension are some of the most studied systems. These substrates can largely be organized into two broad categories: dispersed particles and aggregated systems. Many diverse synthesis schemes have been devised to create nanostructures of increasing complexity including nanorods[50], nanocubes[53], nanospheres[54,55], nanotriangles[56], nanowires[53], nanoplates[50] and nanostars[57]. The difference in the magnitude of the SERS response for these nanostructures is attributed to the number of 'hotspots' from per particle. Figure 1.8 shows SEM images of different structured nanoparticle SERS substrates.
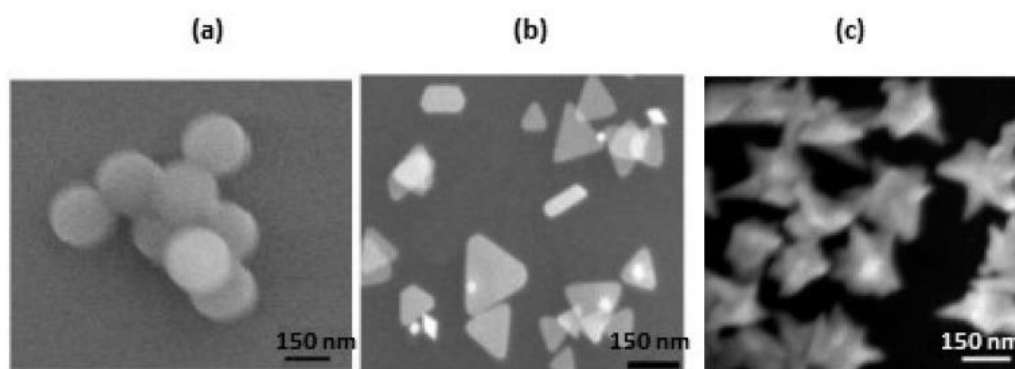
Figure 1.8 SEM images of the different gold nanostructures: (a) nanospheres; (b) nanotriangles, and (c) nanostars. [54]

For spherical nanoparticles, the aggregation process is needed in order to increase the Raman enhancement ability. [54] Aggregated particles are often prepared by adding small amounts of salt to metal nanoparticle solutions. Aggregated Ag nanoparticles were the first be used for single molecule SERS sensing.
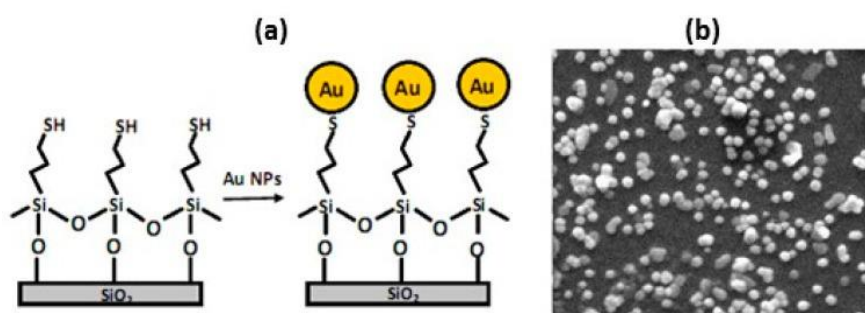
Figure 1.9 (a) Schematic representation of the procedure to immobilize Au NPs on a quartz substrate; (b) SEM image showing Au NPs immobilized on a quartz substrate.[58]

On solid substrates, metal nanoparticles can be immobilized orderly and compactly to provide plasmonic hotspots, by several strategies. One typical method is to use a 'chemical tether' to bond Au or Ag nanoparticle on the surface of quartz/silica,[58] as shown in Figure 1.9. Au or Ag nanoparticles are prepared by chemical reduction of $HAuCl_4$ or $AgNO_3$. The surface of the solid substrate is silanized using (3-mercaptopropyl)trimethoxysilane (MPTMS). After immersing the substrate in a suspension of Au or Ag nanoparticles, the nanoparticles can be immobilized on the surface. Similar substrates have been developed by immobilizing Au nanoparticles on other materials such as animated silica beads,[59] paper,[60,61] and alumina filters[62,63].

For nanostructures fabricated directly on solid substrates, nanolithography is one of the most commonly used methods for preparing surfaces with highly ordered metal nanostructures. For example, nanosphere lithography, which can fabricate well-defined 2D periodic arrays of nanoparticles for SERS[64,65](Figure 1.10). Three types of substrates can be fabricated using this nanosphere lithography techniques.[66] The first step of the nanosphere lithography is to drop cast a suspension of monodispersed polystyrene or SiO_2 nanospheres onto a conductive metal substrate, following which the nanospheres self-assemble into an ordered mask. Good conductivity of the substrates is normally required for further SEM characteristic of the fabricated metal nanostructure. Then physical vapour deposition or electrochemical deposition is used to generate a metal layer on the mask. The categories of substrates are (1) Au or Ag coated on nanosphere surface by physical vapour deposition; (2) Au or Ag triangular footprint after removing of nanospheres as well as the coatings by vapour deposition; and (3) hexagon shaped Au or Ag arrays after removing the nanospheres as well as the coatings by electrochemical deposition. The shape and size of the nanostructure can be tuned by the size of the nanospheres and the thickness of the deposited metal, which can help to match the requirement of sensing system, such as excitation wavelength to optimise the SERS measurement.
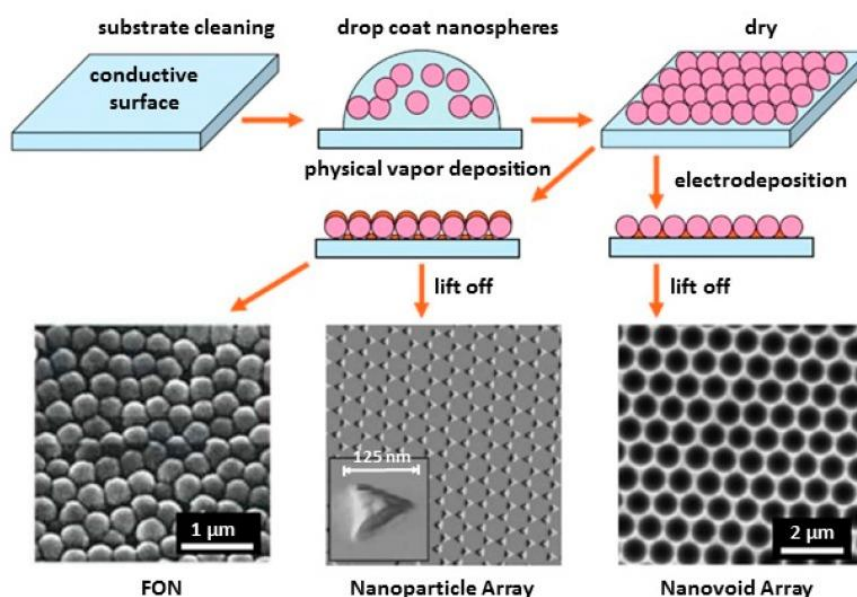
Figure 1.10 Schematic of the nanosphere lithography process for fabricating metal film over nanosphere.[66]

Electron-beam lithography is another commonly used technique to fabricate metallic nanostructures on solid substrates.[67–69] Figure 1.11 shows a schematic of two electron-beam lithography fabrication processes mostly used to fabricate nanostructured SERS substrates. [69] Firstly, on a silicon wafer coated with Au and resist (an electron-sensitive material), a focused electron beam is applied to draw designed shapes (e-beam writing). The solubility of the resist can be changed by being exposed to electron beams, enabling the removal of the exposed (or non-exposed) parts of the resist by flushing an organic solvent (developing). After development, the SERS substrate can be fabricated either by evaporating gold onto the template followed by lift-off, or plasma etching as shown in Figure 1.11. Compared to other techniques, the advantage of electron-beam lithography is to fabricate SERS substrates from custom patterns with sub-10 nm resolution.
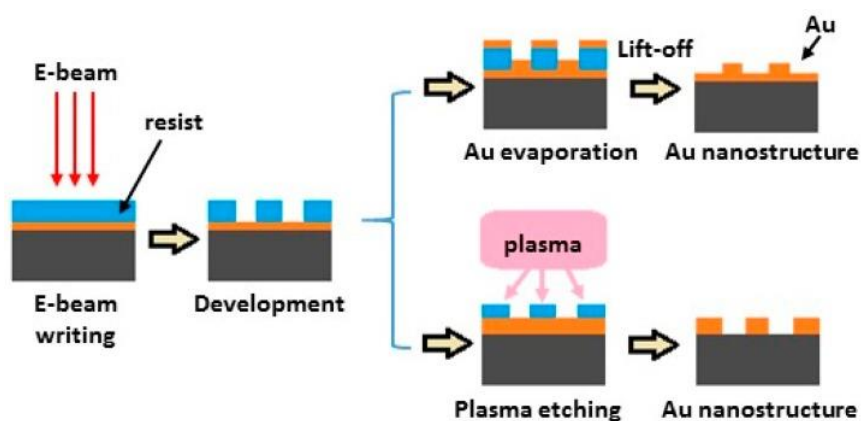
Figure 1.11 Schematic of the two fabrication processes used to prepare nanostructured SERS substrates.[69]

1.2.3 Analytes adsorbing on SERS substrates

To implement SERS detection of analytes, the molecules need to be adsorbed on the hotspots of SERS substrates. Conveniently, many of the SERS measurements reported so far were carried out with thiolated or aminated molecules, which can chemically bound to the surface of the substrates.[70–75] For analytes without strong binding groups, SERS signals are always not as strong, which limits its sensing applications.[70–75] [70] Various strategies have been developed to put analytes on the substrates plasmonic hot-spots, such as electrostatic and hydrophobic interactions,[70] mechanical trapping,[707677] and host-guest interactions.[78–8081]

When dealing with substrates of nanoparticles in solution, electrostatic or hydrophobic interactions are commonly used to decrease the repulsion force between the nanoparticles and the analyte molecules. Electrolytes including sulphates, nitrates or halides are added to the colloidal solution to increase the ionic strength and reduce the nanoparticle surface charge, leading to a smaller electrostatic repulsion between the metallic surface and the analytes.[70] At the same time, the nanoparticles could aggregate to form more hotspots although the aggregating process is usually not controllable.

For mechanical trapping technique, the Au or Ag substrate surface are always functionalised with an environmental responsive matrix which can trap and release analytes. Temperature and pH are the most used stimuli to the responsive matrix materials. [70,76] For example, poly-N-isopropylacrylamide (pNIPAM) is a commonly used temperature responsive material, due to its reversible phase transition at the temperature of 32 ℃. When the metal surface is coated with pNIPAM, small molecules can be trapped and released reversibly by tuning the environmental temperature, so that SERS signals of analytes can be obtained. [7076,77]

Host-guest interactions refer to the host molecule which normally has macromolecular cages interacting with its target guest molecules. It has been be utilized for binding analytes on SERS substrates. [7082–86]For example, the host molecule cyclodextrin, which shows extremely low SERS cross-sections, have been applied to the ultrasensitive detection of poly(allylamine hydrochloride),[83] explosives[82] and pollutants.[86] Other host systems such as calixarenes[84] and cucurbit[n]urils (CB[n]s, where n = 5, 6, 7 or 8)[78–80] are also emerging macromolecules which have been used in recent years for SERS sensing. CB[n], specially, does not only show low SERS cross-sections and selective encapsulation of a variety of guest molecules, but also can functions as a precise spacer between

nanoparticles in aggregatres.[80][85] Further introduction into the use of CB[n] will be discussed in chapter 2.

1.3 Summary

Droplet-based microfluidic technology has the ability to process small volume of droplets within micro-scale channels. One important application of droplet-based microfluidic is analytical detection, with various detecting techniques such as electrochemical, MS, NMR or optical detection. Among all the optical detection methods, fluorescence-based detection is the most widely applied technique, however its applications are limited by the requirement of fluorescent labelling molecules for non-fluorescent chemical analytes. Raman spectroscopy can be used an alternative optical sensing technique with its label-free detection ability, where analytes can be recognized by the fingerprints of Raman shifts and can be quantified by corresponding peak intensity to concentrations.

Raman scattering itself is a relatively weak signal when the analytes are in low concentrations, therefore surface enhanced Raman spectroscopy (SERS) is often utilised for Raman detection. In principle, in the technique, Raman scattering can be enhanced by surface interactions by using a noble-metal (Ag or Au) nanostructured surface with its intense electromagnetic field upon incident excitation. SERS is an extremely sensitive technique (up to 10^{11} enhancement factor) that can be tailored to provide the detection of specific analytes through their unique vibrational fingerprints of molecules, even the analytes are at ultra-trace concentration.

To implement SERS detection of analytes, the molecules need to be adsorbed on the hotspots of SERS substrates. Most SERS-active substrates are based on noble metals which can be classified in three categories: (1) metal nanoparticles in suspension; (2) metal nanoparticles immobilized on solid substrates; and (3) nanostructures fabricated directly on solid substrates by nanolithography and template-based synthesis. To bind target analytes on the surface of substrates, thiolated or aminated molecules were widely used since they can bind to the metal surface chemically. For analytes without strong binding groups, the binding can be achieved by various strategies, such as electrostatic and hydrophobic interactions, mechanical trapping, and host-guest interactions.

In this thesis work, metal nanoparticles in suspension will be firstly discussed, with the binding protocol of host-guest interactions and chelation interactions, specifically by Cucurbit[n]uril (CB[n]) and by Fe(III) ions. The fundamental resonance modes of neurotransmitters molecules and ultratrace neurotransmitters SERS sensing will be discussed in details. Further exploration of SERS substrates in the format of oil/water interfacial film will be reported afterwards, and the SERS application integrated with microfluidic technique will be covered in the final part of this thesis.

Chapter 2 Ultratrace Neurotransmitters SERS Sensing with AuNPs aggregates

2.1 Background

2.1.1 Introduction to NTs and the importance of NT SERS Sensing

Neurotransmitters (NTs) are the most important messengers of the nervous system. Due to the significant contribution of neurotransmitters to not only neurological functioning, but also endocrinological and immunological actions, clinicians and researchers are interested in the function and measurement of neurotransmitters as they have the potential to serve as clinically relevant biomarkers for specific disease states or to monitor treatment efficacy.

The initial identification of chemical messengers began by Ernest Starling and William Bayliss in 1902, when the existence of an internal communication system was reported with their discovery of the first hormone, secretin[87]. Subsequently, numerous other chemical messengers have been identified within the body such as epinephrine (EPI)[88] and norepinephrine (NEPI)[89]. The measurement of chemical messengers was rapidly adopted as a means to assess functions of organs or tissues and became the basis for diagnostic or functional indicators in clinical practice[90]. Despite a historical absence of relevant biomarkers in the realm of clinical psychiatry, this has expanded and neurotransmitters now serve as a primary target for the development of predictive or correlative biomarkers of nervous system function.

There are over 100 types of neurotransmitters reported and they are generally classified as amino acids, monoamines, neuropeptides, purines and gasotransmitters based on their chemical structure. In this chapter, a number of monoamine neurotransmitters which structurally contain one amino group connected to an aromatic ring by a two-carbon chain, namely dopamine, serotonin, norepinephrine and epinephrine are the focus for quantitative sensing. Dopamine is one of these neurotransmitters of significant clinical importance for motor functions and motivational behaviours. Its dysfunction is involved in many psychiatric disorders, including drug addiction[91], schizophrenia[92] and psychiatric conditions[93]. Serotonin is a neurotransmitter that regulates sleep and wake states, feeding behaviour, aggressive behaviour and mood/depression, among others[94]. Norepinephrine and epinephrine, also known as noradrenaline and adrenaline, respectively, are involved in the autonomic nervous system. In the hypothalamus, amygdala and locus coeruleus, the increase of norepinephrine release had been associated with anxiety and epinephrine plays a role in the fight-or-flight response by increasing the heart rate, vasodilatation, pupil dilation, and blood sugar[95].

Given their important roles in the central nervous system and the severity of disorders linked to their dysfunctions, the accurate detection and measurement of neurotransmitters are among the most important challenges in neuroscience. There are various approaches reported so far for neurotransmitter sensing and monitoring. Depending on the technology used in the literature, the most used sensing methods can be classified into the following categories[90]:

(1) Nuclear medicine tomographic imaging, including positron emission tomography (PET)[96] and single-photon emission computed tomography (SPECT)[97]. These methods offer high spatial resolution, but the equipment is expensive, making these techniques only suitable for diagnostic purposes where the functional studies and accurate localization of neurotransmitters in the brain are needed. In addition, since they are not suitable for neurotransmitter concentration detection, they must be used with techniques that have higher concentration sensitivity to get accurate neurotransmitter concentration measurements. Also, PET and SPECT both have limitations in terms of label improvement due to the overlapping signals from labelled tracer and target molecules.

(2) Electrochemical detection, including voltammetry[98] and amperometry[99]. These methods are reputed to be easy to implement in an implantable device, in addition to being cost effective. However, due to its low selectivity and the complexity of in-vivo chemical/molecular monitoring, its usage in real world applications still needs improvements in terms of reliability and selectivity. In addition, not all neurotransmitters can receive or yield electrons in a redox reaction on an electrode surface. Thus, only reactive neurotransmitters such as dopamine can be detected by using an electrochemical method without electrode functionalization. The electrochemical approach is also closely dependent on the electrode surface, which reacts with the targeted molecule. Thus, it is not possible to guarantee the stability and quality of the electrode for a long time; although it is possible to detect a good signal over a small number of detection cycles, the electrode degradation becomes significant as the number of cycles grows.

(3) Analytical chemistry techniques, for example high performance liquid chromatography (HPLC), which is a very sensitive technique that allows the detection of two enantiomers for example D-serine in the brain can be detected by HPLC.[100] Simultaneous detection of monoamine and amino acid neurotransmitters by HPLC and mass spectrometry was reported,[101] where five molecules including L-glutamate, GABA, dopamine serotonin and 5-hydroxyindole acetic acid were separated and then detected with an LOD of 0.40-1.26 nM. However, analytical chemistry techniques require expensive equipment, complex manipulations and are time consuming[90].

(4) Microdialysis. This method is a powerful technique to monitor analytes in vivo and is always used with invasive detection techniques. It is especially important for neurochemical sensing, such as

neurotransmitters monitoring in vivo while the animal is behaving, so that the neurotransmitters concentration change can be correlated to a certain behaviour. Other detecting techniques, such as mass spectrometry and liquid chromatography are always conjunct with microdialysis.[102,103] In practice, microdialysis has been used for the detection of amines, amino acids, neurotransmitters, neuropeptide and acetylcholine in the human brain.[104,105]

(5) Optical sensing, including fluorescence, chemiluminescence, optical fibre based biosensors and colorimetry.[102] Most optical sensing methods are suitable for miniaturization, thanks to rapidly advancing optoelectronic and MEMS (micro-electromechanical systems) micro-fabrication technologies, and the possibility to automate chemical reactions with microreactors, emerging as the most promising for neurotransmitter detection with high accuracy. However, the detection of neurotransmitters is still challenging due to their sparsity and their complex mixture with other molecules.

Approaches	LOD reported	Advantages	Disadvantages
PET and SPECT	Dopamine 200 nM[106]	High spatial resolution	Complex manipulation High cost
Voltammetry	Dopamine 50 nM[107]	High sensitivity	Low selectivity Electrode short lifetime
Amperometry	Dopamine 10 nM[108]	Low implementation cost	Low sensitivity and selectivity
HPLC	Dopamine, Serotonin 0.4 nM[101]	High sensitivity and selectivity	High cost and complex
Fluorescence	Dopamine 10 pM	High sensitivity and selectivity	May not be used in vivo
Optical Fiber Sensing	Glutamate 0.22 μM	High selectivity	Low sensitivity
Colorimetric	Dopamine 1.8 nM	High sensitivity and selectivity	May not be used *in vivo*
Field-effect Transistors	Dopamine, Serotonin 10 fM[109]	High selectivity and sensitivity	Complex device and manipulation required

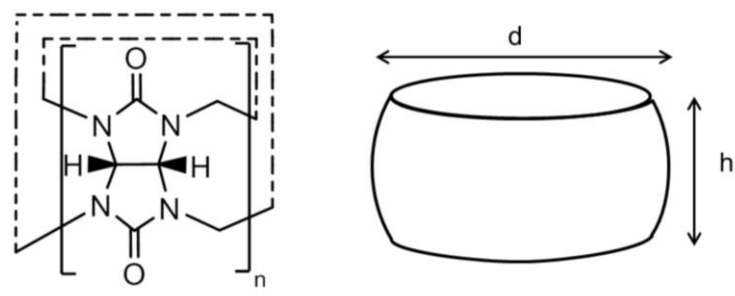Table 2.0 Technologies for neurotransmitters sensing[90]

The LOD, advantages and disadvantages of above sensing approaches for neurotransmitters and listed in table 2.0. These approaches are more or less limited by their sensitivity, selectivity complexity. Therefore, it is important to explore some new sensing approaches which have high selectivity, sensitivity and low manipulation complexity towards neurotransmitters.

In this thesis, surface-enhance Raman spectroscopy (SERS) is introduced as an optical sensing method to detect ultra-trace neurotransmitters. SERS uses photon interactions with matter to detect and identify molecules. Raman scattering is enhanced by molecules adsorbed on a metal surface, with an amplification factor that can reach 10 to 100 billion.[110] The surface is usually nanostructured gold or silver, and is functionalized to detect target molecules.[41,42] In this work, gold nanoparticles are the main SERS substrates. Usually, the SERS signals derived from individual nanoparticles are often too weak for detection. Therefore, nanoparticles need to assemble to form enough hot spots to enhance the electromagnetic fields and SERS signals. In order to achieve high sensing sensitivity and selectivity, neurotransmitters are selectively bound to the hot spots by different functionalizing molecules.

2.1.2 AuNPs-CB[n] aggregates used for SERS Sensing

In order to provide strong field confinement and enough 'hot-spots' for SERS sensing in solution, spherical AuNPs should be assembled by controlled methods.[111] Herein, a macrocyclic molecule cucurbit[n]uril (CB[n]) was used for this purpose. CB[n] are cage-like macrocyclic molecules consisting of glycoluril monomers linked by methylene bridges.[112] These macrocycles were named 'cucurbiturils' for their resemblance to a pumpkin, which belongs to the cucurbitaceae family [113] where n represents the number of glycoluril units. Table 2.1 shows the structure and dimensions of CB[n] molecules.[111] The height for all CB[n]s is 0.91 nm, since the height of a single glycoluril unit is fixed. The mean cavity diameter increases progressively from 1.31 nm for CB[5] to 1.75 nm for CB[8].

Historically, CB[6] was first synthesised in 1905 by Behrend,[114] by acid-catalysed condensation of glycoluril and formaldehyde, as shown in Figure 2.0a. However, the chemical nature and molecular structure were not identified until 1981, when a thorough investigation of CB[n]s was carried out by Mock and coworkers.[113] The research on the CB[n] family was largely promoted by the research groups of Kim, Day and Isaacs, who discovered and isolated four other homologues, (CB[5], CB[7], CB[8] and subsequently CB[10]).[115–118] Recently, the largest family member, CB[14], was reported with 14 glycoluril units linked by 28 methylene bridges.[119]

CB[n]	d/ nm	h/ nm
n = 5	1.31	0.91
n = 6	1.44	0.91
n = 7	1.60	0.91
n = 8	1.75	0.91

Table 2.1 Cucurbit[n]urils consist of n glycoluril molecules that are bound in a ring-like arrangement via methylene bridges. The external van der Waals dimensions of the CB[n].[111]
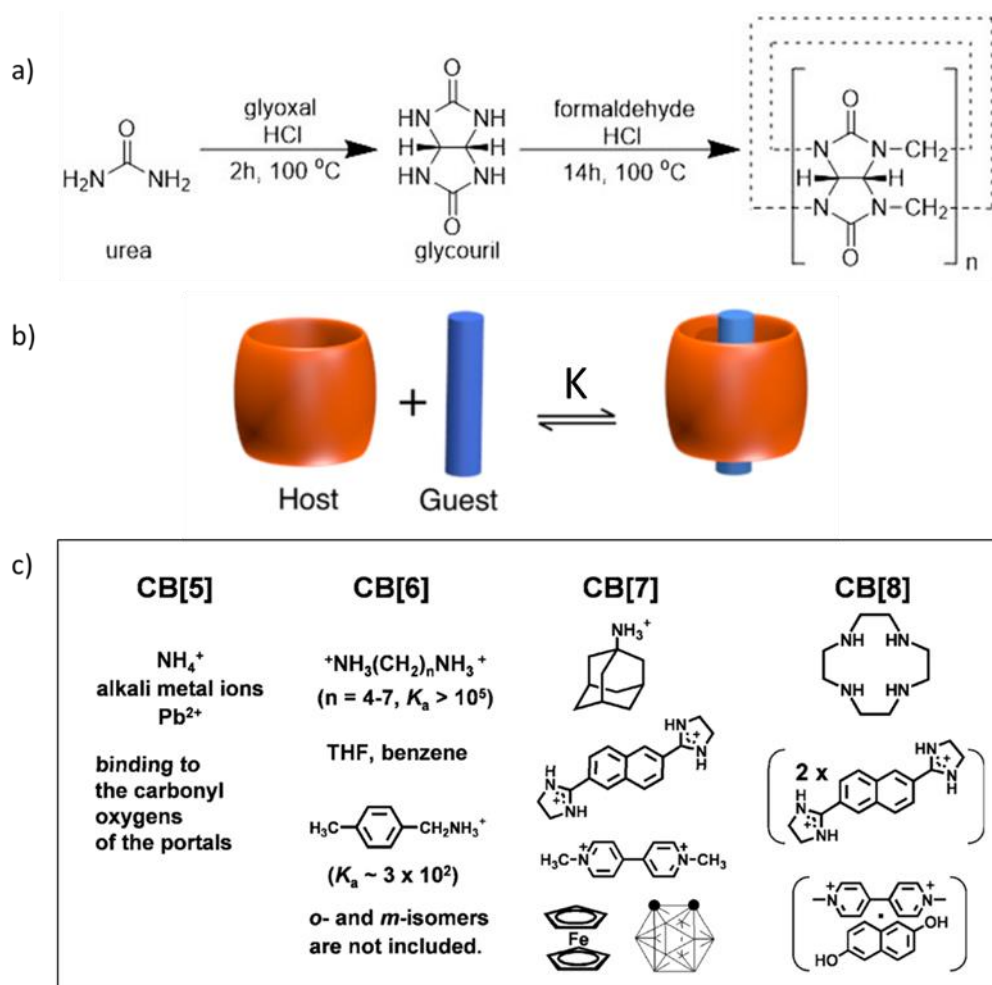
Figure 2.0 a) Synthetic scheme of CB[n]. b) Schematic diagram of host-guest complexation.[120] K is the binding affinity between host and guest molecules. c) Examples of the host-guest chemistry of CB[n].[112]

Like other macrocyclic molecules, including cyclodextrins and crown ethers, the CB[n] family is well known by their ability to bind analytes through host-guest chemistry.[121] Macrocyclic host-guest complexation is a process of molecular self-assembly where molecules bind selectively through supramolecular interactions. A host-guest complex is composed of at least one host and one guest molecule held together in a unique structure by non-covalent interactions.[111] Generally, the host component is a larger molecule, which is able to encompass a smaller guest molecule. A complementarity in molecular shape and binding sites location is the key to the host-guest complexation [111] and Figure 2.0b shows a schematic diagram of host-guest complexation.

CB[n]s exhibit remarkable guest binding properties attributed to their hydrophobic inner cavity and polar carbonyl portals.[122] The main driving forces of CB[n] complexation include the hydrophobic effect as well as ion-dipole and dipole-dipole interactions stemming from the electronegative carbonyl portals.[123,124] This host-guest complexation has also been studied from the energy point of view, which counts for the release of 'high energy' water molecules upon the inclusion of nonpolar organic guests.[125] More specifically, the guest molecule entering the CB[n] cavity leads to an energy loss from the reconstruction of hydrogen bonding network, which is due to the occupation of the guest and the release of trapped water molecules inside the cavity.[125] The differences in cavity and portal sizes of CB[n]s lead to different molecular recognition properties, as shown in Figure 2.0c.[112]

The smallest member in the CB[n] family, CB[5], only binds to protons, alkali metal ions and ammonium ions or encapsulates gas molecules (e.g. Ar, O_2, N_2, N_2O, CO_2, CH_4) and some solvent molecules (e.g. acetonitrile and methanol).[125] CB[6] is able to form stable complexes with protonated diaminoalkanes and protonated aromatic amines, e.g. p-methylbenzylamine, etc.[126] It is also able to encapsulate neutral molecules such as benzene and tetrahydrofuran in aqueous solution.[126] CB[7] can bind larger guest molecules that cannot fit into CB[6]. For example, CB[7] forms 1:1 complexes with protonated adamantane amine (ADA) and methyl viologen dication (N,N'-dimethyl-4,4'-bipyridinium, MV^{2+}), and can easily encapsulate neutral molecules such as carborane and ferrocene.[126] CB[8], with a much larger cavity volume, displays an unique ability to bind two guests at the same time.[122] It is able to encapsulate two 2,6-bis(4,5-dihydro-1H-imidazol-2-yl) naphthalene molecules to form a 1:2 complex, or two complementary guest molecules (a charge transfer complex) such as MV^{2+} and 2,6-dihydroxynaphthalene to form a 1:1:1 ternary complex.[126] It can be concluded that unlike most other host compounds, CB[n] can be selective of molecular size, shape, and functional groups in the guest

molecules that it binds to.[116] The different CB homologues are additionally selective for distinct molecules to each other which makes the CB[n] family an extremely versatile platform for supramolecular chemistry.

On the other hand, CB[n] macrocyclic molecules are also known for the ability to bind metal surfaces by using the C=O group. The direct interaction of CB[n]'s portal with the Au surface was firstly reported by An and co-workers (Figure 2.1 a, b and c).[127] CB[n]s acted as direct molecular junctions between adjacent Au NPs, resulting in the formation of coagulates. The CB[n] molecules were oriented perpendicular to the Au surface, and the NPs were separated by CB[n] molecules at a precise distance of 0.9 nm, as shown in Figure 2.1b and c. The strong and irreversible binding between CB[n] and the Au surface is attributed to the electrostatic interactions between their electronegative carbonyl portals and the metal surface, as well as the chelation.[127] They can define the gap distance between every two nanoparticles as 0.91 nm because the height of CB[n] molecules are 0.91 nm. This gap of 0.91 nm is a good size for enhancement of plasmonic coupling in nanostructure, neither big enough so the enhancement of electronic magnetic field is weak, nor small enough so the charge transfer dominates a lot, covering up the field enhancement.
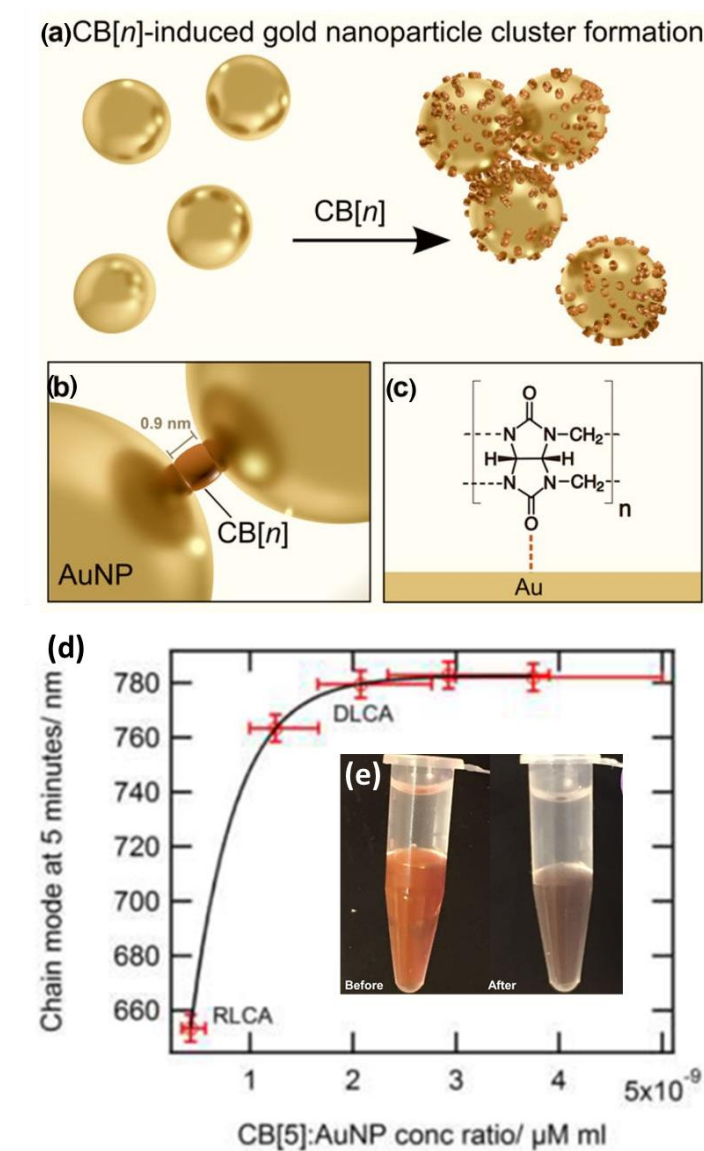
Figure 2.1 a) CB[n] acts as a 'glue' in between gold nanoparticles forming nanoparticle coagulates.[127] b) nanoparticles are held apart by CB[n] molecules at a precise distance of 0.9 nm.[127] c) CB[n]s bind to metallic surfaces through its carbonyl portals and are oriented perpendicular with respect to the gold surface.[127] d) Extinction chain mode maxima at five minutes for AuNPs undergoing CB[5]-induced assembly as a function of the CB concentration.[128] At low CB concentrations the assembly is reaction-limited (reaction-limited colloidal aggregation, RLCA). At higher concentrations the assembly is diffusion-limited. e) AuNPs suspension before and after adding CB[5] and solvent.

Overall, combining the abilities of capturing guest molecules and gluing Au nanoparticles to form nanostructured 'hot-spots', CB[n] can bind and place the guest molecule analytes specifically in the gaps between the nanoparticles. SERS sensing of these analytes can be performed with the gold nanoparticle aggregation triggered by CB[n]. The defined gap size of 0.91 nm can not only enhance

the plasmonic coupling, but also define the strength of the coupling, which provides a possibility for quantitative SERS analysis.

In order to obtain gold nanoparticle aggregates, a simple method is to add CB[n] aqueous solution directly into AuNPs suspension. Figure 2.1e shows the comparison of AuNPs suspension ($C = 2.6 \times 10^{10}/mL$ 60 nm diameter from BBI International, covered by n-hexane on the top) before and after adding one drop of CB[5] (1 mM). After the addition of CB[5], the colour of the AuNPs suspension changes to purple from red.

There are two steps for AuNPs aggregation, diffusion and reaction, either of which could be the aggregation forming rate limiting step. Based on the relative concentrations of AuNPs and CB[n] solution, the process can be distinguished into two phases, reaction limited colloidal aggregation (RLCA) and diffusion limited colloidal aggregation (DLCA) (Figure 2.1d).[129] When the CB[n] concentration is relatively high, there is enough CB[n] to cover the surfaces the AuNPs, therefore the assembly process is very fast and the diffusion of AuNPs limits the assembly process. In the case of DLCA, the aggregation tends to be large and uncompact, because the binding of AuNPs are irreversible and newly-joining AuNPs tend to stay around the periphery when they first get into touch with the cluster.

In the case of RLCA, the CB[n] concentration is always too low to cover the particle surface, so that the speed of the AuNPs-CB[n] reaction is very slow, dominating the AuNPs assembly process. The binding strength is not as strong as in DLCA regime, so that AuNPs always collide several times before they aggregate permanently. Therefore, the aggregates are more compact than DLCA and the assembly process is slower.[129] Figure 2.1d shows the extinction chain mode when the aggregation process takes place for 5 min for 60 nm AuNPs when adding different concentrations of CB[5]. When the CB[5] : AuNPs concentration ratio is high, the chain mode is mainly at longer wavelength mode 780 nm, which means that the assembly process is quick at DLCA. While at a lower CB[5] : AuNPs concentration ratio, the chain mode is at lower wavelength, which means the process is reaction-limited. For RLCA, it takes a longer time to reach long wavelength modes, not only because the assembly process is slower, but also the compact aggregates show shorter wavelength plasmonic mode than uncompact aggregates in DLCA.

2.1.3 NT binding methods to AuNPs hotspots

2.1.3.1 Binding by Cucurbit[n]uril Host-Guest Chemistry

In 1988, Lee group tested weak SERS signals of catecholamines at zero charge potential on a rough silver electrode.[130] They found that catecholamine was adsorbed on the surface of metallic silver

through phenolic hydroxyl groups. In 1995, Kneipp group used silver nano aggregates and gold nano aggregates to detect neurotransmitters.[131] The signal obtained on the gold nanoparticles was very weak and they believed that dopamine could not be adsorbed on the surface of silver or gold by chemical interaction. Therefore, the detection sensitivity of catecholamine directly from SERS substrates can be very low.

As stated above, the CB[n]s exhibit remarkable host-guest binding properties attributed to their hydrophobic inner cavity and polar carbonyl portals. In Figure 2.2, it shows the conceptual schematic of host-guest chemistry of neurotransmitters epinephrine (EPI), dopamine (DA) and serotonin (5HT) form 1:1 inclusion complexes with macrocyclic host CB[7].[120] The equilibrium constant K shown in the reaction is called binding affinity. The Scherman group has reported that dopamine molecules and CB[7] has a high binding affinity of log K = 5.00 to 5.66 in an aqueous environment.[120]
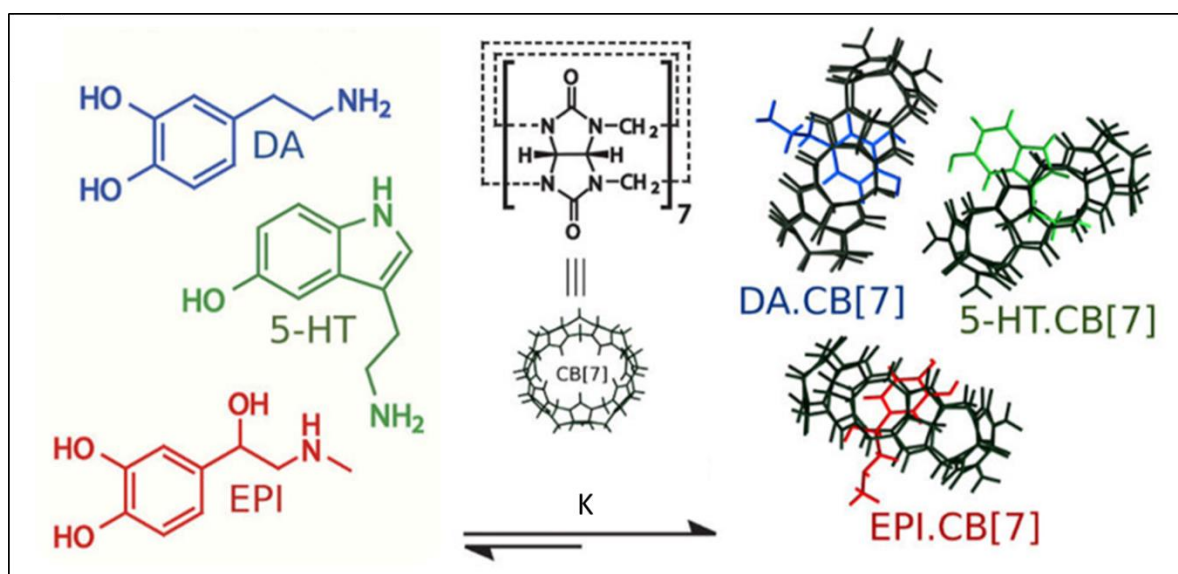
Figure 2.2 Conceptual schematic of host-guest chemistry of neurotransmitters epinephrine (EPI), dopamine (DA) and serotonin (5HT) form 1:1 inclusion complexes with macrocyclic host CB[7]. [120]

Through CB[7], a neurotransmitter can then bind and placed on the surface of Au, which provide hotspots for SERS detection. Figure 2.3 shows the schematic of the host-guest molecules near the gold surface in the hot-spot through their encapsulation inside the CB[7] cavity.[120]
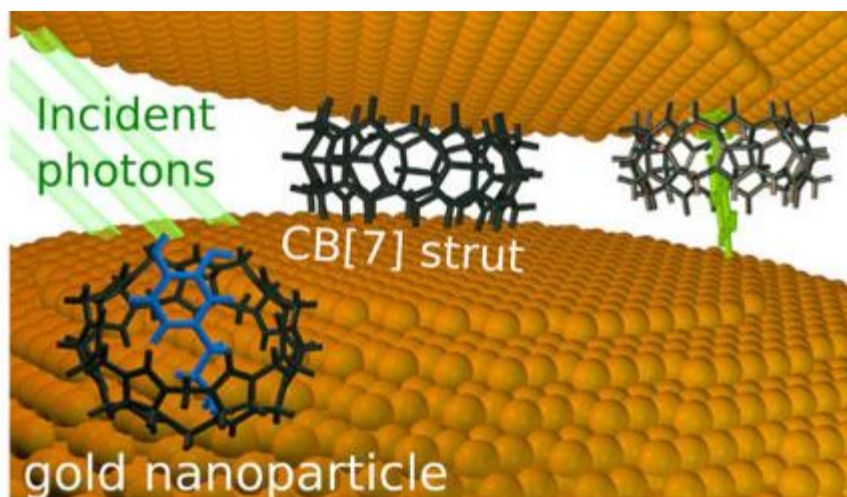
Figure 2.3 Schematic of the host-guest molecules (CB[7]-neurotransmitters) near the gold surface in the hot-spot.[120]

2.1.3.2 Binding by Neurotransmitters -Fe(III)-Citrate-Au complex

Iron ions can form bidentate complexes with catechol through Fe-O coordination bond.[132][133] Catecholamine neuro transmitters with catechol structure therefore can be adsorbed onto Fe ion-modified Au or Ag surface, therefore sitting on the SERS substrate hotspots to give enhanced Raman signals. Volkan's[134] group firstly modified silver nanoparticles with Fe ion complex Fe(NTA) (Fe Nitrilotriacetic acid) and used the complex as a 'binding agent' for dopamine. They then applied this Ag-Fe(NTA)-Dopamine complex for SERS sensing and achieved the LOD of several hundred Pico mole. Yang's[135] group also used a Fe(III) ion complex with citric acid to bind dopamine onto gold nanoparticle surface, so as to do low concentration dopamine detection by SERS.

For the binding behaviour of dopamine to Fe(III) specifically, by doing Fe(III)-dopamine titration, Franz[136] found that dopamine can bind to Fe(III) to form mono species, bis species and tris species by mole ratio of 1:1, 2:1, and 3:1 respectively. The titration curve showed three distinct steps that each correspond to the release of two protons upon Fe(III) binding. For triprotic dopamine H_3DA^+, as shown in Figure 2.4, these three steps point to formation of the mono species $Fe(HDA)^{2+}$ at pH values below 5.7, the bis species $Fe(HDA)_2^+$ at pH values between 5.7 and 7.2, and the tris species $Fe(HDA)_3$ above pH 7.3, with further deprotonation of $Fe(HDA)_3$ occurring above pH 10.
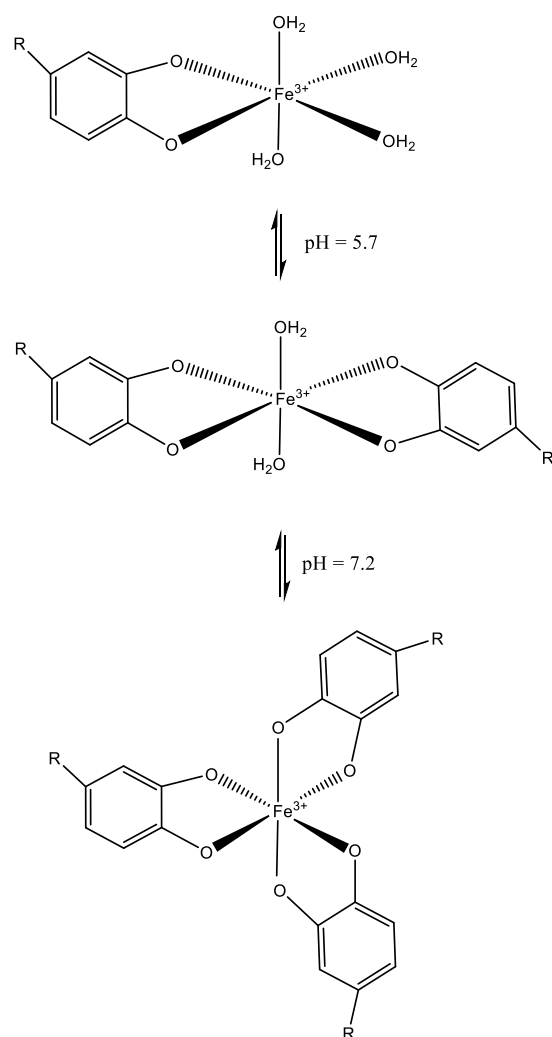
Figure 2.4 Mono, bis, and tris-catechol species formed by Fe(III) and DA in different pH environments.

The Au nanoparticles surface is normally stabilized by citric groups, which can also bind to Fe(III) ion. Hider[137] studied the Fe(III) affinity constants of citric systematically by spectrophotometric method. It was demonstrated that the predominant ferric citrate species at neutral pH values are the mono iron di-citrate complex ($[Fe(Cit)_2]^{3-}$) and di-nuclear, tri-nuclear oligomeric complexes, the relative concentration of which depends on the solution pH value and the iron: citric acid molar ratio. The $[Fe(Cit)_2]^{3-}$ complex predominates in the iron : citrate molar ratio range 1:100 to 1:10. The presence of oligomeric species becomes appreciable when iron: citrate ratios are higher than 1:10.

With the understanding of binding abilities to Fe(III) of citric acid and neurotransmitters, it is highly promising to bind neurotransmitters to citric modified Au surface with Fe(III), by forming a complex of neurotransmitters-Fe(III)-Citrate-Au. This structure can be the basic unit for neurotransmitters SERS sensing on Au surface, especially for low concentration samples. In the final section of this chapter, we will discuss the SERS sensing research based on this structure.

2.1.4 Overview of this chapter

In this chapter, a simple and efficient 'mix-and-measure' method will be used to form a liquid sensing platform by Raman/SERS. The basic research of dopamine Raman/SERS sensing in water solution is covered. Firstly, dopamine Raman spectra at different pH environments is discussed. Density functional theory (DFT) calculations are carried out to help understand the dopamine molecules' chemical bonds resonance modes. Dopamine concentration series for Raman spectroscopy are carried out to determine the detection of limit of dopamine in pure water which is measured to be in the range of 100 mM to 250 mM.

Furtherly, in order to decrease the limit of detection (LOD) of dopamine, the Raman signal is enhanced by SERS. Gold nanoparticles were used as the SERS substrates for dopamine detection. The AuNPs assembly process, dopamine-AuNPs binding methods by either CB[n] molecules or weak binding directly by dopamine molecule to Au surface is discussed. Dopamine LOD is 1 µM for NaCl-induced AuNPs aggregates SERS, and is 0.1 to 1 µM for CB[n]-induced AuNPs aggregations SERS, which reaches the level of physiological dopamine concentration in urine.

Iron (III) is then introduced as a binding molecule for dopamine and AuNPs. Two distinct protocols ('PreNP' and 'PostNP') are compared, which differ in the steps for forming SERS sensing complexes, affecting both the LOD and the DA SERS intensities. Characterising complexation of Fe(III) and dopamine (DA) in different pH suggests that Fe(III)DA2 dominates in PostNP detection, whilst in PreNP it is the monomeric Fe(III)DA that is seen. The dopamine LOD is 1 to 10 nM by dopamine-Fe(III)-AuNPs complex SERS, which enables to perform fast detection of multiplexed neurotransmitters (NTs) at physiological concentrations.

2.2 Raman spectroscopy of dopamine

Dopamine is one of the important catecholamine neurotransmitters, however its concentration in body fluids is only 0.01-1 µM[135], and there are many kinds of interfering substances such as amino acids, nucleic acids, glucose. Therefore, it is difficult to distinguish dopamine from other molecules in body fluids by conventional detection methods. Spectroscopic techniques, for example Raman, can identify corresponding molecules based on the characteristic peaks of substances, so is a useful method to detect dopamine or other neurotransmitters. Dopamine, epinephrine, norepinephrine and DOPA are all hydroxyphenyllethyl amine derivatives and their structures are similar (see Figure 2.5a), so their Raman vibration peaks will be similar. However, due to the existence of different functional groups, the Raman peaks of these molecules are different and the relative intensity is also different, as shown in Figure 2.5c, which can help to distinguish these substances from others.

Before examining the SERS sensing, it is essential to understand the nature of the spectra of dopamine obtained by Raman spectroscopy. In this section the Raman spectra of dopamine was measured and discussed at different pH. Density functional theory (DFT) simulation results were also carried out to understand the dopamine molecules chemical bonds resonance modes. The DFT simulation results includes effects of molecular configurations, so the absolute Raman activity of the molecules in theory can be compared for each complex format, and the Raman activity in 'real world' measurements can be drawn out by comparing the experimental results and DFT simulation results.
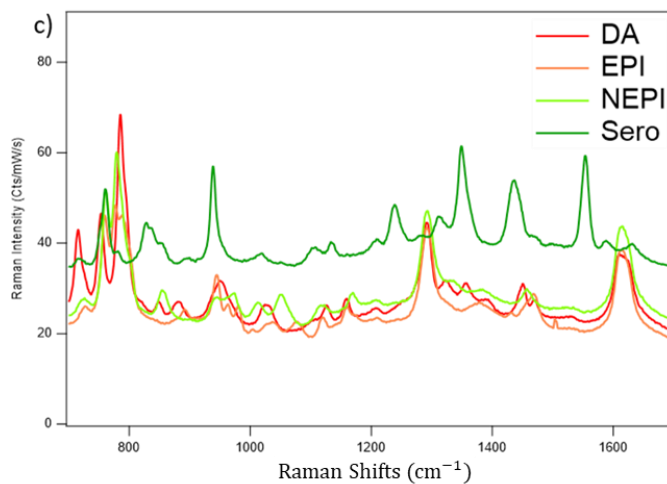
a)

Dopamine (DA)

Epinephrine (EPI)

Norepinephrine (NEPI)

DOPA

Serotonin (Sero)

b)

$(pKa_1 = 9.44)$ $(pKa_2 = 10.75)$

$(pKa_3 = 12.80)$

c)
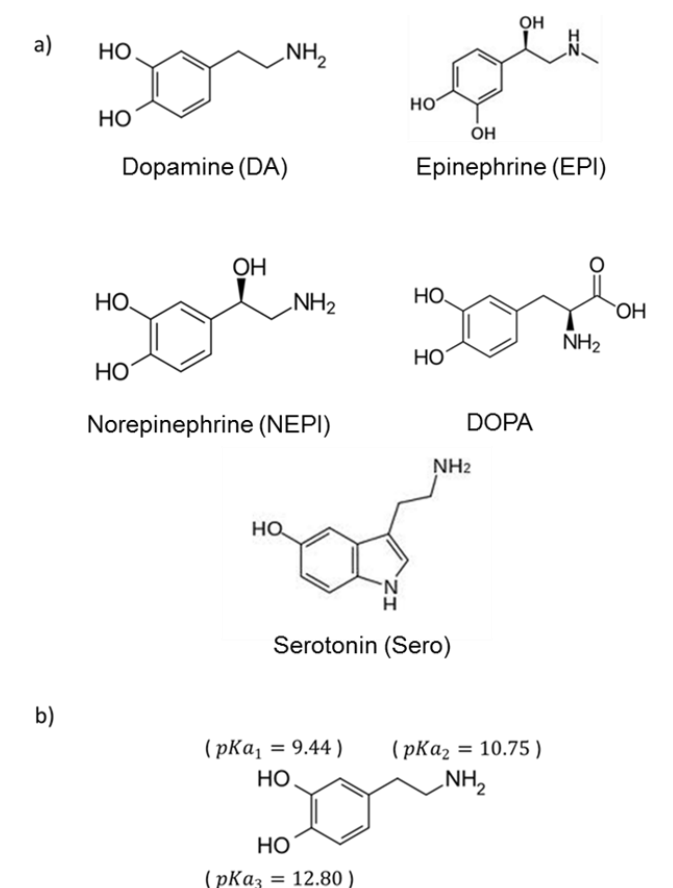
Figure 2.5 a) Molecular structures of dopamine, epinephrine, norepinephrine and DOPA. b) Dopamine pKa at different proton positions in water.[138] c) Raman spectra of dopamine, epinephrine, norepinephrine and DOPA, 1 M in deionized water.

 water.

As shown in Figure 2.5b, dopamine contains two phenolic hydroxyl groups which can donate protons, and one amino group on alkyl chain which can be protonated in solution. The three pKa for these 3 positions in water environment were measured as reported in the literature, 9.44, 10.75 and 12.80 respectively.[138] When the pH is 7.0, dopamine is protonated on amino group with one positive charge, DAH^+. Since the pH of biological environment is less than 9.44, dopamine exists as DAH^+ in the human body. The two phenolic hydroxyl groups and amino group can also form inter molecular hydrogen bonding in solution, to form dimer or multiple complexes, which may give out different Raman resonance from single DAH^+ molecule.

Raman spectroscopy, as well as SERS measurements were carried out using a Renishaw in Via Raman microscope equipped with a Plan 5X objective. The laser beam entered the sample from the (open) top of the cuvette or plate well containing samples. By performing a depth series, the optimum distance of the solution from the laser, which is the location yielding the maximum number of counts, was determined. At the ideal distance the focal point of the laser is near the liquid–air interface. This results in neither the illumination path nor the collection path passing through or near the plastic of the cuvette or plate well. Spectra were recorded in the range of 620–1730 cm^{-1} with a resolution of 1.1 cm^{-1}.

DFT calculations were carried out with Dr Ivana Lin's help (a postdoctoral researcher in Prof. Jeremy Baumberg's group in the Cavendish Laboratory, University of Cambridge), to show the specific Raman peak assignments for single unit DAH^+, dimer complex $2(DAH)^{2+}$ and tetramer complex $4(DAH)^{4+}$. For all calculations the Gaussian 09 *ab initio* software suite was employed.
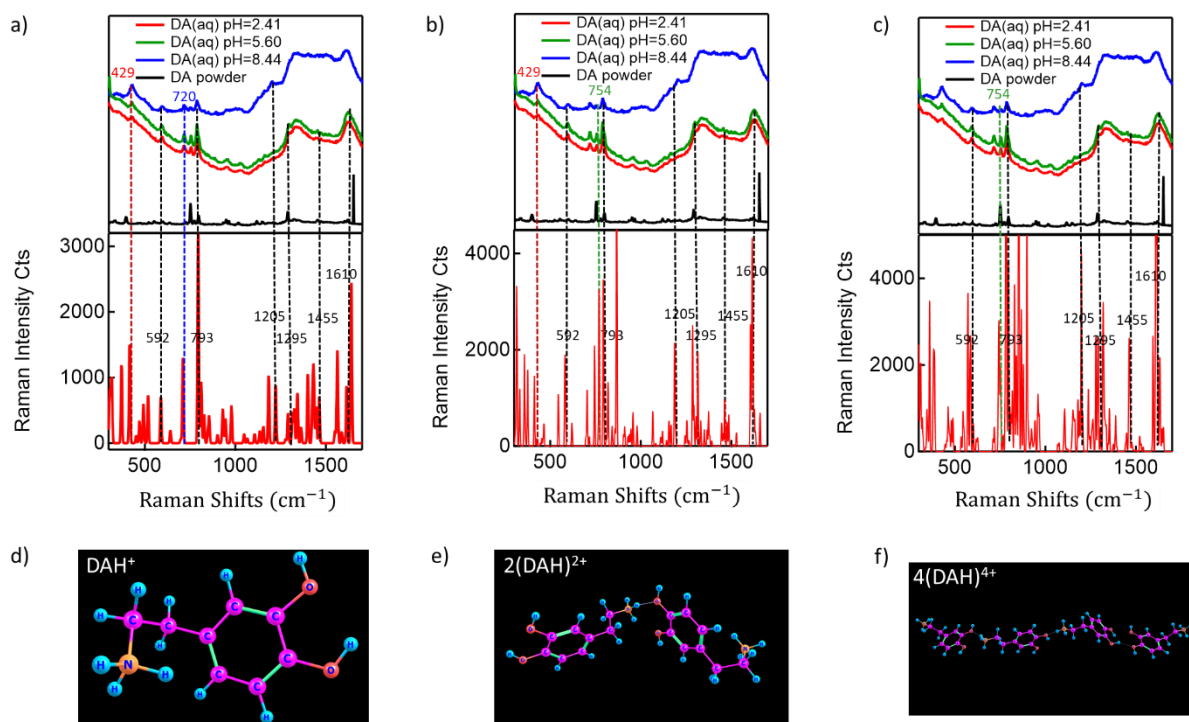
Figure 2.6 a-c) Top, Raman spectra of dopamine solution of pH at 2.41, 5.60, 8.44 and dopamine solid powder on silica wafer. a-c) Bottom, Raman spectra of dopamine in the format of single unit DAH^+, dimer complex $2(DAH)^{2+}$ and tetramer complex $4(DAH)^{4+}$ respectively. Dashed lines are Raman peak alignment of experimental data with DFT calculation results. d-f) Molecular schematics for DAH^+, $2(DAH)^{2+}$ and $4(DAH)^{4+}$, respectively. DFT calculations were carried out with wet samples (water molecules were involved in the calculation).

To understand the experimental Raman signals of dopamine molecule at different pH, experimental Raman data and DFT calculations for different dopamine formats in water solution were compared. In Figure 2.6 a-c, it shows the Raman spectra of dopamine solution of pH at 2.41, 5.60, 8.44 and dopamine solid powder on silica wafer. Dopamine was purchased in the form of dopamine hydrochloride (DAHCl), and was dissolved in water at 100 mM which shows pH of 5.60 originally. The pH of 5.60 can last for 1 hour until the solvent get gradually darker by DA being oxidised to quinone and poly-dopamine in air. The two solutions at pH 2.41 and 8.44 were obtained by adding different amounts of HCl or NaOH solution. The full 785 nm laser power of 131.6 mW was applied to solvent Raman measurement. Since all three pH are below the value of pKa_1 9.44, DAH^+ ions dominate in these three systems. The powdered dopamine hydrochloride was placed on silica wafer and low laser power of 0.13 mW was applied to avoid being burned. Compared to powder DA, Raman of solvents show raised backgrounds due to solvation effect. The spectra of pH 8.44 shows even higher background because dopamine is not stable in a basic environment and can be easily oxidised to a quinone[138]. When pH is above 8.0, the dopamine solution gradually turns dark from transparent because of the

oxidation of dopamine to quinone (followed by the formation of poly-dopamine)[139] and shows photoluminescence effect, so that Raman background raise significantly and Raman peaks become relatively weaker. However, the main peak positions of these 3 spectra stay consistent due to the same mode of DAH$^+$.

Table 2.2 shows the Raman peak positions of experimental data and their bound assignments based on the DFT calculation results in bottoms graphs of Figure 2.6 a-c. The peak at 429 cm^{-1}, which is attributed to the aliphatic chain C-C vibrations, is shown in DFT mode DAH$^+$ and 2(DAH)$^{2+}$, but not shown in mode 4(DAH)$^{4+}$, as marked as red dashed lines in Figure 2.6 a-c top graph. The reason is that the longer the network is, the less dense the electron cloud is on aliphatic C-C bound is, so that C-C electronic resonance become weaker than short networks. Peak 720 cm^{-1}, which is attributed to the H-C(β)-H twisting on aliphatic chain, only shows in DFT mode DAH$^+$, but not 2(DAH)$^{2+}$ and 4(DAH)$^{4+}$, as marked as blue dashed lines in Figure 2.6 a-c top graph. This is because the aliphatic chain H-C(β)-H electron twisting flexibility is weakened when the amino group forms hydrogen bond, showing less resonance in dimer and multiple modes. Peak 754 cm^{-1}, which is attributed to N-H-O hydrogen bond bending, however only shows in 2(DAH)$^{2+}$ and 4(DAH)$^{4+}$ modes rather than DAH$^+$, as marked as green dashed lines in Figure 2.6 a-c top graph. This is because no inter molecular hydrogen bond is calculated in DAH$^+$. The rest Raman peaks in Table 2.2 are shown in all of 3 modes, though the Raman intensity varies a bit due to the not exactly same electronic resonance environments.

Raman Shifts (cm^{-1})	Assignments
429	Aliphatic chain C-C vibrations
592	CH in-plane ring deformation, OH scissoring
720	H-C(β)-H twisting
754	N-H-O hydrogen bond bending
793	CH out-of-plane ring deformation
1205	C-O-H bending
1295	Ring breathing; CH aromatic rocking; CH twisting
1455	CH scissoring
1610	CH in-plane ring deformation, OH scissoring

Table 2.2 Raman peak positions of experimental data and the chemical bond assignments based on DFT calculation results in bottoms graphs of Figure 2.6 a-c.
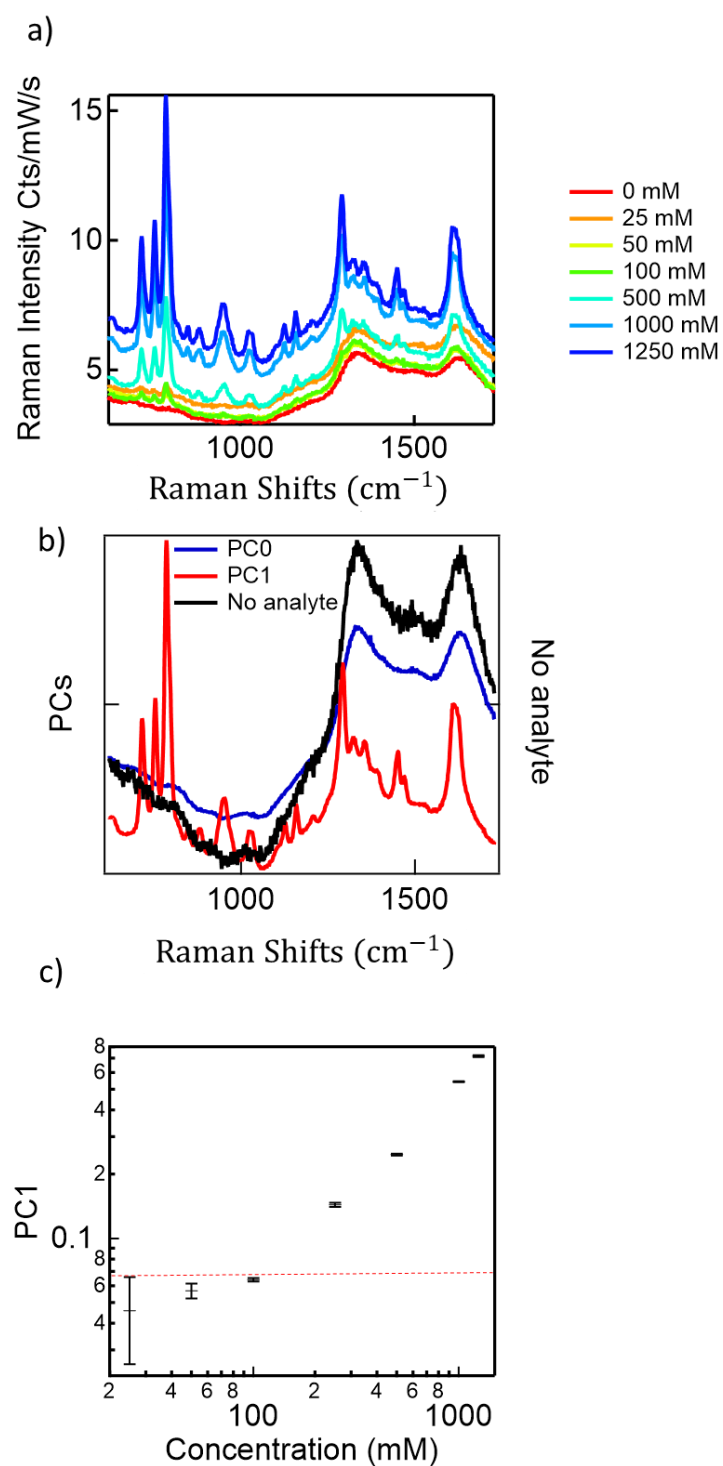

Figure 2.7 a) DAHCl concentration series in pure water. b) Raman spectra of sample without analyte, PC0 and PC1 after PCA analysis. c) PC1 scores vs dopamine concentrations in log-log axis with noise level dashed.

The Raman spectra were carried out with a range of different concentrations of dopamine to determine the LOD of dopamine in pure water, as shown in Figure 2.7a. The finger print region of the Raman spectra is only shown in samples with concentration above 250 mM, which indicates that the dopamine LOD is above 250 mM in pure water solution.

In order to further process, the raw spectra, instead of performing background fitting and subtraction to each spectrum due to the poor consistency and high complexity, a principal component analysis (PCA, See Section 7.1 for more details of PCA) was applied. These principal components represent linearly-transformed Eigen spectra that have different levels of correlation to the original SERS spectra, with corresponding scores (weights of Eigen spectra). A complete set of Eigen spectra and scores reconstructs the original SERS spectra. By using a transformation procedure[81], extracted scores can be defined, which are zero for samples without DA (PC0), and give values characteristic of the SERS strengths (PC1, PC2…).

Figure 2.7b shows PCA analysis result PC0 and PC1, where PC0 is correlated to the Raman spectra of sample without DA and PC1 is correlated to the major variation, dopamine spectra. Therefore, the change of dopamine concentration can be directly reflected on the PC1 scores, as shown in Figure 2.7c.

At low concentrations, the limit of detection (LOD) can be determined by the PC1 vs DA concentration plot (Figure 2.7c). The LOD refers to the lowest possible concentration at which the approach can detect the analyte quantitatively. In this experiment, typically, LOD is the lowest concentration that can be separated from lower detected concentrations. For example, in Figure 2.7c, by plotting PC1 (with standard deviation error bars) vs concentrations, we can find that the lowest detected concentration in the experiment that can be distinguished from lower concentrations is 250 mM. The signal of 100 mM concentration overlaps with the deviation error range of concentration 25 mM, so 100 mM is not quantitatively distinguishable. Therefore, the LOD in this experiment is 250 mM. The upper range of the PC1 deviation error bars (red dashed line) of lower concentration is used as a 'noise level' to distinguish the LOD in the experiment. By using this method, we can see that LOD determined is highly dependent on the concentration series resolution. Therefore, the LOD here only applies to the specific experimental condition. This data analysis method is applied throughout the thesis for concentration series experiments to determine the corresponding LODs.

Dopamine concentration in body fluids is normally between 0.01 to 1 µM, which is 5 to 7 order of magnitude below this Raman spectra LOD 250 µM. In order to decrease LOD of dopamine, the Raman signal needs to be enhanced by 5 to 7 order of magnitude, which could be achieved by surface enhance Raman spectroscopy (SERS). In the following chapter, gold nanoparticles (AuNPs) will be examined as

the main SERS substrates for dopamine detection. The AuNPs assembly process, dopamine-AuNPs binding methods by either CB[n] molecules or Fe(III) ions and weak binding directly by dopamine molecule its self will be discussed.

2.3 AuNPs-CB[7] aggregates formation in solution

Before the SERS measurement were carried out the AuNPs firstly need to be aggregated in the nanoscale to provide hotspots for the analytes to sit in. Time-resolved extinction spectroscopy can effectively track the AuNPs aggregate formation process. In Figure 2.8, it shows typical time-resolved extinction spectra during CB[7]-induced AuNPs aggregation (see Section 7.1 for further experimental details).

In Figure 2.8, all of the spectra show a 'monomer' mode at around 530 nm corresponding to the single nanoparticles or transverse mode of aggregates chains. As the AuNPs attach together, the plasmons hybridise giving lower energy coupled modes. A distinct 'dimer' mode at around 670 nm is observed when the nanoparticles are monodispersed, and the dimer mode corresponds to optically accessible dimers within larger aggregates and not necessarily to isolated dimers. The spectral position of the dimer mode is strongly sensitive to the coupling strength between the two nanoparticles. Smaller inter-particle gap sizes lead to longer adsorption wavelength for the dimer mode. The 'aggregate' mode above 670 nm red-shifts as the assembly progresses and the effective optical chain length increases. These three extinction spectra feature shows that the plasmonic modes of complex aggregates are simply governed by those three chain subunits.
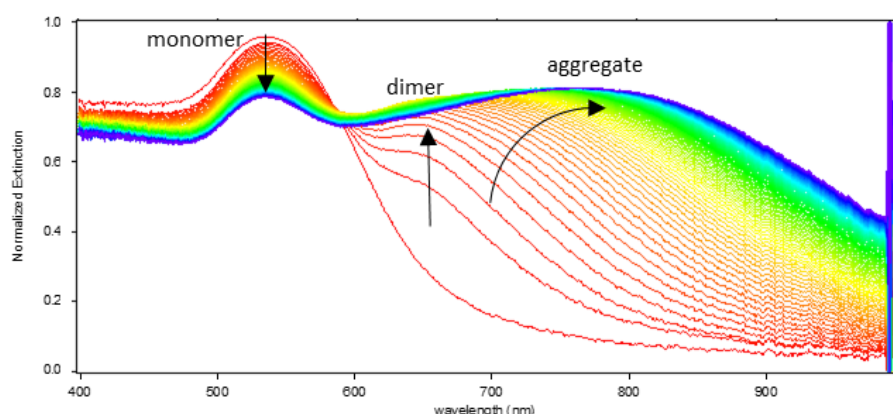
Figure 2.8 Time-resolved extinction spectra during CB[7]-induced AuNPs aggregation (1 mL AuNPs from BBI, 100 µL of 1 mM CB[7], spectra were obtained with 1000 ms interval time and 3 ms integration time)

34
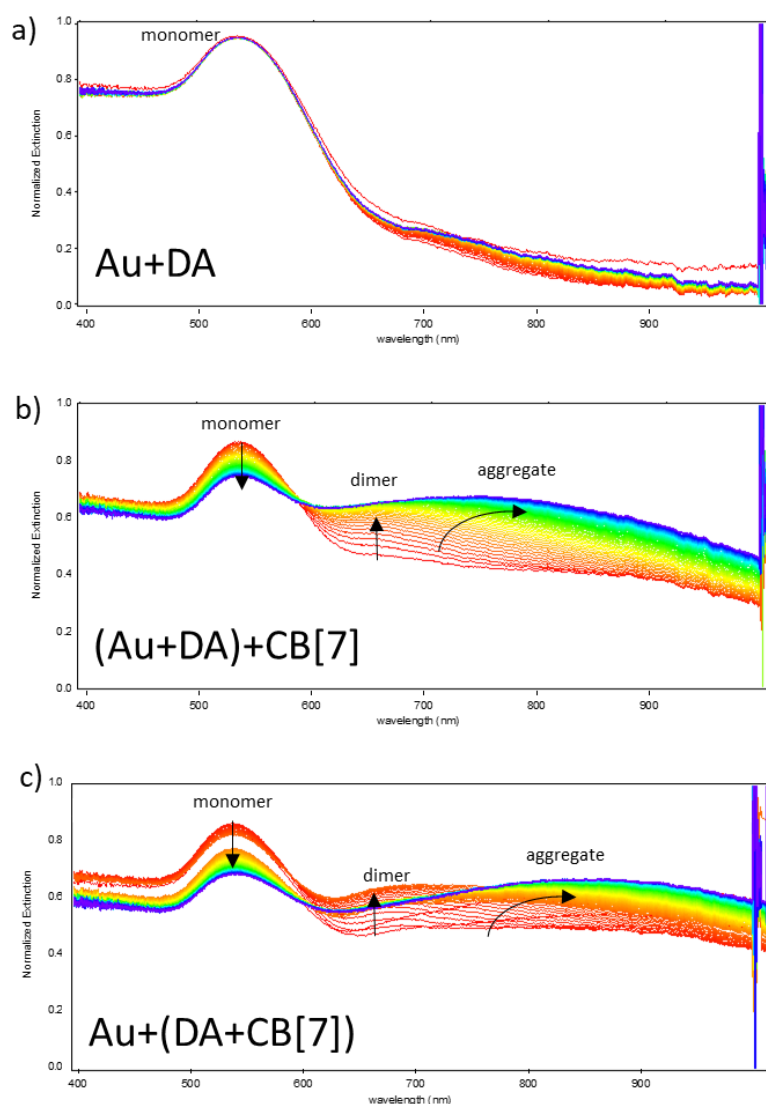
Figure 2.9 Time-resolved extinction spectra of a) AuNPs with dopamine added; b) AuNPs premixed with dopamine and then CB[7] was added to aggregate nanoparticles; c) CB[7] premixed with dopamine and then adding into AuNPs to form aggregates. (1 mL AuNPs from BBI, 100 µL of 1 mM CB[7], 50 µL of 1 µM dopamine, spectra were obtained with 1000 ms interval time and 3 ms integration time)

Similarly, for the system involving dopamine analytes, the UV-Vis extinction spectra of AuNPs aggregates were also investigated. In Figure 2.9a, it shows the time-resolved extinction spectra of AuNPs with dopamine added, in which only one mode 'monomer' mode is observed, indicating that AuNPs are not aggregated in the system when only low concentration dopamine is added. Figure 2.9b shows the time-resolved extinction spectra of the system where AuNPs premixed with dopamine and then CB[7] was added into the mixture. The spectra show a similar trend to that seen in Figure 2.8, where all of three modes 'monomer', 'dimer' and 'aggregate' show when aggregates are formed, and the 'aggregate' mode red-shifts as chains get larger. This result means that the addition of low

35

concentration of dopamine does not influence the CB[7] induced AuNPs aggregation process and aggregation result. However, the spectrum gaps between every two scans are significantly smaller in Figure 2.9b than in Figure 2.8, which indicates that during a certain aggregating time, the involvement of dopamine can slow down the aggregating process of CB[7]-AuNPs. This is due to the strong interaction between dopamine molecules and CB[7] molecules, and the 'glue' ability to AuNPs of host molecule CB[7] is decreased by being occupied by guest molecule dopamine. The same result applies to Figure 2.9c, which shows the time-resolved extinction spectra of the system where CB[7] is premixed with dopamine and then adding into AuNPs to form aggregates. Premixing dopamine with CB[7] still allow CB[7] to aggregate AuNPs, however the aggregating speed is even more slowed down.
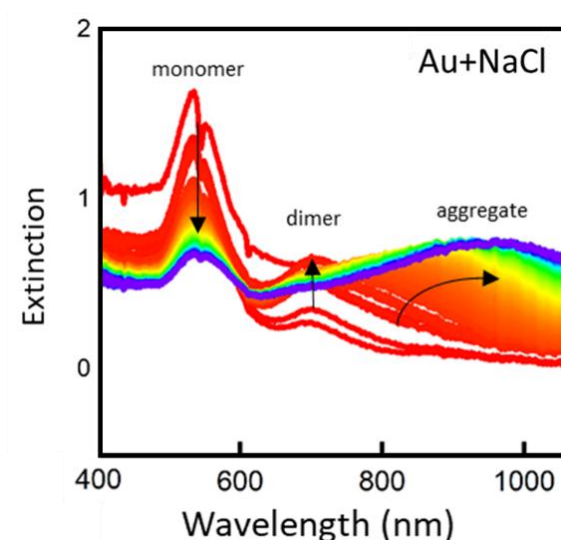
Figure 2.10 Time-resolved extinction spectra during NaCl-induced AuNPs aggregation. (1 mL AuNPs from BBI, 200 μL of saturated NaCl solution, spectra were obtained with 1000 ms interval time and 3 ms integration time.)

NaCl is a most commonly used chemical to aggregate AuNPs due to its strong ability to shield the surface charge of AuNPs and lead to a concomitant decrease in inter-particle distance.[140] Therefore, NaCl induced AuNPs aggregating process was also investigated by time-resolved extinction spectra, as shown in Figure 2.10. Three modes can all be observed in the result, however the 'dimer' mode is shown at around 700 nm wavelength which is 20 nm longer than that of CB[7]-induced aggregates dimer mode 680 nm. This is because the inter particle gap size of NaCl-induced aggregates are smaller than that of CB[7]-induced aggregates. For CB[7] induced aggregates, the gap size is equal or more than the height of the CB[7] molecule, 0.91 nm. However, for citrate capped AuNPs aggregates, even though there might be multiple layers of citrate in the gap of Au nanoparticles, the gap size can hardly exceed 0.91 nm. Therefore, the NaCl-induced aggregates 'dimer' peak position is red-shifted compared to that of CB[7] induced aggregates.

2.4 Dopamine SERS sensing with AuNPs aggregated by NaCl

After understanding the assembly process of AuNPs aggregates, dopamine SERS detection based on AuNPs aggregates were carried out. In this section, dopamine SERS detection by NaCl-induced AuNPs aggregates will be systematically analysed. For reference, the DA Raman results with non-aggregated AuNPs are shown in Figure 2.11a. Figure 2.11b shows DA SERS results by NaCl-induced AuNPs aggregates. For Figure 2.11a, five different dopamine concentrations from 0 µM to 1000 µM were measured.

This demonstrates that non-aggregated AuNPs with no dopamine or low concentration of dopamine (100 µM) show weak SERS spectra apart from a solvent background with no obvious Raman/SERS peaks. The Raman/SERS peaks can be clearly identified for samples with concentrations above 250 µM, which is however, still far from the physiological dopamine concentration 0.01-1 µM. This is because for non-aggregated AuNPs, there is no SERS hot spots for dopamine to sit in, so the Raman intensity shows little enhancement. However, compared with Figure 2.7a where the system has no AuNPs involved, dopamine Raman signals of 1 mM sample with AuNPs are much stronger than that of 25 mM without AuNPs. This signal enhancement for a high dopamine concentration sample is because at high dopamine concentration this has a higher ion strength which can trigger AuNPs assembly, so that these aggregated AuNPs can provide hot spots which help to enhance the dopamine Raman signals. However, compared to Figure 2.11b, where AuNPs are pre-aggregated by NaCl, the signal of 1 mM dopamine with non-aggregated AuNPs is 2 times weaker than that of 10 µM dopamine with NaCl aggregated AuNPs. This is because 1 mM dopamine can only help to partially aggregate AuNPs due to its weaker ion strength than saturated NaCl, so the signal enhancement by dopamine-induced aggregates is limited.

The AuNPs aggregates itself shows clear SERS peaks as shown in Figure 2.11b (red spectrum) even with no analyte added in. This is because AuNPs solution contains various chemicals, such as citric acid, ascorbic acid, etc. and these exhibit Raman signal which can be enhanced by AuNPs aggregates, thus the red spectrum shows the signals of components originally existed in AuNPs solution. To estimate the LOD for dopamine SERS based on NaCl-induced aggregates, PCA analysis was carried out as described in section 2.2. Figure 2.11c shows PC1 scores change significantly along dopamine concentration when it is above 1 µM, so the LOD is around 1 µM, which is close to our target in physiological environments.
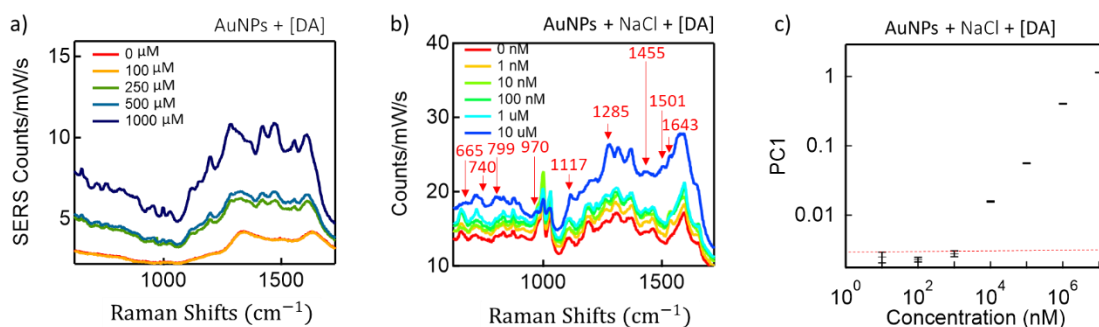
Figure 2.11 a) Dopamine SERS concentration series by non-aggregated AuNPs. b) Dopamine SERS concentration series by NaCl-induced AuNPs aggregates. c) PCA analysis PC1 vs dopamine for spectra in Figure b), with noise level dashed.

The red arrows in Figure 2.11b mark the new peaks shown in the spectrum of 10 μM dopamine sample (dark blue) compared to that of no dopamine sample (red). Nine new Raman peaks were found and these are listed in Table 2.3. These are identical as pure dopamine and DFT calculations for Raman spectra of AuNPs-dopamine complexes were carried out to help find out the assignments for these 9 peaks. The DFT calculations were simplified by only taking Au and dopamine molecules into account. Dopamine has 3 possible binding sites to Au surface: meta-position phenolic hydroxyl group (mO-Au), para-position phenolic hydroxyl group (pO-Au), and amino group at the end of aliphatic chain (N-Au). When only one of these 3 binding sites binds to Au atom, the other two sites are free and form 1 binding site complexes, as shown in Figure 2.12. When two of these 3 sites bind to the Au and the rest one site is free and form 2 binding sites complexes, as shown in Figure 2.13. When all of the three sites bind to the Au, a 3 binding sites complex is formed as shown in Figure 2.14. DFT SERS results for all these 7 complexes can be correlated to experimental SERS data of dopamine-AuNPs(NaCl) mixture, as all the black dashed lines indicate in Figure 2.12-2.14, so that measured SERS peaks can be assigned to specific chemical bond vibrations, as shown in Table 2.3. These assignments can not only help to understand the SERS signals from Au-dopamine complexes, but also can help to analyse dopamine SERS signals from other more complicated complexes involving CB[n] or Fe(III) in the following chapter.

The dominant complexes in the system can be estimated by comparing the matching peak numbers of all 7 complexes. Single site binding mode mO-Au and all three 2 sites binding modes have the most matched peaks with the experimental data, compared to other 3 modes. Therefore, the 'real world system' can be formed mostly by 2 sites Au-dopamine binding modes and single site binding mode mO-Au, with fewer other 3 binding modes.
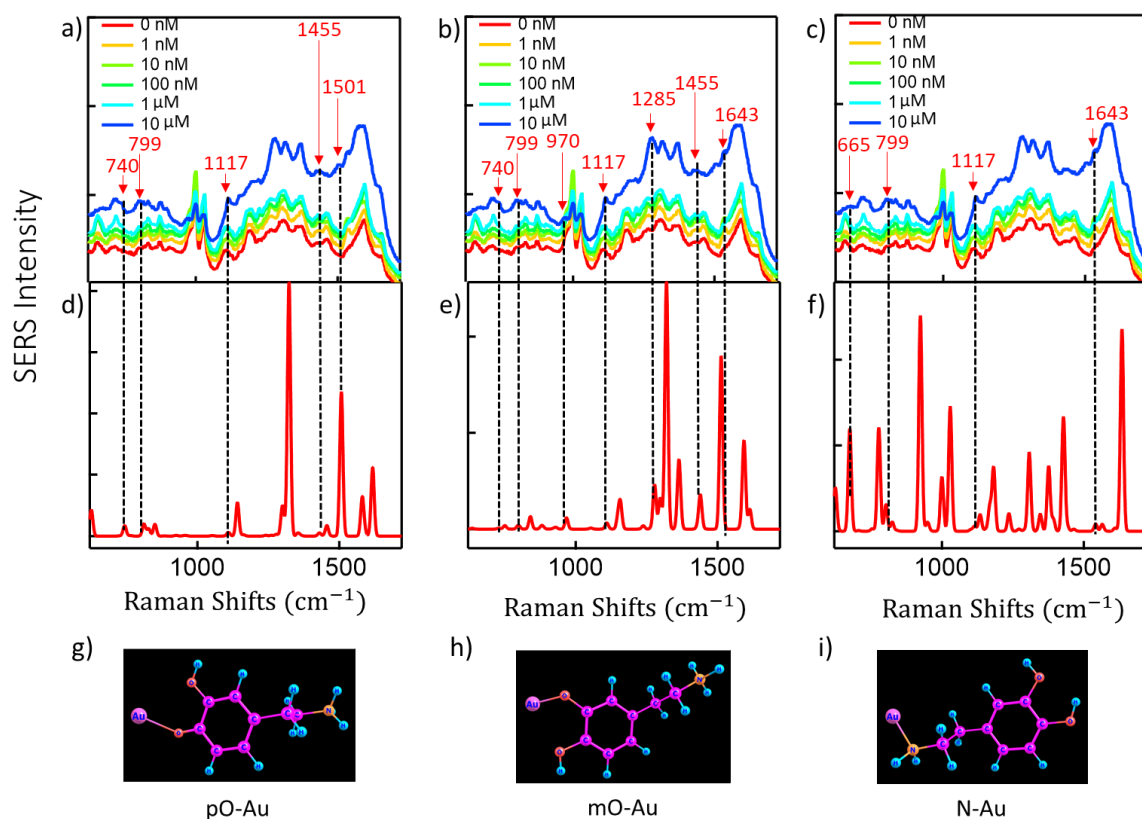
Figure 2.12 a-c) Dopamine SERS concentration series by NaCl-induced AuNPs aggregates. d-f) DFT calculations results for 1 binding site Au-dopamine complexes: po-Au, mo-Au and N-Au respectively. Dashed lines match the experimental peaks with simulation results. g-h) Complex schematic of po-Au, mO-Au and N-Au respectively. DFT calculations were carried out with dried samples (no water molecules involved).
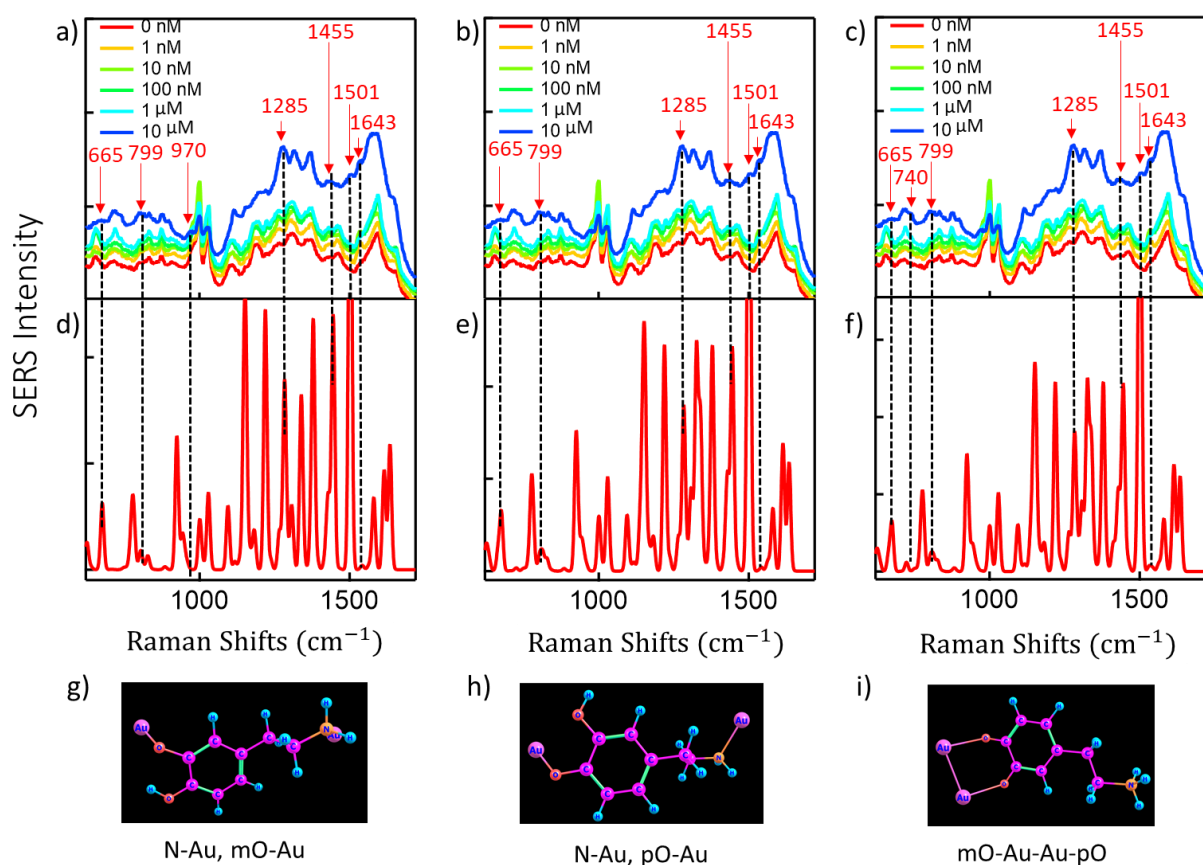
Figure 2.13 a-c) Dopamine SERS concentration series by NaCl-induced AuNPs aggregates. d-f) DFT calculations results for 2 binding sites Au-dopamine complexes: d) N-Au, mO-Au, e) N-Au, pO-Au and f) mo-Au-Au-pO respectively. Dashed lines match the experimental peaks with simulation results. g-i) Schematics of 2 binding sites Au-dopamine complexes: g) N-Au, mO-Au, h) N-Au, pO-Au and i) mo-Au-Au- pO respectively. The exact atom were noted on each sphere in graph g to i. DFT calculations were carried out with dried samples (no water molecules involved).
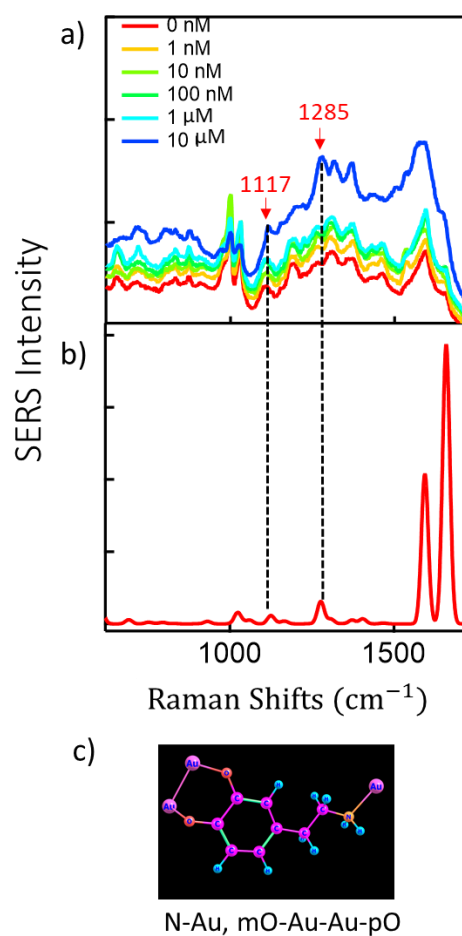
Figure 2.14 a) Dopamine SERS concentration series by NaCl-induced AuNPs aggregates. b) DFT calculations result for 3 binding sites Au-dopamine complexe N-Au, mo-Au-Au-pO. Dashed lines match the experimental peaks with simulation results. c) Schematic of 3 binding sites Au-dopamine complexe N-Au, mo-Au-Au-pO. DFT calculations were carried out with dried samples (no water molecules involved).

Raman Shifts (cm^{-1})	pO-Au	mO-Au	N-Au	N-Au, mO-Au	N-Au, pO-Au	mO-Au-Au-pO	N-Au, mO-Au-Au-pO
665			HNH twisting				
740	pO-C-C-mO stretching					pO-C-C-mO stretching	
799	In-plane benzene stretching; pO-Au stretching						
970		In-plane benzene stretching;		In-plane benzene stretching;			

		mO-Au stretching		mO-Au stretching		
1117	CH in-plane ring deformation, C-O-H bending					CH in-plane ring deformation, C-O-H bending
1285		C-OH stretching, CH in-plane ring deformation		C-OH stretching, CH in-plane ring deformation		
1455	NH bending aromatic C=C stretching and C-H scissoring			aromatic C=C stretching and C-H scissoring	NH bending aromatic C=C stretching and C-H scissoring	
1501	CC in-plane ring deformation			CC in-plane ring asymmetric deformation		
1643		CC in-plane ring symmetric deformation; O-H scissoring				

Table 2.3 Assignments of dopamine SERS peaks to binding modes and chemical bonds vibration modes.

2.5 Dopamine SERS sensing with AuNPs-CB[n]-dopamine complex

Since dopamine can bind to CB[n] via host-guest chemistry, it is potential to further improve the Au-dopamine binding strength by CB[n] which have stronger binding affinity to Au. Therefore, the same concentration series for dopamine SERS sensing were carried out to achieve a lower LOD. Two different CB[n] molecules, CB[5] and CB[7] were tested. The reason to choose these two CB[n] molecules is that they have higher solubility in water than CB[6] and CB[8][120]. To be specific, CB[5] and CB[7] exhibit a water solubility of 25 mM and 30 mM respectively, compared to 0.02 and 0.01 mM for CB[6] and CB[8] respectively.

To obtain best SERS signals, the host molecule concentration can neither be too low or too high. A low concentration of CB[n] would not provide enough host cavities for guest molecules so may limit the number of analytes sitting into hotspots and limit the analytes SERS signals. Low concentration of CB[n] also does not have enough ability to aggregate large amount of AuNPs, so the aggregating process could be either very slow or not complete, which limit the formation of hotspots. High concentration of CB[n], on the other hand, may immediately fully cover the single AuNPs surface once two solutions are mixed, so AuNPs become hydrophobic with high coverage of carbonyl groups, which in contract

will inhibit the aggregation of AuNPs. This can be proved by CB[n] SERS spectra data as shown in Figure 2.15 a) and c), which respectively show CB[7] and CB[5] SERS spectra of different CB concentrations for system 'AuNPs+CB[n]'. Peak 829 cm^{-1} is shown in both spectra, which is a characteristic peak of CB[n] SERS spectra. As CB[n] concentrations increase from 0 to 1mM, 829 cm^{-1} intensity firstly increase and then decrease, peaking at concentration of 250 μM and 100 μM for CB[7] and CB[5] respectively, as the black lines show in Figure 2.15 e and f.

To optimise the dopamine SERS signal, finding the optimised CB[n] concentration is important. The optimised CB[5] and CB[7] concentration for SERS signals were explored for 'AuNPs+CB[n]+dopamine' system, as shown in Figure b and d, which respectively show CB[7] and CB[5] SERS spectra of different CB[n] concentrations for fixed dopamine concentration 1 mM in system 'AuNPs+CB[n]+dopamine'. Dopamine's characteristic peak 1455 cm^{-1}, as well as CB[n] Peak 829 cm^{-1}, is shown in both spectra. As CB[n] concentrations increase from 0 to 1 mM, 1455 cm^{-1} intensity also firstly increase and then decrease, peaking at concentration of 125 μM and 10 μM for CB[7] and CB[5] respectively, as the orange lines show in Figure 2.15e and f. Therefore, in the following dopamine SERS detecting experiments, CB[7] is fixed to 125 μM and CB[5] is fixed at 10 μM.
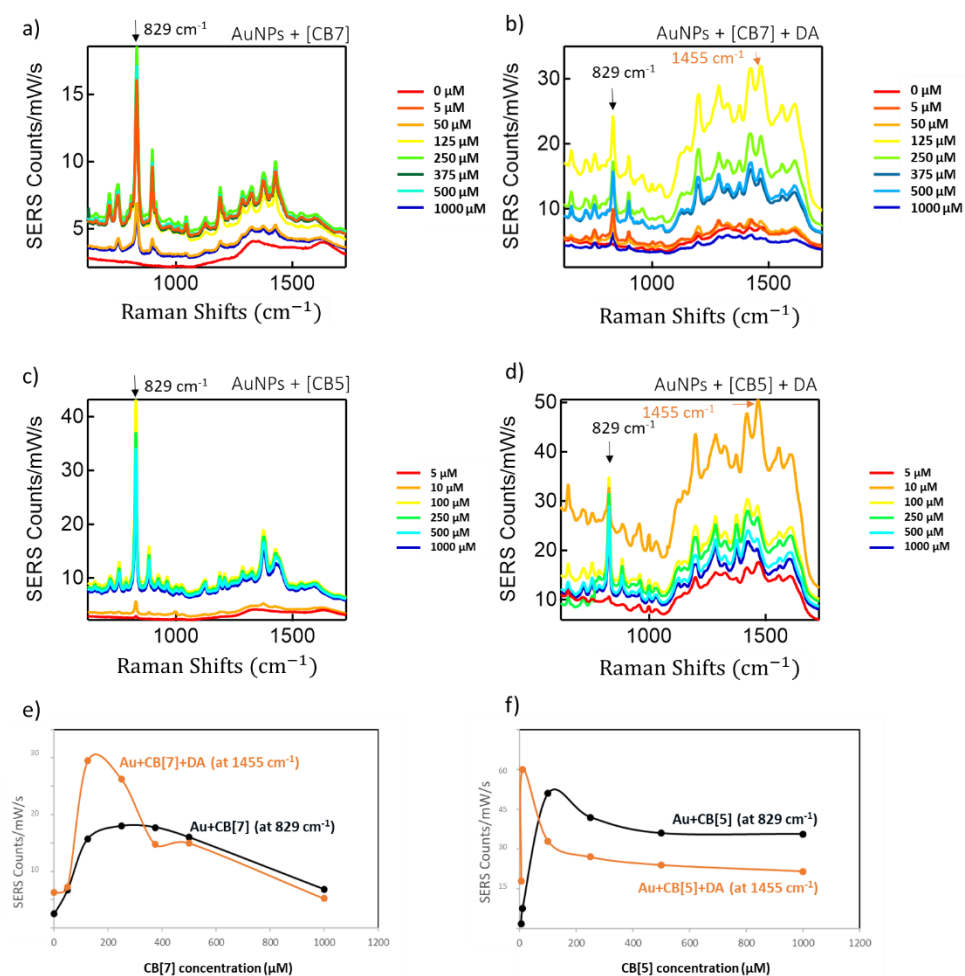
Figure 2.15 a) CB[7] and c) CB[5] concentration series for SERS with 60nm (300 μL 60 nM BBI AuNPs mixed with 15 μL CB solution in plate well). b) CB[7] and d) CB[5] concentration series for dopamine SERS with 60nm AuNPs (300 μL 60 nM BBI AuNPs mixed with 15 μL CB solution firstly in plate well for 10 min, and then 15 μL of 1 mM dopamine solution was added). e) SERS intensity of dopamine peak at 1455 cm^{-1} and CB[7] peak at 829 cm^{-1} vs CB[7] concentration. f) SERS intensity of dopamine peak at 1455 cm^{-1} and CB[5] peak at 829 cm^{-1} vs CB[5] concentration.

Figure 2.16 a and b) SERS spectra of dopamine from 0 μM to 1000 μM by protocol PreNP and protocol PostNP respectively for CB[7] system. c and d) SERS spectra of sample without analyte, PC0 and PC1 after PCA analysis, by protocol PreNP and protocol PostNP respectively. e and f) PC1 scores vs dopamine concentration with noise level dashed, for protocol PreNP and protocol PostNP respectively.

The dopamine SERS concentration series were then carried out to determine the LOD for Au-CB[n]-dopamine complex system. The following two protocols of different adding orders were examined:

Protocol PreNP: 300 μL of 60nm AuNPs solution was first mixed with 15 μL CB[n] solvent to form AuNPs-CB[n] aggregates. After waiting for 10 min, 15 μL dopamine solution was added and mixed adequately.

Protocol PostNP: 15 μL dopamine was first mixed with 15 μL CB[n] solution to form host-guest molecule complexes. After waiting for 10 min, 300 μL AuNPs was added to form aggregates.

SERS spectra of dopamine from concentration 0 to 1000 μM are shown in Figure 2.16 a) and b), which shows the results of protocol PreNP and protocol PostNP respectively for CB[7] system. By doing PCA analysis, PC0 representing background spectra and PC1 representing dopamine signals are shown in Figure 2.16 c) and d). Figure 2.16 e) and f) show the PC1 scores change along dopamine concentration and they both show the LOD at 0.1 to 1 μM, which is within the range of physiological dopamine concentration in urine. Therefore the adding orders of AuNPs, CB[7] and dopamine have little influence on dopamine SERS sensing sensitivity. However, protocol PostNP shows stronger intensity and higher reproducibility than protocol Prenp, based on the data obtained at the same dopamine concentration in Figure 2.16 e) and f).
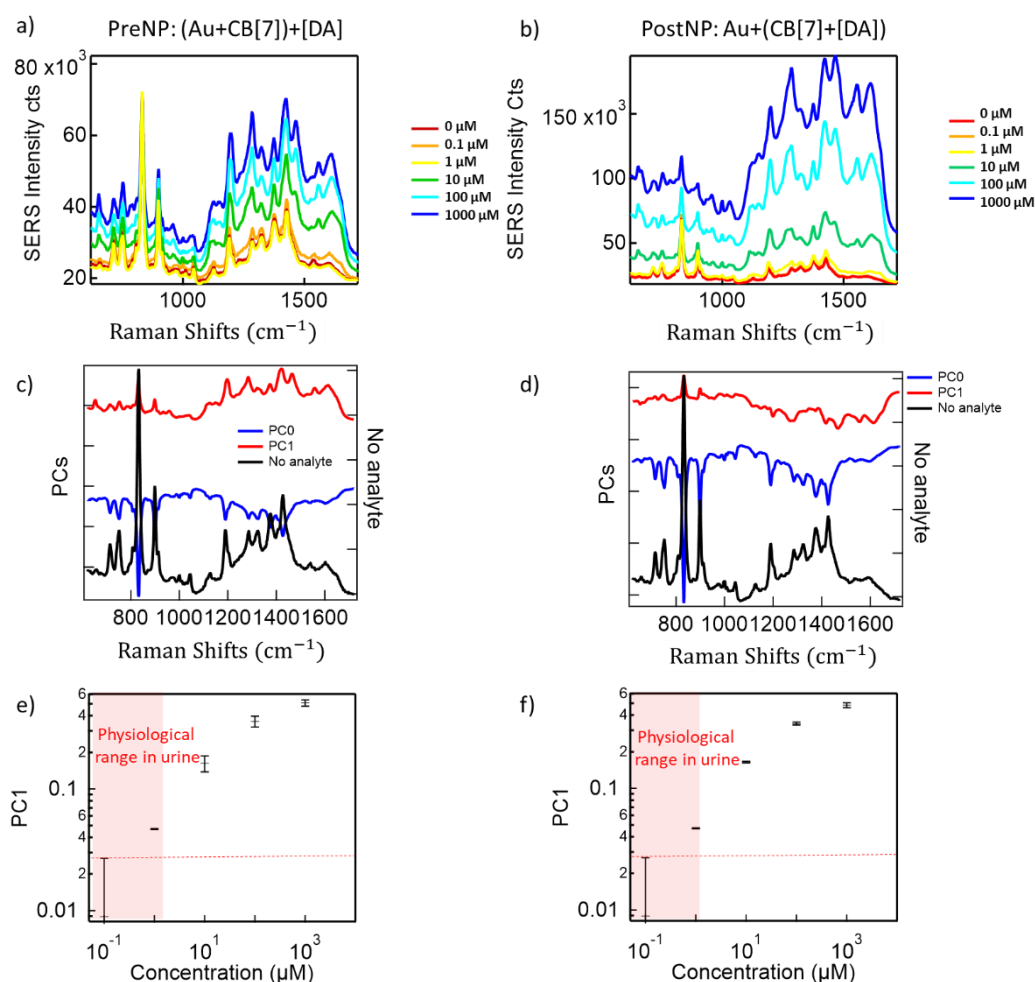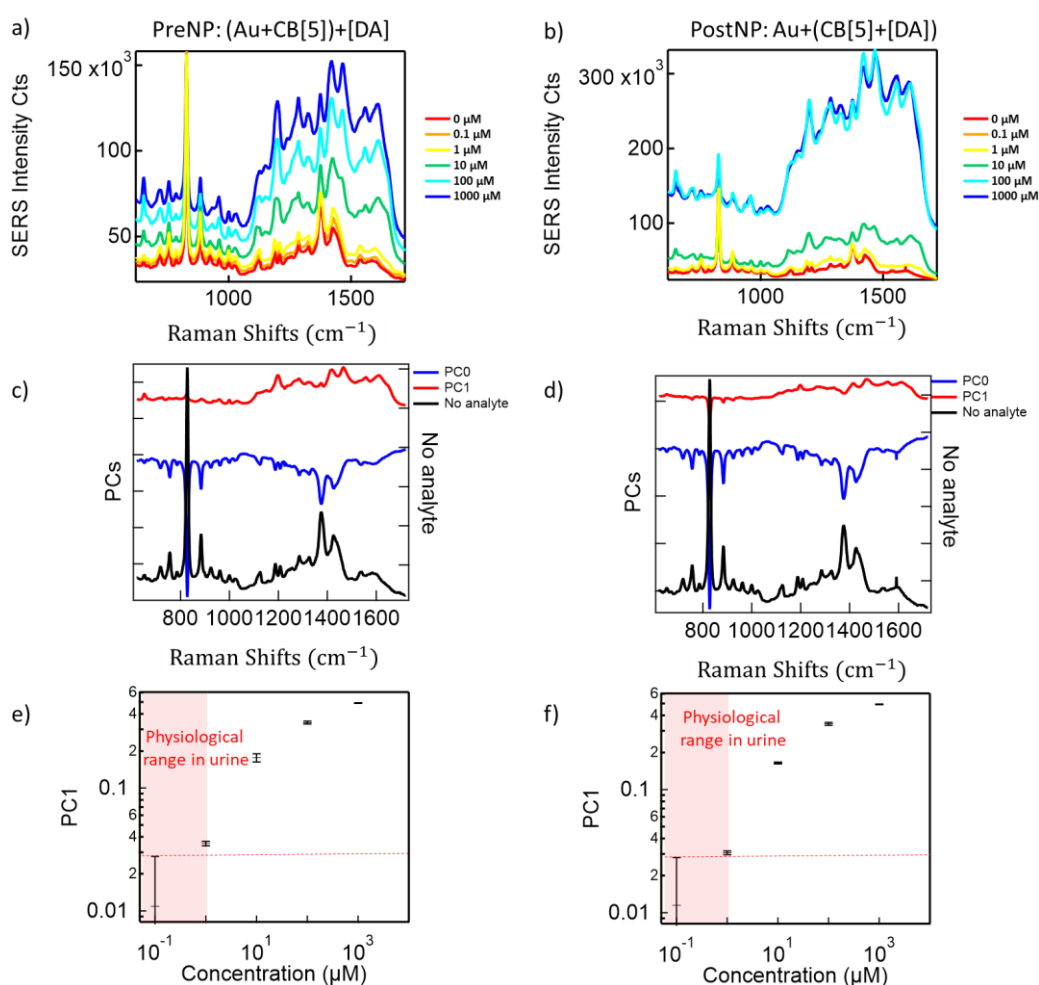
Figure 2.17 a and b) SERS spectra of dopamine from 0 μM to 1000 μM by protocol PreNP and protocol PostNP respectively for CB[7] system. c and d) SERS spectra of sample without analyte, PC0 and PC1 after PCA analysis, by protocol PreNP and protocol PostNP respectively. e and f) PC1 scores vs dopamine concentration with noise level dashed, for protocol PreNP and protocol PostNP respectively.

The same experiments were carried out for CB[5] and the results are similar as that of CB[7], which also can help get to the LOD at 0.1 to 1 μM (See Figure 2.17). From all the above results, the conclusion can be drawn that CB[n] molecules can help to increase dopamine SERS sensitivity by 1 order of magnitude compared to NaCl-induced AuNPs aggregation, reaching to the level of physiological dopamine concentration.

2.6 Dopamine SERS sensing with Dopamine-Fe(III)-Citrate-AuNPs complex

Apart from dopamine-AuNPs (NaCl-induced aggregates) and AuNPs-CB[n]-dopamine complexes, Fe(III) was also found to be an excellent binding agency for dopamine and AuNPs, as introduced in sector 2.1.3.2 The protocols, the binding mechanism, and the sensing results will be discussed in the following section.

2.6.1 Two protocols PreNP and PostNP

As in section 2.5, Protocol PreNP and PostNP were applied in this new system as described below. The difference between the two protocols is the order of addition of Fe(III) in the system (see Section 7.2 for details).

Protocol PreNP (Figure 2.18a): AuNPs solution was first mixed with $Fe(NO_3)_3$ solution to form AuNPs-citrate-Fe(III) complexes. Saturated NaCl solution then was added to aggregte AuNPs. After 10 min, dopamine (NT, neurotransmitter) solution was added and SERS spectra were measured.

Protocol PostNP (Figure 2.18a): Dopamine solution was first mixed with $Fe(NO_3)_3$ to form Fe(III)-DA complexes (either monomer, dimer or trimer depending on the pH). Meanwhile as shown in step 2, saturated NaCl solution was mixed with AuNPs to form aggregates. The mixture of Fe(III) and dopamine was moved into the aggregates. SERS spectra were then measured after 10 min of mixing.

Figure 2.18b-d) show DA SERS spectra of different concentrations, by protocol Fe(III) omitted as shown in b), by protocol PreNP as shown in c), by protocol PostNP as shown in d). Generally, compared to DA SERS spectra from protocol with Fe(III) omitted, protocol PreNP gives 10 times higher signal intensity and protocol PostNP gives 20 times higher signal intensity. This suggests that although DA is likely to adsorb onto citrate via electrostatic attraction, the affinity between DA and citrate is weak. Much stronger binding between Fe(III) - citrate and Fe(III) - DA suggests it provides an improved way to bind

DA to the surface of AuNPs, thus giving SERS signals thousands of times larger with Fe(III) included. The assignments of these dopamine peaks can be found back in Table 2.3.

PCA was further utilized for the data analysis. PC1 vs dopamine concentration for all 3 protocols were plotted as Figure 2.18e and f. The assay without Fe(III) has the lowest score even at high DA concentrations and it saturates above 1 μM, with the best LOD ~100 nM. Since this is not enough for the clinical range demanded, it shows that despite being an efficient SERS substrate for a wide variety of other molecules, DA is hard to access the hotspots and thus a further advance is required.

Incorporating Fe(III) in the assay delivers this enhancement, with protocol PreNP giving the lowest LOD of < 1 nM, whilst PostNP gives LOD~10 nM. Therefore, both protocol PreNP and PostNP can reach the dopamine concentration range of physiological degree. Usefully, PreNP also has a wider dynamic range of measurable DA concentrations than PostNP. This suggests PreNP provides a more accessible pathway for DA to attach to the gap surfaces of aggregated AuNPs. Pre-coating Fe(III) on AuNPs may support surface attachment followed by surface migration into hotspots. By contrast as we now discuss, in the PostNP protocol DA already exists in solution as a mono-, bis- or tris-complex with Fe(III). This may account for the lower dynamic range from PostNP as steric effects can then limit the fraction of Fe(III)-bound DA which binds to the AuNPs and migrates into the hotspots.
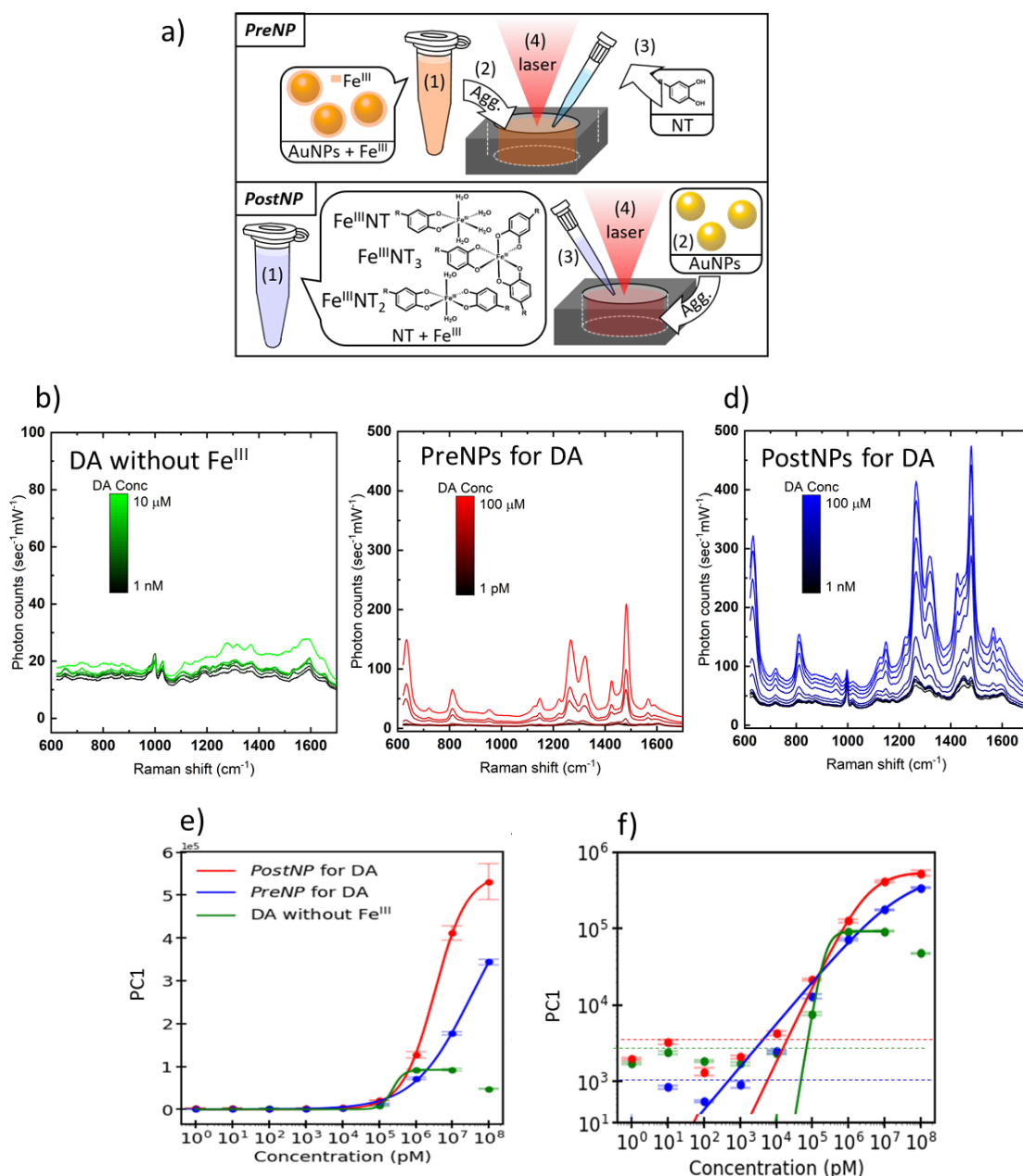
Figure 2.18 a) Two protocols used for sensing DA: PreNP: (1) AuNPs pre-incubated with Fe(III), (2) then aggregated using NaCl, (3) NTs were added, and mixed thoroughly. PostNP: (1) NTs pre-incubated with Fe(III), creating Fe(III)NT, Fe(III)NT2 and Fe(III)NT3 complexes, (2) AuNPs separately aggregated using NaCl, then (3) Fe(III)NT complexes added to the aggregate solution and mixed thoroughly. In both cases the final step (4) focusses a 785 nm laser into the solution to obtain SERS. b) DA SERS spectra with Fe(III) omitted (meaning AuNPs firstly aggregated by NaCl, DA then added to the aggregation solution for SERS measurements), c) DA SERS spectra by PostNP, and d) DA SERS spectra by PreNP. e) Scores of PC1 from spectra in b-d) vs spiked DA concentrations. f) A log–log plot of e), with noise levels dashed.
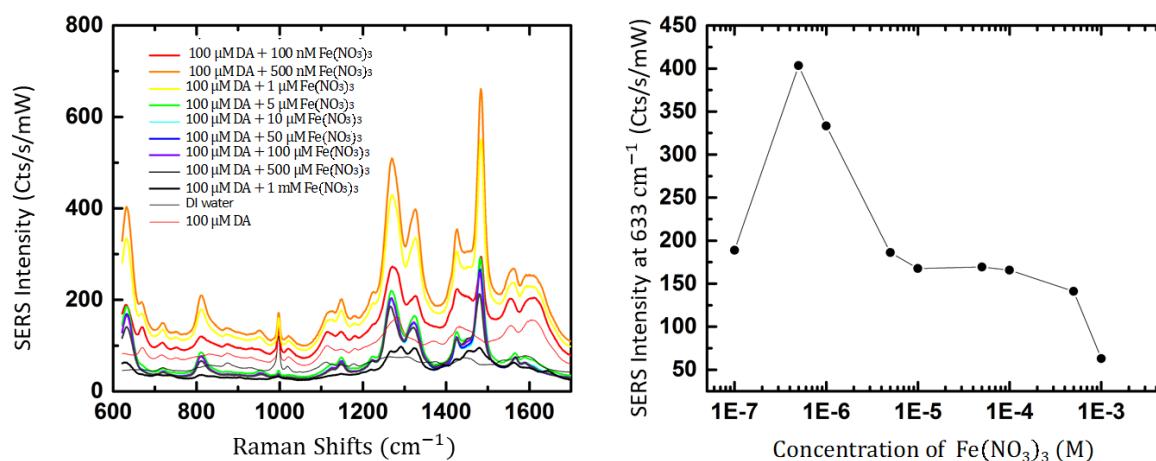
Figure 2.19 By PostNP protocol, a) 100 μM DA SERS spectra influenced by the concentration (0 – 1mM) of Fe(III) when it is pre-incubated with dopamine. b) DA SERS peak 633 cm^{-1} intensity changes along with concentration change of Fe(III).

To get the best DA SERS spectra, the concentration of Fe(III) was always optimised beforehand since it has significant influence on DA SERS signal intensity. For example, with protocol PostNP, Figure 2.19a shows different DA SERS spectra by adding different concentrations of Fe(III) (from 0 to 1mM), and Figure 2.19b shows SERS peak intensity at DA 633 cm^{-1}. DA shows strongest SERS signal when the Fe(III) concentration is 100 uM. This is because lower concentration of Fe(III) could not provide enough 'Fe(III) glue' to bind DA to Au surface so the DA shows relatively weak SERS signals, and on the other hand concentrations of Fe(III) higher than 100 μM result in unwanted Fe(III)-induced aggregation of AuNPs through screening-induced reduction of their Coulomb barriers, which dramatically decreases the ability of Fe(III) to capture DA into hotspots. Overall, there is an optimised Fe(III) concentration for the best DA SERS sensing, which is 100 μM in my experimental condition.

2.6.2 Characterisation of Fe(III)-DA complexes in solution at various pH

The key role of Fe(III) complexation in enhancing this DA assay requires a careful characterisation of the complexes between Fe(III) and DA that are formed in the pre-incubation stage of PostNP.
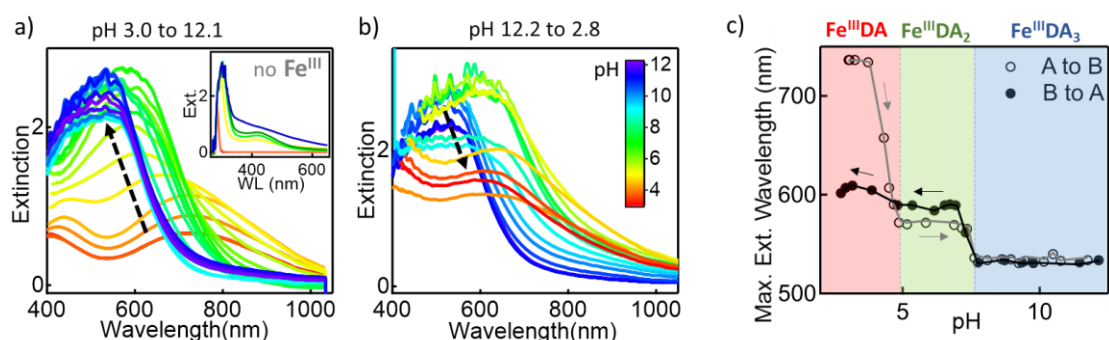
Figure 2.20 Evolution of the extinction spectra of the complexes of DA and Fe(III) in a) acidic to basic (A to B), and b) basic to acidic (B to A) pH titration. Inset of a) shows pristine DA without Fe(III). c) Extinction spectra peak wavelengths from (a, b) vs pH. Regions where Fe(III)DA, Fe(III)DA2 and Fe(III)DA3 dominate shaded red, green and blue. See experimental details in Section 7.3.

As stated in Figure 2.4, the Dopamine-Fe(III) complexes mode is highly dependent on pH. UV-Vis extinction spectra (See Section 7.8 for experimental details) of these complexes of Fe(III) and DA are measured as the solution pH is titrated from acid to base (Figure 2.20a) and base to acid (Figure 2.20b). In the UV–vis range, according to literature the mono-complex has doublet peaks at 406 nm and 759 nm, whilst the bis- and tris-complexes have single peaks at 575 nm and 492 nm respectively[136]. The fraction of these species in different solution pH can thus be extracted (Figure 2.20c), giving three regions in a step-like curve (shaded colours denote the Fe(III)DA, Fe(III)DA2 and Fe(III)DA3 regions). Interestingly, pH titration from base to acid does not completely reverse to the original acid state. This is likely due to irreversible oligomerisation between DAs bound via Fe(III) at high pH. Several hours are needed for full DA polymerisation (pDA) at pH > 10[141] , so during the 30-minute measurement here DA disassociated from Fe(III) partially oligomerises and cannot return to the monomer even at low solution pH.

2.6.3 Raman scattering/SERS of Fe(III)-DA complexes

Despite the clear involvement of Fe(III) in bringing DA into the plasmonic gaps, it is so far unclear in which form it is bound. Raman spectroscopy at 785 nm is thus now used to check the gap contents.
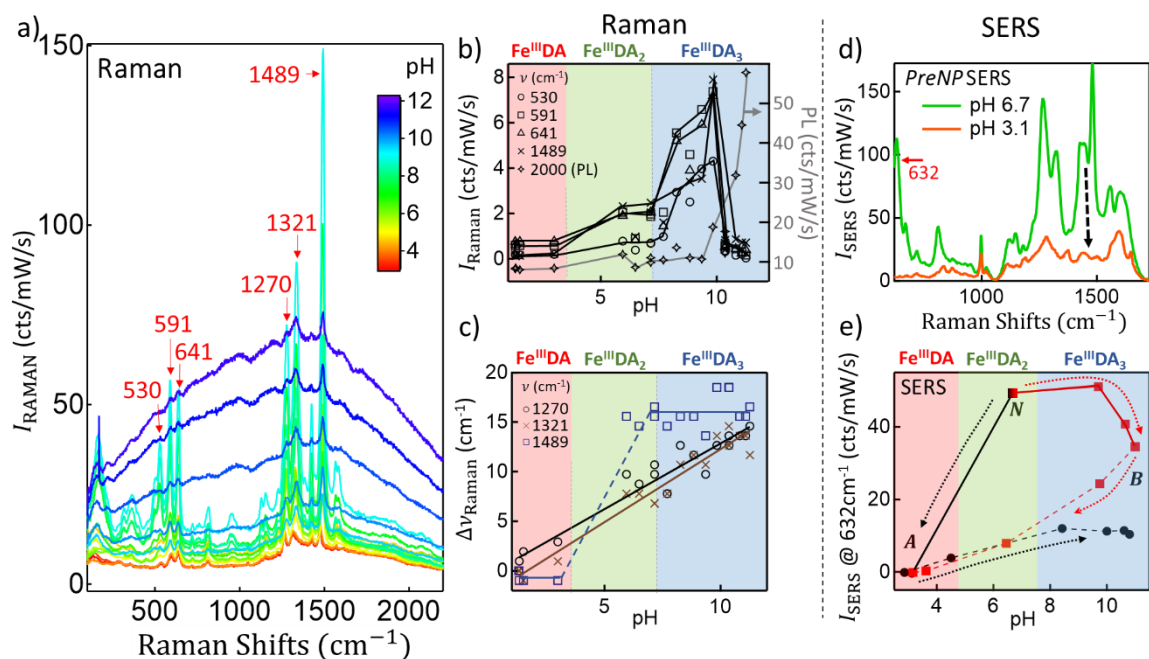
Figure 2.21 a) Evolution of Raman signals from Fe(III)-DA complexes vs pH at 50 mM DA with 50 mM Fe(III). b) Raman intensity of 530, 591, 641, 1270, 1321, 1489 cm^{-1} lines (arrows in a) as solution pH changed from acid to base. c) Shift of Raman peaks initially at 1270, 1321, 1489 cm^{-1} vs pH. Red, green, blue regions indicate Fe(III)DA, Fe(III)DA2, Fe(III)DA3 dominating species. Lines are guides to eye. d) SERS of DA obtained from protocol PreNP at pH 3.1 and 6.7. e) SERS intensity of DA at 632 cm^{-1} as pH changed from neutral (N) to base (B) (red squares, then to acid, dashed), and from N to acid (A) (black circles, then to base, dashed).

Initially the Raman spectra was calibrated with the Fe(III)-DA complexes in solution without AuNPs (Figure 2.21a). The covalent coordination binding is through lone pair electrons between the central Fe(III) and the deprotonated hydroxyls of DA (Figure 2.18a).[136] The Raman intensities increase significantly with increasing solution pH up to 10, particularly for peaks at 530, 591, 641, 1270, 1321 and 1489 cm^{-1} (all absent without DA). This directly tracks the amount of DA bound to each Fe(III), as seen in Figure 2.21b. At lower pH, a higher fraction of the hydroxyl groups is protonated preventing their coordination to Fe(III), leading to a far weaker Raman intensity. This is surprising since the 785 nm laser is near-resonant with electronic transitions seen in adsorption at low pH (Figure 2.20 a&b) which should give resonant Raman, and the result must be due to much higher Raman cross sections for Fe(III)DA3, from electronic delocalisation across the complex. By contrast, the Raman intensity drops suddenly for pH>10 since black sediments forms and Raman signal is overwhelmed by photo luminescence of sediment, which is likely due to polymerisation between DAs (oligomerisation)[141]. The fluorescence generated by these newly-formed oligomers is seen as a rising background under the Raman spectrum (Figure 2.21a, 2000 cm^{-1}). Small spectral shifts ($\Delta v < 1\%$) of the Raman peaks

(Figure 2.21c) show $\Delta v \propto$ pH for 1270, 1321 cm^{-1} but reveal a jump for pH $\approx$ 7 at 1489 cm^{-1} coinciding with regions of dominant Fe(III)DA or Fe(III)DA3.

Compared to the concentrated 1M DA solution required to capture these Raman measurements (LOD ~100 mM), aggregated AuNPs are vital to provide SERS amplification when the analyte concentration is very low, < 1 µM. SERS spectra are typically more complicated and shifted compared to Raman, since signatures of surfactants on AuNPs (e.g. citrates) are also amplified, while chemical shifts from bond hybridisation with the metal also occur. Helpfully, SERS contributions from surfactants are insignificant, and the SERS spectra of Fe(III)-DA complexes in AuNPs match their solution Raman spectra. As before, at low pH DA protonation results in partial dissociation of DA from Fe(III)[136], eliminating the characteristic DA SERS peaks leaving only protonated surfactant molecules peaks.

While SERS peak shifts with pH are absent, the SERS intensities change depending on the direction of pH titration (Figure 2.21e). Initially the colloidal AuNPs are buffered to pH 6.3, and are then shifted in either acidic or basic directions. For increasing pH, the SERS intensity drops irreversibly at pH>10 (no recovery for subsequent pH→3). Minimal SERS increase is seen from pH 6.3 to >7.5, in contrast to the Raman (Figure 2.21b). This suggests that in terms of SERS, the higher Raman cross-section Fe(III)DA3 complex is unable to form, perhaps because at least one of the available DA binding sites on Fe(III) is occupied by surfactant citrates at the AuNPs. Permanent oligomerisation between DAs bound to Fe(III) for pH > 10 seems to kill their Raman cross section, perhaps by detaching them from SERS-enhancing Fe(III). On the other hand, initial acidification to pH 3 protonates DA, cleaving it from Fe(III) so the SERS disappears. It also seems to disassociate the Fe(III) from citrate on the AuNPs because even returning to pH 6 restores <10% of the signal, suggesting the active sites in the gap are now locked up. The optimal PreNP protocol assay is identified around pH~7-8, where multiple DA complexation with Fe(III) is favoured.

DFT calculation at weakly alkaline environment was carried out to correlate to the experimental data, as shown in Figure 2.22. The calculated Raman spectra in Figure 2.22 b shows Raman peaks of trimer mode Fe(III)DA3 complex. These marked peaks can correlate well to experimental data (Figure 2.22 a) which were measured at pH = 7.5, proving again that the dominant species is the trimer binding mode in weakly alkaline environment. The complex molecular structure is shown in Figure 2.22 c and the assignments of these peaks to chemical bonds vibration modes are shown in Table 2.4.
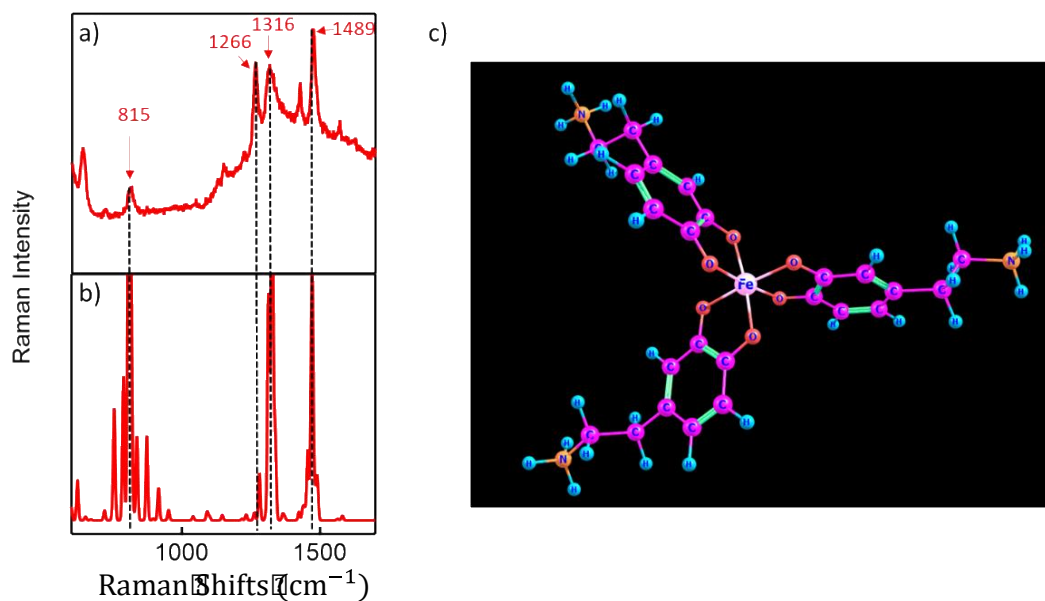
Figure 2.22 Raman spectra of dopamine + Fe(III) mixture from a) experimental measurement of DA+Fe(NO$_3$)$_3$ water solution at pH = 7.5; b) DFT calculation of trimer mode Fe(III)DA3; c) trimer mode Fe(III)DA3complex molecular structure. DFT calculations were carried out with dried samples (no water molecules involved).

Raman Shifts (cm^{-1})	Assignments
815	In-plan benzene stretching; pO-Au stretching
1266	CH in-plane ring deformation
1316	NH bending
1489	CC in-plane ring asymmetric deformation

Table 2.4 Assignments of DA+Fe(III) Raman peaks to chemical bonds vibration modes

2.6.4 Proposed mechanisms for binding of Fe(III) and DA
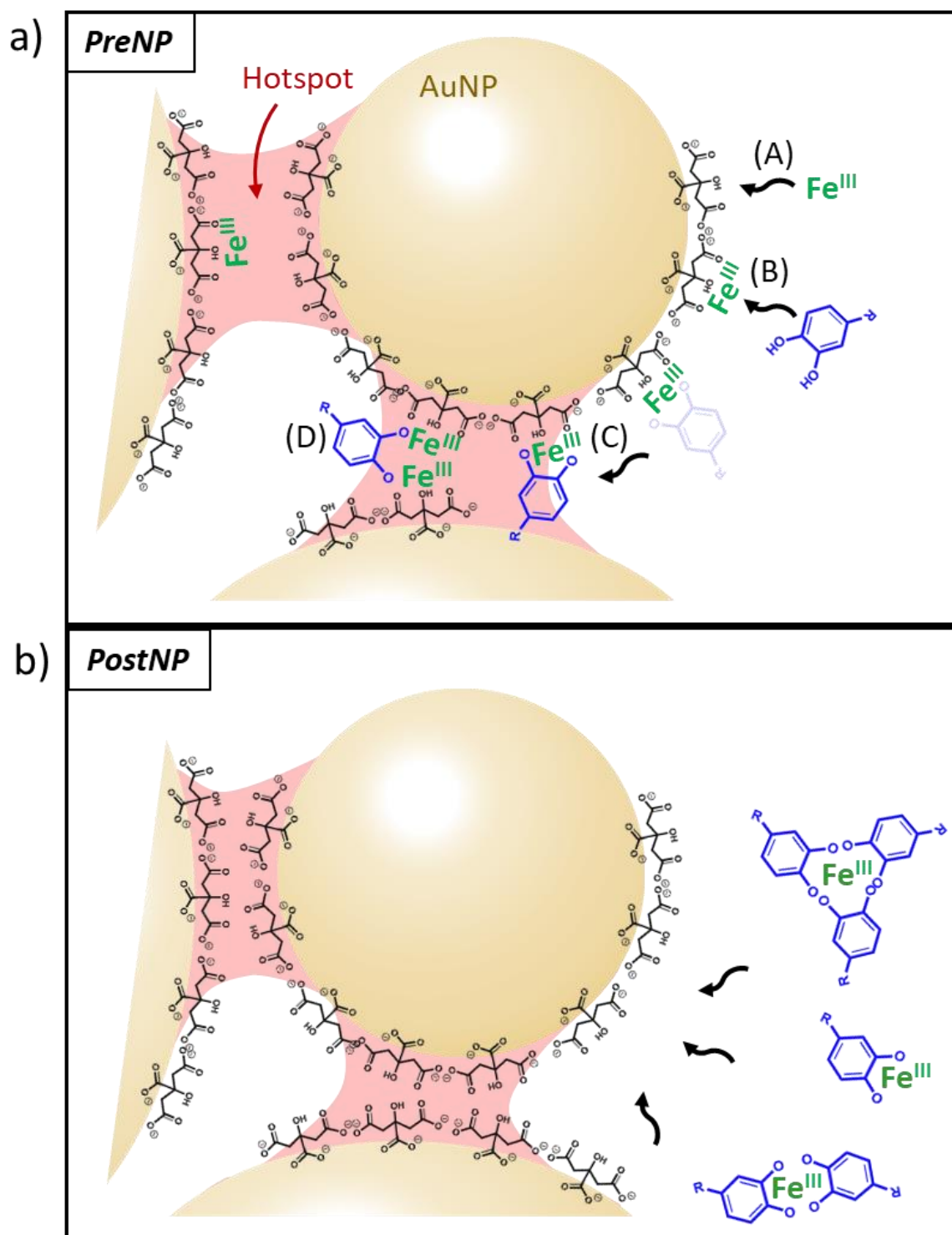
Figure 2.23 Proposed sequestration of DA in optical hotspots between aggregated AuNPs comparing PreNP and PostNP. In PreNP: (A) Fe(III) chelates surfactant citrate on AuNPs, (B) DA diffuse to these sites and chelate to Fe(III), (C) Fe(III)DA complex migrates to hotspots. In PostNP: Fe(III)DA, Fe(III)DA2 and Fe(III)DA3 formed in solution diffuse to citrates and migrate to the hotspots. (D) Single DA can potentially chelate with two Fe(III) only in the gap regions.

These above characterisations of DA SERS sensing efficacy for PreNP and PostNP protocols, and the complexation of DA and Fe(III), allow for a detailed discussion of the mechanisms by which DA reach the hotspots after they are added to AuNPs aggregate solutions (Figure 2.23).

Figure 2.23 shows schematics for the two protocols. For protocol PreNP, Fe(III) coated AuNPs are aggregated by NaCl firstly, and free dopamine molecules diffuse close to or into the hotspots from bulk solution by binding to Fe(III). In the PreNP scenario, pre-incubation allows each Fe(III) to bind to citrate on the AuNPs (the surfactant used in typical synthetic routes for AuNPs). This allows DA molecules to attach to the AuNPs surface through binding to the citrate-complexed Fe(III) on the AuNPs. It then appears that these complexes migrate across the surface into the hotspots to give a LOD of < 1 nM DA in water. This hypothesis is favoured by recent work using a similar platform where AuNPs aggregation is achieved through cucurbituril[5] (CB[5]) complexation[81]. In that system, ethanol and methanol migrate to the more hydrophobic hotspots between AuNPs bridged by CB[5]. It is also possible that hydroxyls can link two Fe(III) in the hotspot (Figure 2.23a, process D), although Fe(III) only covers AuNPs very sparsely.

By contrast in the PostNP scenario, citrate-coated AuNPs are aggregated by NaCl firstly, and Dopamine-Fe(III) complexes diffuse to the Au surface and bind to citrate by Fe(III). Complexes of Fe(III) and DA form in advance of addition to the aggregate solution. These presumably bind to the AuNPs surface and thence into the hotspots by a similar mechanism as in PreNP. The high fraction of Fe(III)DA2 in PostNP which is buffered to pH 6.3, contrasts with PreNP where individual DA diffuse onto the aggregates. The latter has a nearly hundred-fold lower LOD, but gives only 50% of the SERS strength of the former. These likely result from the complex binding, multiple chelation, and surface migration mechanisms involved.

2.6.5 Summary

In this section, DA SERS was systematically analysed by AuNPs-Citrate-Fe(III)-DA structured substrate. We compared two distinct protocols ('PreNP' and 'PostNP') which differ in the order of steps for forming SERS sensing complexes, affecting both the LOD and the DA SERS intensities. Characterising complexation of Fe(III) and dopamine (DA) in different pH suggests that Fe(III)DA2 dominates in PostNP detection, whilst in PreNP it is the monomeric Fe(III)DA that is seen. When the pH in solution is extremely acidic (basic), protonation (deprotonation) of the hydroxyl bonds of DA becomes competitive to their binding to Fe(III), leading to a decrease (increase) in SERS. Full optimisation is thus crucial for DA SERS sensing, which improves the ability of DA to bind to the surface of AuNPs and migrate to the vicinity of the hotspots. The dopamine limits of detection were 0.01 to 0.1 μM by

dopamine-Fe(III)-AuNPs complex SERS, which enables to perform fast detection of multiplexed neurotransmitters (NTs) at physiological concentrations.

2.7 Overall summary

In this chapter, the Raman spectra of dopamine at different pH environments is discussed. Density functional theory (DFT) calculations was carried out to help understand the dopamine molecules' resonance modes. Dopamine concentration series for Raman spectra were carried out to determine the detection of limit of dopamine in pure water which is in the range of 100 mM to 250 mM. In order to decrease detecting limit of dopamine, the Raman signal was enhanced by surface enhance Raman spectroscopy. Gold nanoparticles were introduced as the main SERS substrates for dopamine detection. The AuNPs assembly process, dopamine-AuNPs binding methods by either CB[n] molecules or Fe(III) ions and weak binding directly by dopamine molecule its self was discussed.

Time-resolved extinction spectroscopy was used to track the AuNPs aggregates formation process. CB[n]-induced and NaCl-induced AuNPs aggregation processes both show three extinction spectra features ('monomer' mode, 'dimer' mode and 'aggregate' mode) which indicate that the plasmonic modes of complex aggregates are governed by these three chain subunits. Dopamine LOD was 1 µM for NaCl-induced AuNPs aggregates SERS, and was 0.1 to 1 µM for CB[n]-induced AuNPs aggregations SERS, which reaches the level of physiological dopamine concentration in urine.

Iron ion(III) was also introduced as a binding agent for dopamine and AuNPs. The protocols, the binding mechanism, and the sensing results were discussed. Protocol PreNP and PostNP were applied in this system. Compared to SERS spectra from NaCl-induced aggregates, protocol PreNP gives 10 times higher signal intensity and protocol PostNP gives 20 times higher signal intensity. The LOD is 1 nM for protocol PreNP and 10 nM for protocol PostNP.

Dopamine-Fe(III) complexes modes are highly dependent on environment pH. When pH is low, monomer mode Fe(III)DA dominates the system, and the Raman intensity is relatively low since mono binding mode shows relatively weak electromagnetic resonance. When pH rises to neutral, dimer mode Fe(III)DA2 becomes the dominant species and when pH is high, the dominant species is the trimer mode Fe(III)DA3. The signals increase as pH increases since dimer and trimer modes' electron clouds are more delocalised so have stronger electronic resonance and give out stronger Raman signals. PH influence on Dopamine-Fe(III) complex SERS was also tested. With PreNP protocol, when pH rises from acidic to neutral, SERS signal increases dramatically due to the change from monomer mode to dimer mode, which shows more electronic resonance ability than monomer mode. However, it is a challenge to imply SERS for higher pH environment since the instability of dopamine in basic

environment and the SERS signals are easily covered by photo luminescence from polymerized or oxidised dopamine.

Chapter 3 Other Neurotransmitters Raman/SERS Sensing

Apart from dopamine, there are more than 40 of other NTs discovered in human body.[142] Among all these NTs, catecholamine is of the most important members due to their roles as neuromodulators in the central nervous system and as hormones in the blood circulation.[143,144] The molecule of a catecholamine consists of a catechol and a side chain amine. Typically, dopamine (DA), Norepinephrine (NEPI), DOPA and epinephrine (EPI) are most widely discussed catecholamine (molecular structure see Figure 3.1).

As stated in Chapter 2, Fe(III) can bind to catechol via two OH groups (binding affinity logK = 43.8[136]) on benzene, and this helps ultratrace DA SERS sensing with AuNPs-Citrate-Fe(III)-DA complex substrate. Therefore, other catecholamine NTs are likely to be detected by the same protocol to ultratrace concentrations. In this chapter, the ultratrace sensing of other catecholamine NTs will be ultimately discussed, before which, the distinguishment of these NTs will be studied by their finger printing Raman signatures. For comparison, non-catecholamine NT serotonin (Sero in Figure 3.1) which shows weaker binding affinity to Fe(III) (logK = 7[136]), will also be included and discussed.
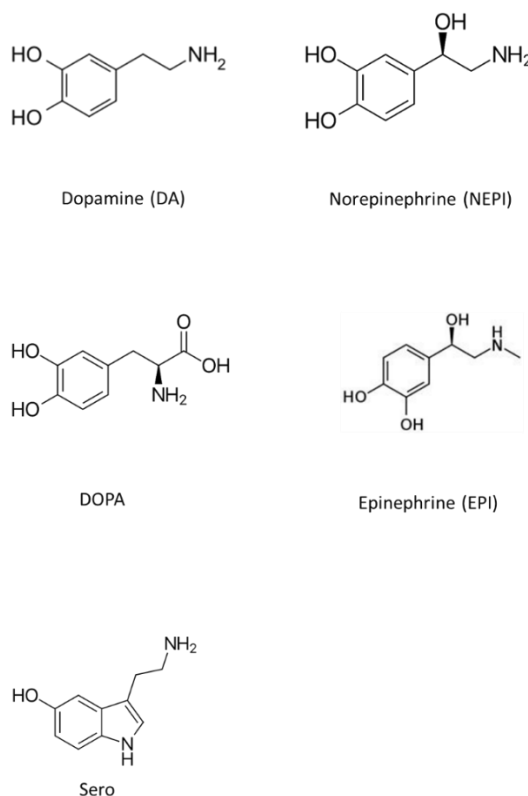
Figure 3.1 Neurotransmitters examined

3.1 Raman spectroscopy of other NTs

3.1.1 Raman of pure NT in solvents
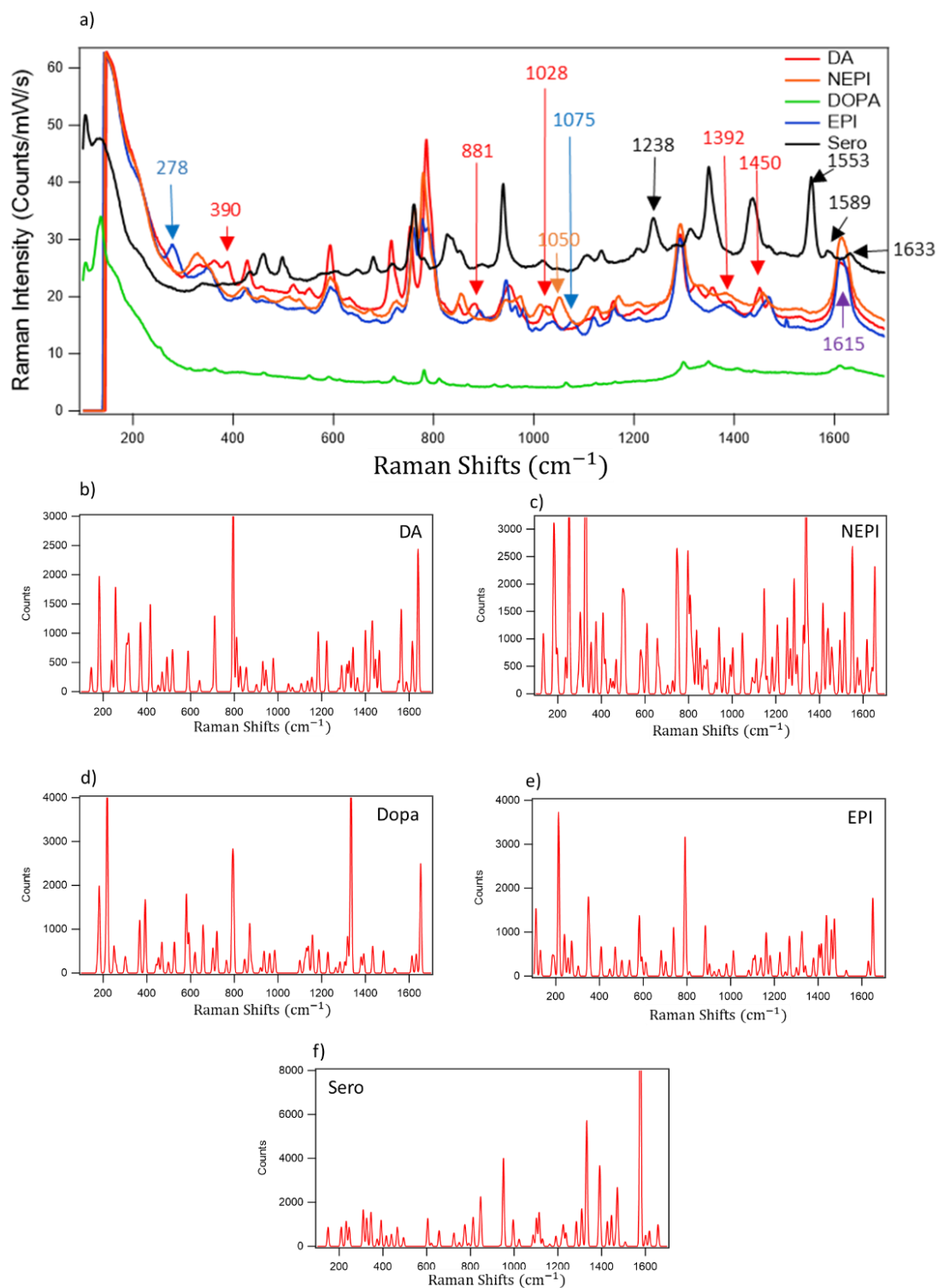
Figure 3.2a) Raman of NTs in water; b-f) NTs DFT Raman spectra for DA, NEPI, Dopa, EPI, Sero respectively. DFT calculations were carried out with dried samples.

Like dopamine the Raman spectra of other catechol neurotransmitters was firstly examined, as shown in Figure 3.2a. The figure shows Raman spectra of all the five NTs in water solution. DA, NEPI, EPI and Sero are at a concentration of 1 M, and DOPA is at concentration of 0.1 M due to its poor solubility in water. Because of this, the Raman intensity of DOPA is much weaker than the other four NTs even though it is saturated. From Figure 3.2a, it can be seen that the spectra of Sero stands out from others due to its distinguishable structure and its unique Raman peaks which are marked by black arrows. For DA, NEPI and EPI, they show similar Raman spectra with subtle differences between each other, as marked by arrows in red, orange and blue in Figure 3.2a. The assignments of these peaks to chemical bonds interactions are shown in Table 3.1, correlated by the DFT calculation of NT single molecule Raman spectra as shown in Figure 3.2b-f. These NTs (apart from DOPA) all have their unique Raman peaks that can allow them to be distinguishable from each other at a concentration of 1 M, although due to the poor solubility of DOPA the spectra is not good enough to distinguish the peaks.

Raman Shifts (cm^{-1})	Assignments
278	EPI C-N-C bending
390	DA C-C-N
881	DA C-C-N
1028	DA C-C-N
1050	NEPI C-N-H
1075	EPI N-C-H
1238	Sero two-ring
1392	DA C-C-N
1455	DA Benzene
1553, 1589	Sero two-ring vibration
1615	DA EPI NE DOPA H-N-H Bending
1633	Sero H-N-H Bending

Table 3.1 Assignments of NTs unique Raman peaks to chemical bonds vibration modes based on DFT calculations.

Using the same protocol as DA, the NEPI and Sero concentration series for Raman detection was carried out to determine the LOD, as shown in Figure 3.3. In Figure 3.3 a and d, NT Raman intensities increase as concentration increases from 0 mM to 1000 mM. The Raman spectra in the fingerprint region only show peaks with samples of concentration above 100 mM, indicating that the LOD is above 100 mM in pure water solution for both NEPI and Sero. Figure 3.3 b and e show the PCA analysis result PC0 and PC1, where PC0 spectra can match the Raman spectra of sample without analyte and PC1 can be correlated to the major variation NT spectra. In Figure 3.3 c and f., the PC1 scores increase dramatically when the NTs concentration is above 100 mM for both cases, so the LOD for Raman is around 100 mM for NEPI and Sero in water. Again, this value is 5 to 7 orders of magnitude above the level in body fluids which is normally between 0.01 to 1 μM. Therefore, SERS should also be introduced to enhance the LOD for these other NTs.
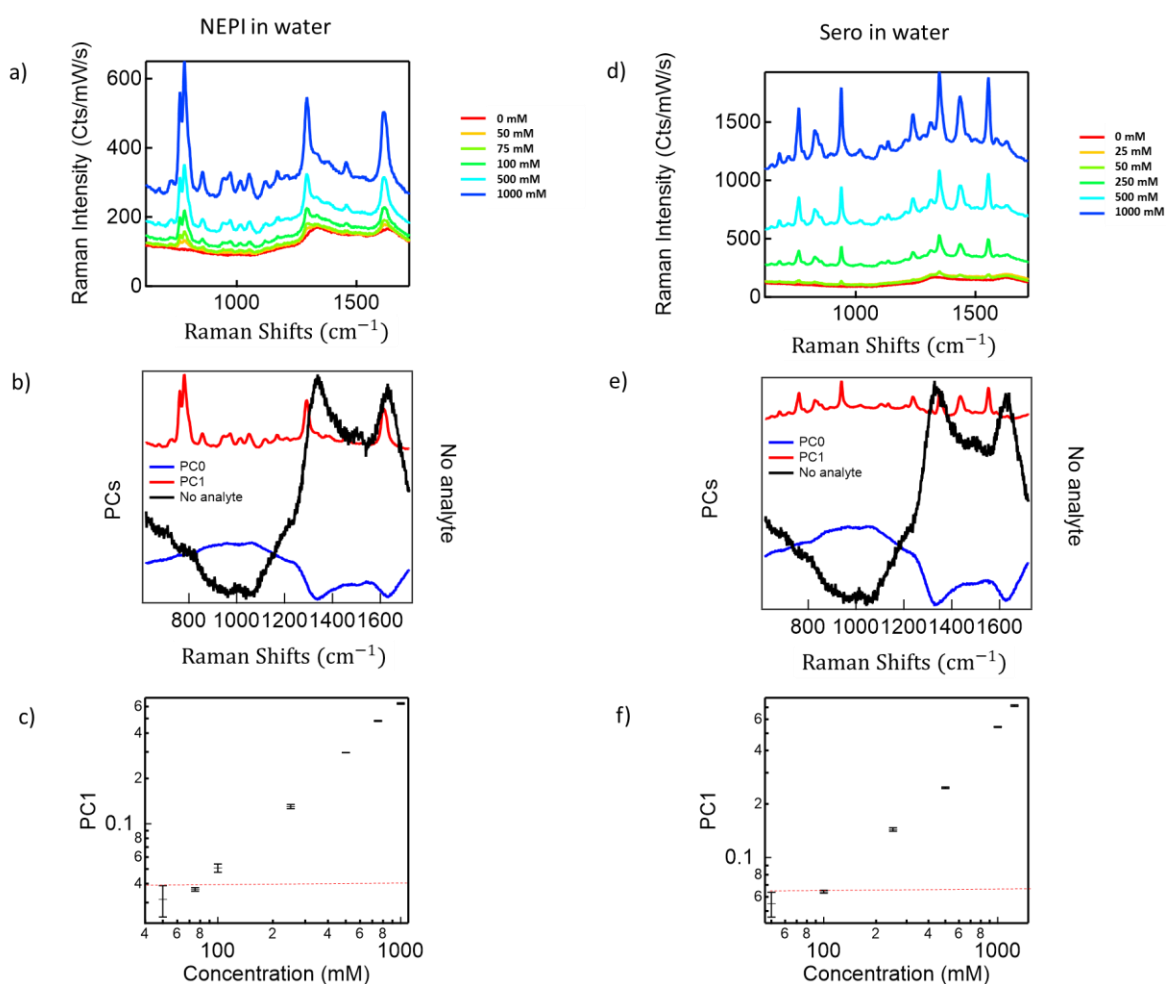
Figure 3.3 a) NEPI d) Sero Raman concentration series in pure water. b,e) Raman spectra of PC0, PC1 after PCA analysis, and sample without analyte for NEPI and Sero respectively. c,f) PC1 scores vs NEPI and Sero concentrations respectively with noise level dashed.

3.1.2 Raman of a mixture of 2 NTs solutions

Knowing that every NT shows some unique Raman peaks in their single NT solution, it becomes appealing to discover whether they show the same unique Raman peaks in mixture solvents. The Raman measurements for mixtures of 2 NTs were carried out and the comparison to that of single NT Raman spectra, Figure 3.4. The unique Raman peaks for each NT are marked in different colours and the purple coloured spectra in each figure represents the mixture's Raman. By comparing the 3 spectra in each figure, we can find that the mixture shows the same unique Raman peaks as the single NT solution, even though the intensity is weaker due to diluted concentration of each component. From Figure 3.4 b), e), h) and j), we can see that when DA, NEPI, EPI or Sero mixed with DOPA, the mixture shows exactly the same peaks as DA, NEPI, EPI or Sero with lower intensity due to very weak impact from low concentration of DOPA.
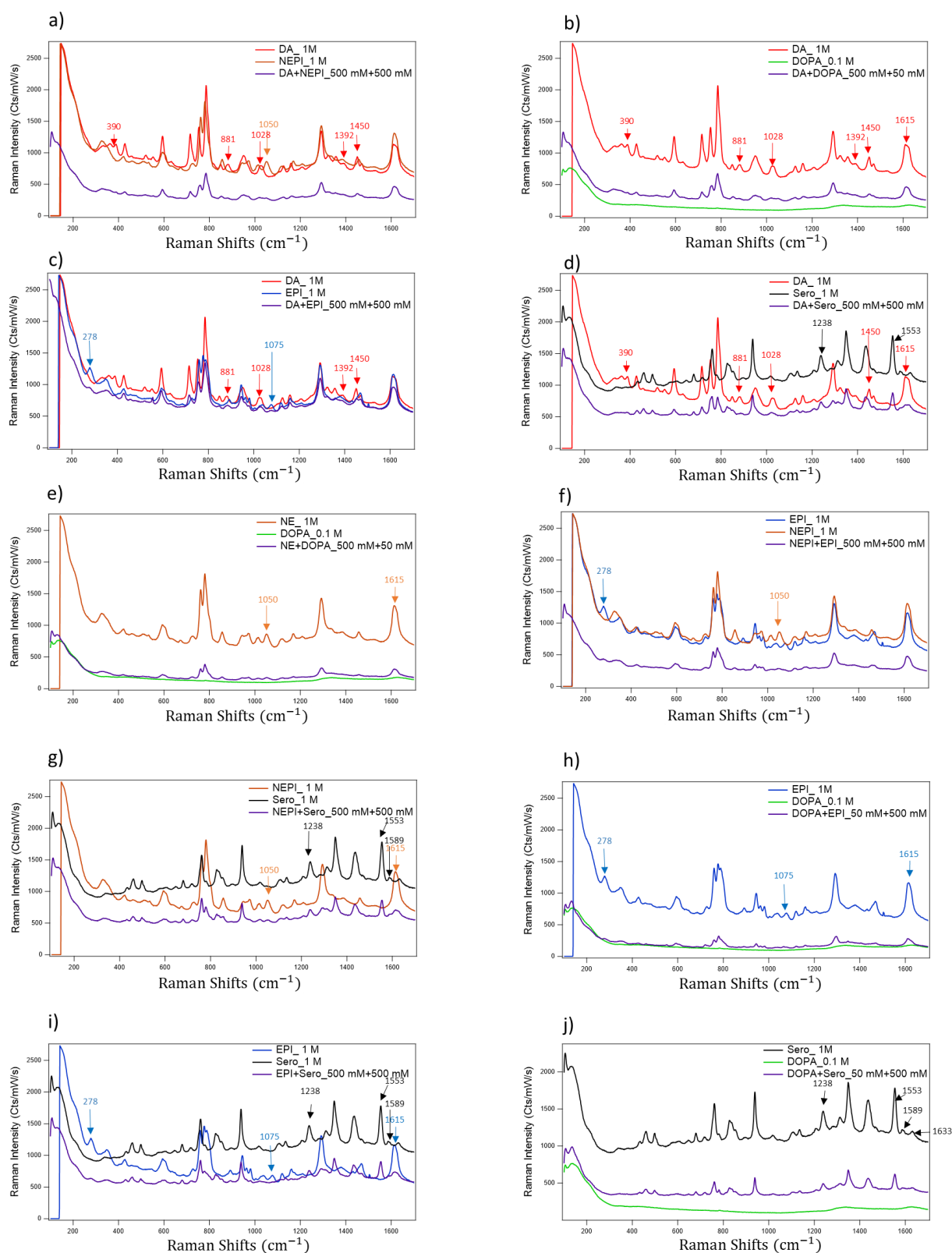
Figure 3.4 Raman spectra of every 2 NTs mixtures compared to that of single NT.

It was shown that when DA, NEPI, or EPI mixed with Sero, the mixture's spectra show unique peaks from both components and all these peaks are easy to distinguish due to Sero's distinguishable molecular structure from other three, Figure 3.4 d, g and i. When it comes to the mixture of every 2 of DA, NEPI and EPI, it is not that straight forward to tell the mixture's peaks from single component's due to similar molecular structures of the three, Figure 3.4 a), c) and f). However, weak peaks show up in mixture's spectra which can correlate to that of pure DA, NEPI or EPI spectra, which indicates that in mixture solution, Raman can still help to distinguish these NTs even though they have similar molecular structures.

3.1.3 DFT experiments for the study of a mixture of catechol NT DA and non-catechol NT Sero

To further evaluate the catechol NT sensing behaviour in the presence of non-catechol NT, a mixture of DA and Sero were examined.

It was shown in Figure 3.4d that DA and Sero are distinguishable from each other by Raman spectra when they are mixed in water. DFT calculations were carried out to evaluate the structure of these two molecules in pure water, as shown in Figure 3.5. Two structures were calculated, one structure is formed by neutral DA molecule and neutral Sero molecule, namely DA + Sero, as shown in Figure 3.5 a and b, the other structure is formed by protonated DA and protonated Sero, namely DAH + SeroH, as shown in Figure 3.5 c and d. Both DA and Sero are protonated on amino group of the alkyl chain. In Figure 3.5 b, it is shown that the two molecule DA and Sero tend to stay apart and in Figure 3.5 d, it is shown that the pronated DAH amino group forms hydrogen bond with the OH group of SeroH. The assignments of typical chemical bonds interaction to the calculated peaks are shown in Table 3.2, where hydrogen bonds interactions are marked in red colour. Hydrogen bond interactions can be found with structure DAH + SeroH, at peaks 1598, 1028, and 208 cm^{-1}, but not in DA + Sero structure. By comparing the Raman intensity of two structures, the DAH + SeroH structure shows twice the intensity of DA + Sero. This is because the hydrogen bond enhances the molecule's polarizability, and the electron cloud of the whole molecule becomes more easily deformed so has enhanced intensity compared to single molecules. Therefore, the peaks of hydrogen bonded structure generally shows higher Raman intensity than individual molecules.
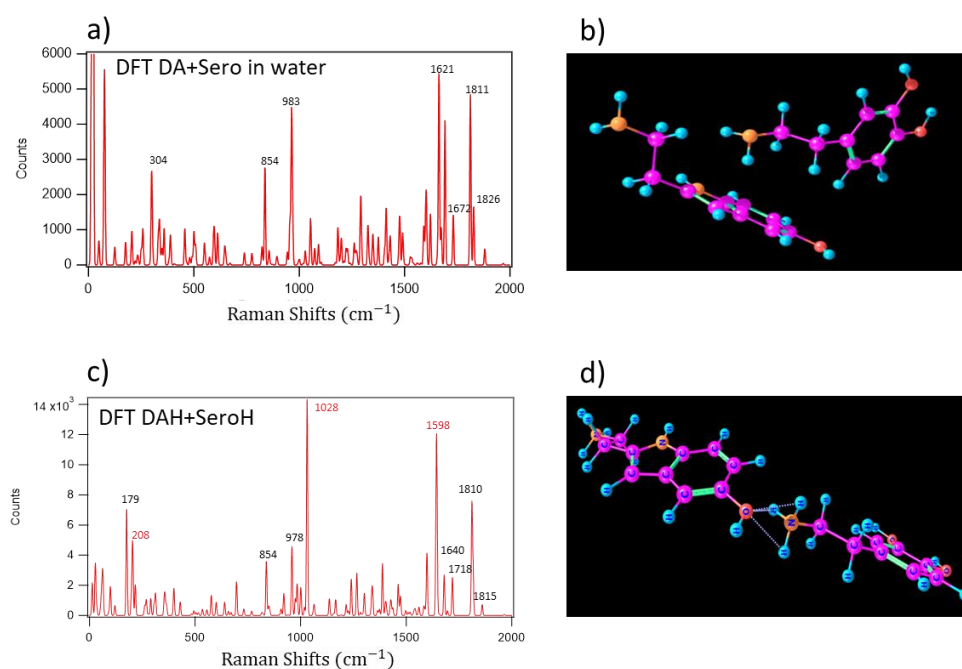
Figure 3.5 DFT calculated Raman spectra of structure a) DA + Sero; c) DAH + SeroH; Complex structure of b) DA + Sero; d) DAH + SeroH. DFT calculations were carried out with dried samples.

	DFT DA+Sero in water	DFT DAH+SeroH in water
(DA) N-H...O (Sero)	None	1598
(Sero) N-H	1672	1640
(Sero) Indol	1621	1718
(Sero) Indol	1811	1810
(DA) Benzene	1826	1815
(DA)N-H...O-H (Sero)	None	1028, 208
C-H	983	978
(DA) Benzene	854	854
Whole complex vibration	304	179

Table 3.2 Assignments of Raman peaks to chemical bonds interactions for two complex structures.

To evaluate the dominant structure in the real-world system, a comparison of the experimental Raman data with DFT calculation results of both structures was carried out, as shown in Figure 3.6. The structure DAH + SeroH shows more correlated peaks to experimental data than that of DA + Sero, which indicates that there is more hydrogen bonded structure than individual molecules in water. Besides, as red marked in Figure 3.6 b, hydrogen bonds peaks 1598 and 1028 cm^{-1} can be correlated to experimental data, with peak 1598 cm^{-1} red shifted to 1615 cm^{-1}, so DAH + SeroH can be one of the contributions to peak 1615 and 1028 cm^{-1} of the mixture. However, there can be many other structures in the real-world system, for example, complex formed by multiple DAH linked by hydrogen

bonds, complex formed by multiple SeroH linked by hydrogen bonds or complex formed by more than 1 DAH and SeroH molecule. All these complexes exist simultaneously and contribute to the Raman spectra measured in real-world system.
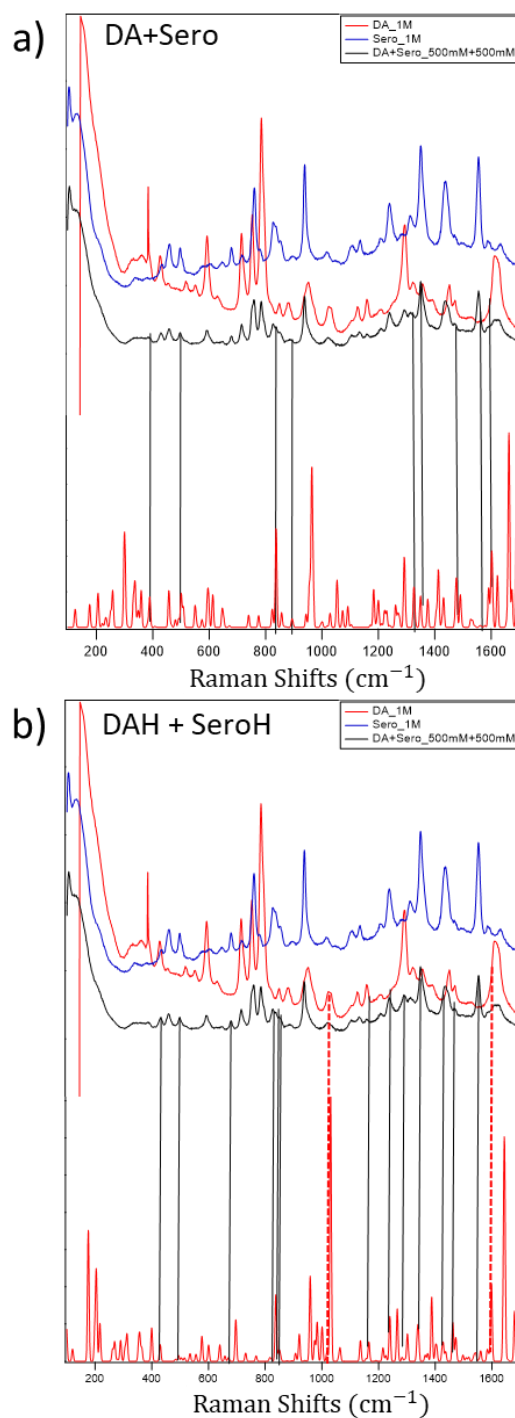
Figure 3.6 Mixture DA and Sero Raman experimental data correlated to DFT calculation of structure a) DA + Sero; and b) DAH + SeroH.

3.1.4 Raman sensing of catechol NTs (DA, NEPI) in non-catechol NT (Sero) solution with and without Fe(III)
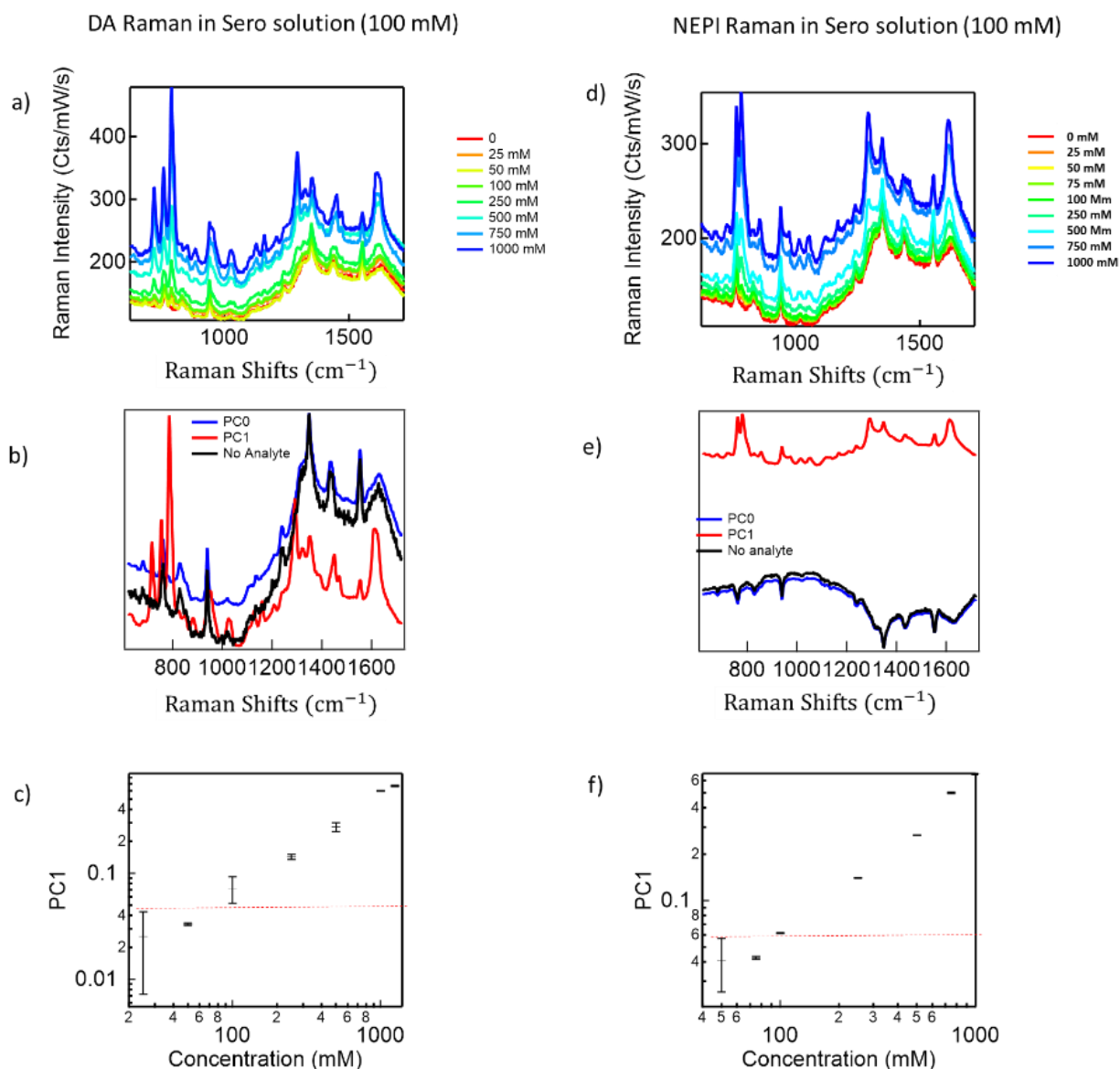
Figure 3.7 a) DA d) NEPI Raman concentration series in 100 mM Sero solvents. b, e) Raman spectra of PC0, PC1 after PCA analysis, and sample without analyte of DA and NEPI respectively. c, f) PC1 scores vs DA and NEPI concentrations respectively, with noise level dashed.

With the existence of NT Sero (100 mM), a Raman concentration series of DA and NEPI were were collected to determine the LOD. In Figure 3.7 a and d, similar as single analyte sensing, DA/NEPI Raman intensities increase as concentration increases from 0 mM to 1000 mM and the fingerprint DA/NEPI Raman peaks are only shown when concentration is above 100 mM, which indicates that the LOD is above 100 mM in 100 mM Sero solution for both DA and NEPI. Figure 3.7 b and e show PCA analysis result PC0 and PC1, where PC0 spectra matches the Raman spectra of pure Sero (black spectra) and PC1 can be correlated to the major variation DA/NEPI spectra. In Figure 3.7 c and f, it shows the PC1

scores increase as DA/NEPI concentration increases and we can find the LOD is about 100 mM for both cases. Comparing with Figure 2.7 where the LOD for DA in water is 100 mM, and Figure 3.3 where the LOD for NEPI in water is 100 mM, the existence of non-catechol NT Sero does not influence the Raman detection of catechol NTs in water.
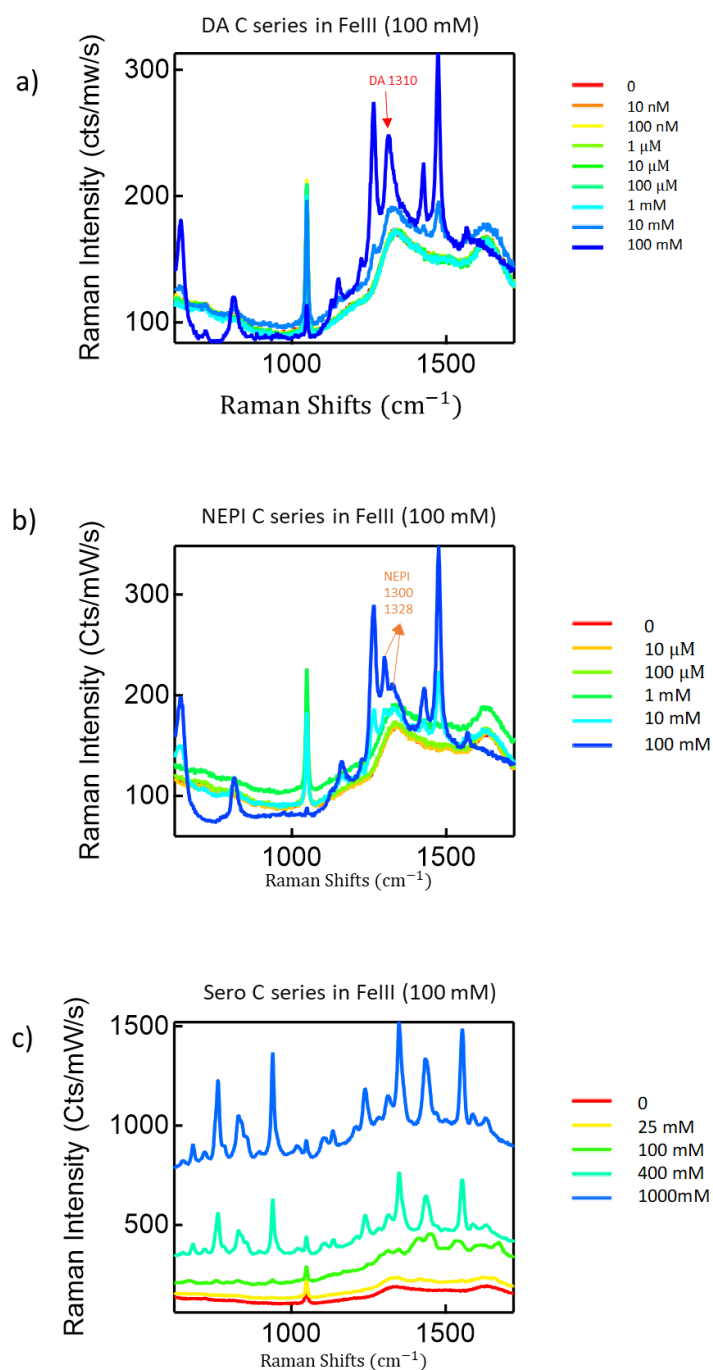
Figure 3.8 Raman concentration series of a) DA; b) NEPI; and c) Sero solvent in the existence of Fe(III) (100 mM)

Since AuNPs-Fe(III)-NTs complexes can be used for NT Raman enhancement, to first understand the Raman detection of Fe(III)-NT complex is important. Figure 3.8 shows Raman concentration series of DA, NEPI and Sero in the presence of Fe(III) (100 mM). From Figure 3.8 a&b, peaks of DA and NEPI can be seen when the concentration is above 10 mM. Compared to the LOD in Figure 2.7 for DA in pure water, and for NEPI in pure water, which are both 100 mM, the LOD is 10 mM when there is Fe(III) ion in solution (Figure 3.3). Therefore, Fe(III) ion can help enhance catechol NTs Raman signals. This is due to the formation of complex Fe(III)-NT as mono binding mode in acidic environment and dimer mode in neutral environment, as illustrated in Figure 2.4. The complexes enhance the polarizability of NT molecule. The electron cloud of molecules becomes more easily to deform so has enhanced electronic magnetic vibration intensity compared to single molecules. To distinguish Fe(III)-DA from Fe(III)-NEPI, the peak differences are marked in Figure 3.8 a and b, where DA shows a singlet peak at 1310 cm^{-1} while NEPI shows a doublet peaks at 1300 cm^{-1} and 1328 cm^{-1} at high concentration. For the case of non-catechol NT Sero, the Raman peaks only show up when the concentration is above 100 mM, so the LOD of Sero is about 100 mM with the existence of Fe(III). Comparing to Figure 3.3 where the Sero Raman LOD is 100 mM in pure water, the LOD with Fe(III) has not been improved. This is because Sero only has one OH group in benzene and the binding affinity to Fe(III) is not as strong as the catechol does (Fe(III)-Sero log K = 7, Fe(III)-Catechol log K = 43.8). Not as strong complexes can be formed to enhance the Sero Raman signals so the Raman signal intensities are at the similar level with and without Fe(III).

Further, DA Raman concentration series were carried out in the presence of both Serotonin and Fe(III), as shown in Figure 3.9 a-c, where 10 mM, 50 mM and 100 mM Sero were tested respectively for DA concentration series sensing with 100 mM Fe(III). When Sero concentration is low at 10 mM, DA can reach the LOD around 10 mM, as same as Figure 3.8 a, where there is no Sero involved. Therefore, low concentration of Sero does not influence the detection of DA in Fe(III) solvent. However, when Sero's concentration goes up to 50 mM and 100 mM, as shown in Figure 3.9 b and c, the Raman signal of Sero dominates the spectra with tiny DA peaks spikes at high concentrations. This indicates that even though the Fe(III) binding affinity to Sero is much weaker than that of DA, large amount can still have a huge influence on the sensing of DA. When a high concentration of Sero is premixed with Fe(III), the binding complex formed and the additional DA need to overcome the energy barrier to bind with Fe(III). The result indicates that the energy barrier is a bit higher that DA can not compete with pre-bound Sero. The same result applies to NEPI as shown in Figure 3.9 d, where when 100 mM Sero pre mix with Fe(III), little NEPI can be detected.
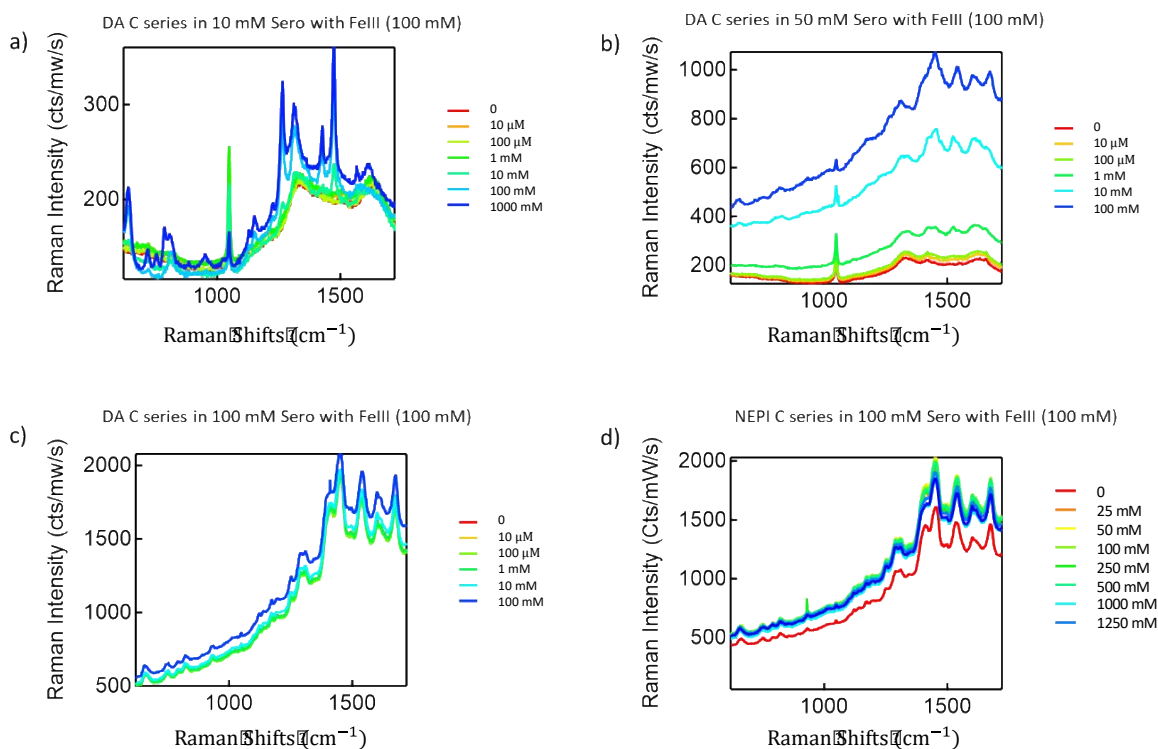
Figure 3.9 DA Raman concentration series with 100 mM Fe(III) in Sero solvent of a) 10 mM; b) 50 mM and c) 100 mM respectively. d) NEPI Raman concentration series with 100 mM Fe(III) in Sero solvent of 100 mM.

3.1.5 Raman sensing of catechol NT (DA) in catechol NT (NEPI) solution with and without Fe(III)

DA and NEPI both have a catechol structure and show similar Raman spectra both with and without Fe(III), as shown in Figure 3.4a and 2.30 a&b. It is crucial to determine the detection limit of one in the presence of the other one. DA concentration series were carried out in 500 mM NEPI solvent with and without Fe(III), as shown in Figure 3.10. PCA was applied for data analysis because it is difficult to tell the subtle change in spectr, as shown in Figure 3.10 a&d at low DA concentrations.

In Figure 3.10a, when Fe(III) is not involved, the DA peak at 1028 cm^{-1} appears at high concentration and NEPI peak at 1050 cm^{-1} shows in nearly all spectra apart from 1000 mM DA concentration where the broad DA 1028 cm^{-1} peak covers 1050 cm^{-1} position. This result can be correlated to Figure 3.4 a. After PCA analysis, PC0 matches with NEPI Raman spectra very well and the 1050 cm^{-1} NEPI peak is marked in orange in Figure 3.10 b. PC1 can be correlated to DA spectra where its 1028 cm^{-1} peak is marked in red. The PC1 scores change along DA concentration as shown in Figure 3.10 c and the DA LOD can be determined at around 100 mM, which is consistent with the result of single DA solution as shown in Figure 2.7a. This indicates that the existence of NEPI has little influence on DA Raman detection.

When Fe(III) is involved, the DA singlet peak at 1310 cm^{-1} appears at high concentration and NEPI doublet peaks at 1300 cm^{-1} and 1328 cm^{-1} are found in nearly all spectra apart from 1000 mM DA concentration where the broad DA singlet 1310 cm^{-1} peak covers the NEPI doublet peaks, as shown in Figure 3.10d. This result can be correlated to Figure 3.6 a&b. After PCA analysis, PC0 matches with Fe(III)-NEPI complex sample and the doublet NEPI peaks are marked in orange in Figure 3.10 e. PC1 can be correlated to Fe(III)-DA complex spectra where its 1310 cm^{-1} singlet peak is marked in red. The PC1 scores change along DA concentration as shown in Figure 3.10 f and the DA LOD can be determined at around 10 mM, which is consistent with the result of single Fe(III)-DA solution as shown in Figure 3.8 a. This again indicates that the existence of NEPI has little influence on DA Raman detection in Fe(III) environment.
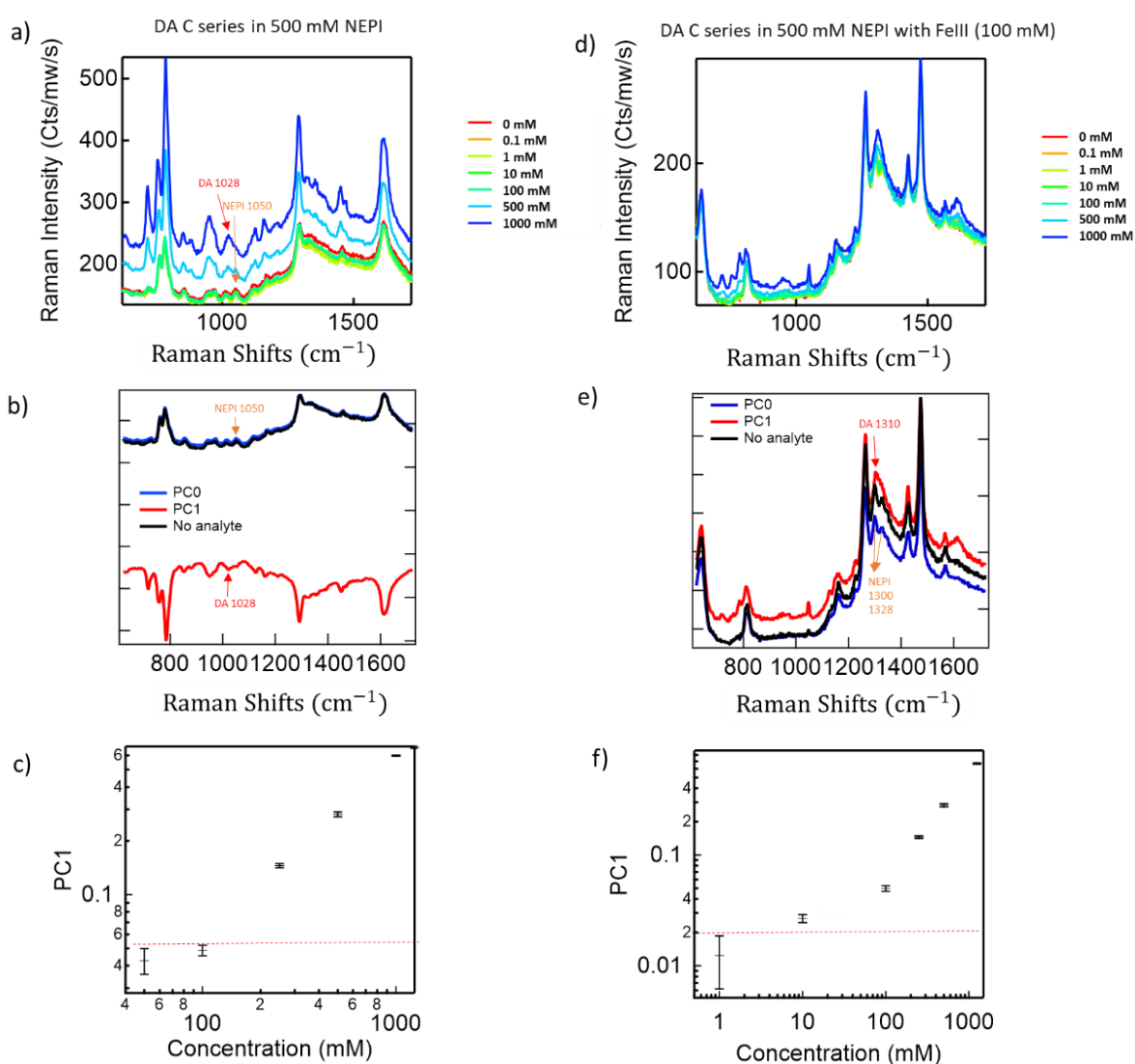
Figure 3.10 DA Raman concentration series in 500 mM NEPI solvents a) without and d) with 100 mM Fe(III). b, e) Raman spectra of PC0, PC1 after PCA analysis, and sample without analyte DA for the case

71

without and with Fe(III). c, f) PC1 scores vs DA concentrations for the case without and with Fe(III), with noise level dashed.

3.2 SERS sensing of other NTs

The above Raman spectra were all obtained at high concentration because they show very weak Raman signals when the concentration is below 10 mM. In order to detect lower concentration of other NTs, the AuNPs-Fe(III)-NT complex system was introduced to do SERS for all the other NTs, by both protocol PreNP and PostNP.

The SERS spectra show subtle differences between all of these NTs as shown in Figure 3.11a. Considering that the molecular structures of these NTs resemble each other, except for differing functional groups on the other end of the hydroxyl NT terminus, it is clear why their SERS spectra are similar (though distinguishable). Since there is only one hydroxyl bond in SERO, whilst two in the other molecules, it is most likely that the weaker SERS intensity of SERO is due to weaker binding. This again emphasises how bidentate Fe(III) chelation is vital to this assay.

The low LOD for PreNP protocol suggests that unassisted solution diffusion of soluble NTs to the hotspots followed by chelation to localised Fe(III) in the hot spot provides an efficient assay. To compare these assays, PCA scores for DA, DOPA, NEPI and EPI were obtained from PreNP protocol vs NT concentration (Figure 3.11b). The concentration series from 1 pM to 1M were tested for all the NTs. Despite their chemical similarity, both signal strengths and LODs (Figure 3.11c) are significantly different. For NTs with two hydroxyls, LODs of DA, EPI and NEPI are much lower than DOPA; while DA has the highest signal strength, DOPA is the lowest of this set. This implies that whether or not the functional groups in a NT have net charge influences their ability to diffuse onto the surface of AuNPs in PreNP protocol and subsequent migration to the hotspots. The reason that DOPA has the worst LOD and signal strength among NTs with two hydroxyls probably results from the additional negative charge of the carboxylate (which the other NTs do not have), that is repelled from the negative surface charge of the citrate-coated AuNPs.
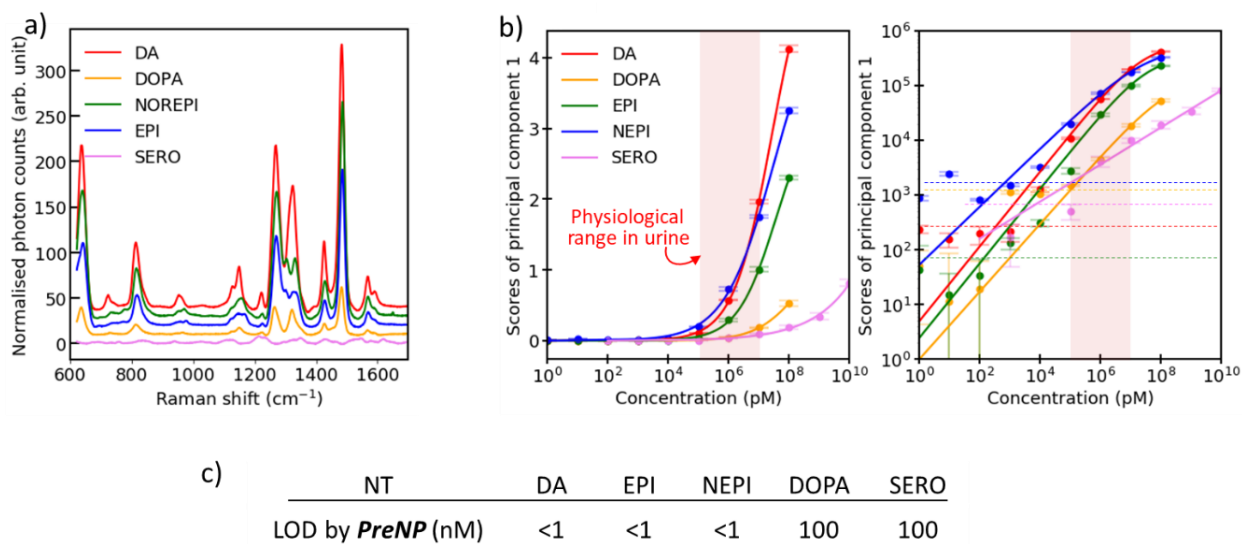
Figure 3.11 a) Normalised SERS of NTs, where NEPI, EPI, DOPA and SERO are norepinephrine, epinephrine, L-DOPA and serotonin, respectively. b) PC1 for NTs in using PreNP on linear and log plots. Noise levels are dashed. Shared red region gives physiological concentrations of NTs in urine. c) Table giving limits of detection (LODs) of NTs using PreNP.

3.3 summary

In this chapter, using the same protocol as in Chapter 2, other neurotransmitters including norepinephrine (NEPI), DOPA, epinephrine (EPI) and serotonin (SERO) were tested by SERS using the same complexes scheme of AuNPs-Citrate-Fe(III)-NTs. DA, EPI and NEPI all reach LOD at 1 nM, which is below the range of physiological concentration. DOPA and SERO show lower detecting sensitivity and the LOD is around 100 nM.

Chapter 4 Liquid-liquid Interfacial Substrates for SERS Sensing

4.1 Background and motivation

In Chapter 2&3, SERS sensing was obtained by Au nanoparticles aggregates suspended in aqueous solution and analytes dissolved in water detected by SERS when they are located in plasmonic hotspots. Even though this method provides high sensing sensitivity, its applications are limited to the detection of aqueous solution samples. When it comes to the analytes sensing in an oil phase, or when analytes both in aqueous and oil phase need to be detected, a substrate which can contact oil phase or both aqueous and oil phase could be a good option. In Chapter 4, a film-shaped AuNPs SERS substrate at water-oil interface will be demonstrated using Au nanoparticles self-assembly at liquid-liquid interface, forming a two-dimensional SERS substrate, which can adsorb and help detect analytes in both liquid phases.

4.1.1 Nanoparticles self-assembly at liquid-liquid interface

Self-assembly refers to the process that nanoparticles or other discrete components spontaneously organize into ordered structures, due to specific interactions or driven by their environment.[87] The assembly of nanoparticles at liquid–liquid interfaces is becoming a central topic both in surface and colloid science, since the soft liquid–liquid interface affords a platform for the assembly and chemical manipulation of nanoparticles, where the nanoparticles are highly mobile and their assemblies can rapidly densely pack. Promisingly, the uniformity of liquid-state interfacial nanoparticle arrays is much superior to the random aggregates in solvents or the fixed arrays on solid surface.[145] On liquid-liquid interfaces, nanoparticle self-assembly could be achieved by either functionalizing nanoparticles or adding electrolyte into the solution containing nanoparticles. The nanoparticle assembly process is driven by either van der Waals or electrostatic forces into mono or multi layers at the interfaces.

The theory of the nanoparticle stability on liquid-liquid interface was fully studied for the past century. Ramsden[146] and Pickering[147] were the first scientists to study the stabilization of emulsions where colloidal particles are adsorbed to the interface of two immiscible liquid phase. This kind of emulsion is called a Pickering Emulsion, which can either be water-in-oil (o/w) or oil-in-water (w/o), depending on the particles wettability.[148] For nanoparticles, one liquid can wet them more than the other liquid, making the less wetting liquid as the dispersed phase. As shown in Figure 4.1a,[149] if the contact angle θ (measured in water phase) is less than 90°, then the particles are hydrophilic and the emulsion tends to be oil-in-water type. If the contact angle θ is more than 90°, then the particles are hydrophobic and the emulsion tends to be water-in-oil type.[150]

Pieranski[151] investigated the thermodynamics of nanoparticles at the water-air interface by analysing a monolayer of spherical particles. The driving force of the particles moving from bulk solution to interface is the reduction of the Helmholtz energy, E. This theory is also applicable to liquid-liquid interfaces. The Helmholtz energy E is determined by

$$E(z) = \pi R^2 \gamma_{O/W} \cdot \left[\left(\frac{z}{R} \right)^2 + 2 \left(\frac{\gamma_{P/O}}{\gamma_{O/W}} - \frac{\gamma_{P/W}}{\gamma_{O/W}} \right) \cdot \frac{z}{R} + 2 \left(\frac{\gamma_{P/O}}{\gamma_{O/W}} + \frac{\gamma_{P/W}}{\gamma_{O/W}} \right) - 1 \right] \tag{1}$$

Where z is the distance of the particle centre from the water/oil interfaces, R is the effective radius of the nanoparticle, $\gamma_{O/W}$, $\gamma_{P/W}$, and $\gamma_{P/O}$ are the interfacial tensions between oil and water, the particle and water, and the particle and oil, respectively. The minimum in E (E_{min}) occurs when

$$z = \frac{\gamma_{P/W} - \gamma_{P/O}}{\gamma_{O/W}} \cdot R \tag{2}$$

Therefore, when the particle moves from the oil phase to the interface, the energy change is

$$\Delta E = E_{min} - E_{\frac{P}{O}} = -\frac{\pi R^2}{\gamma_{O/W}} \left[\gamma_{O/W} - (\gamma_{P/W} - \gamma_{P/O}) \right]^2 \tag{3}$$

where $E_{p/o}$ is the energy when the nanoparticle is located in the oil phase, and locating the particle at the interface leads to a decrease in the energy, which makes the system more stable (Figure 4.1b). Along with Young's equation

$$\gamma_{P/O} - \gamma_{P/W} = \gamma_{O/W} \cos\theta \tag{4}$$

The energy change can also be expressed as

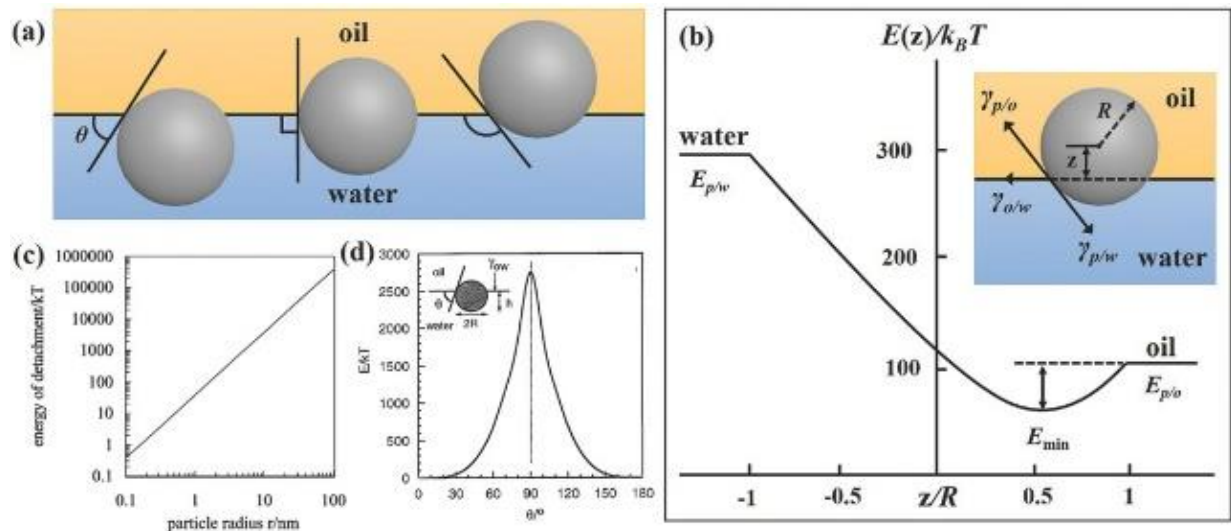$$\Delta E = -\pi R^2 \gamma_{O/W} (1 + \cos\theta)^2 \tag{5}$$

Figure 4.1 a) Position of a small spherical particle at a planar water/oil interface for a contact angle measured through the aqueous phase less than 90° (left), equal to 90° (centre), and greater than 90° (right). b) Estimate of surface energy well. c) Variation of the energy required to detach a single spherical particle exhibiting a contact angle of 90° from a planar water/oil interface (of interfacial tension 50 mN m^{-1}) with particle radius at 298 K. d) Variation of the desorption energy of a spherical particle at a planar water/oil interface as a function of the contact angle; the particle radius is R = 10 nm and the interfacial tension is 36 mN m^{-1}.[149]

From Equations 3 and 5, the Helmholtz energy changed is determined by the R of the particle and the wettability of the particle(θ). As for R, since ΔE is proportional to R^2, the energy keeping nanoscale particles at the interface are significantly less than that for micrometre scale particles. Therefore, thermal energy on one hand gives mobility to the nanoparticles, but on the other hand also induce a desorption energy to the nanoparticles from the interface, making the nanoparticle arrays dynamic or 'liquid-like' in nature at the liquid-liquid interface. Binks[152] analysed this for particles of different R in an alkane/water system (θ = 90°, γ_{ow} = 50 mN m^{-1}) where, as shown in Figure 4.1c, particles with R less than 0.5 nm are easily detached from the interface (several $k_B T$ of desorption energy, where k_B is the Boltzmann constant, and T is the absolute temperature).

As for θ, the desorption energy change along with θ for the water/toluene system (γ_{ow} = 36 mN m^{-1}), was analysed for 10 nm radius silica nanoparticles (Figure 4.1d).[153] A maximum desorption energy was observed when θ is 90°. Deviations away from 90° lead to a rapid decrease in desorption energy. For θ between 0° and 20° or between 180° and 160°, the energy is 10 $k_B T$ or less so the nanoparticles are more easily to be removed from the interface into the liquid, indicating the strong effect of particle surface wettability θ on the interfacial stability.

This stability theory was proved by a number of researchers by using different solvents systems and different types of nanoparticles. Russell[154] used CdSe nanoparticles with different sizes, and found that nanoparticles with less than 1.6 nm diameters were not able to stabilize the emulsion while larger nanoparticles did. To keep the Helmholtz energy at minimization level, the larger nanoparticles tend to stay at the liquid interface and smaller particles are forced away from the interface. Wang[155] analysed influence of the nanoparticle wettability by tuning the contact angles of the nanoparticles with different ligands. By making the nanoparticles hydrophilic, they are stabilised in water phase. By changing the capping ligands to hydrophobic, an interfacial entrapment of the nanoparticles was achieved.

4.1.2 Interfacial substrates for SERS

Due to the unique properties of self-assembled nanoparticles film, using interfacial Au/Ag nanoparticles arrays as SERS substrates has been developed into a novel sensing approach.[156] Gia and co-workers[157] generated plasmonic colloidosomes as 3D-SERS platforms by self-assembly of perfluorodecanethiol functionalized Ag nanoparticles at the interface of water and decane. Ultrasensitive SERS detection of multiphase toxin was achieved with this platform. A SERS sensing platform was established by Yang[158] for RNAs with interfacial gold nanoparticle film at water-oil interface. This sensing protocol was an indirect detection by adding RNA molecules to a solution containing carboxyrhodamine (ROX) and DNA strands functionalized by methylene blue (MB). When RNA was added, it interacted with DNA molecules so that methylene blue molecules were released so the SERS signals of free methylene blue molecules increased. At the same time, free ROX molecules bound to DNA molecules so that free ROX SERS signals decreased. The SERS intensity ratio of MB and ROX molecules were monitored to show the quantitative level of RNA added to the mixture. The paper showed a LOD of 1.10 atto molar for miRNA 155, which showed significantly weaker SERS signal by itself. NaCl was used by the Edel's research group[159][160] to increase the ionic strength of the aqueous phase to drive the Au nanoparticles to self-organize at the water-dichloroethane interface. A droplet Au nanoparticle array on a coverslip can be used as a versatile substrate for quantitative SERS sensing of analytes including toxins, narcotics, explosives and other hazardous chemicals. Wei and co-workers[161] reported a calixarene-based surfactant containing several hydrocarbon tails, providing strong repulsive forces, which has been successfully employed for the fabrication of highly ordered, close-packed gold nanoparticle arrays by self-assembly of large-diameter gold nanoparticles (up to 170 nm in diameter) at the air/water interface and using it for airborne molecule sensing. Using L-cysteine modifiers, Liu[162] demonstrated SERS sensing of trinitrotoluene with gold nanoparticle film formed at water and dimethyl carbonate interface. The trinitrotoluene (TNT) molecules were adsorbed onto the gold surface by forming Meisenheimer complexes with L-cysteine modifiers while other molecules of similar structures could not. It provided a highly selective and sensitive sensing protocol of TNT down to 50 fM.

In this chapter, gold nanoparticle 2D arrays are developed with the special 'glue' molecule CB[n] as well as simply by NaCl, and the arrays are analysed as SERS sensing substrates in different forms. This method will provide a versatile protocol for direct SERS sensing of various analytes. The stability of the interfacial arrays will be studied and furthermore, microdroplet interfaces will be used as the gold nanoparticle array template for SERS sensing. This could provide huge potential for its applications in microfluidic SERS sensing.

4.2 Interfacial Substrate Stability and SERS Sensing

4.2.1 Stability influenced by contact angle and AuNPs/cluster size

The gold nanoparticles used in these experiments were purchased from BBI and the gold nanoparticles in the suspension have a negative surface charge due to the adsorption of citrate and gold-chloride anions. The two liquid phases are water mixed with ethanol (50 vol%) and chloroform. The ethanol is added to adjust the gold nanoparticles surface charge density to form stable arrays at liquid-liquid interface. According to research by Vanmaekelbergh,[163] the addition of ethanol to water gradually decreases the surface charge of gold (Figure 4.2a), likely because of competitive adsorption of ethanol molecules,[164] which displace the citrate or gold-chloride anions from the gold surface. About half the original charge density is preserved upon further addition of ethanol (when ethanol is 50 vol% and more), and the gold sol remains stable. When a layer of oil liquid is introduced above this solution, gold nanoparticles quickly adsorb at the water/oil interface. The nanoparticles coverage of the water/oil interface increases gradually with the decrease of the surface charge density on the gold nanoparticles. Figure 4.2b and 4.2c show in situ optical microscope pictures of the nanoparticle layer after addition of 17 and 38 volume % of ethanol, respectively. Upon the addition of 17 % of ethanol, islands of gold nanoparticle form (Figure 4.2b) and they extend and coalesce to a coherent monolayer as the ethanol content increases (Figure 4.2c).
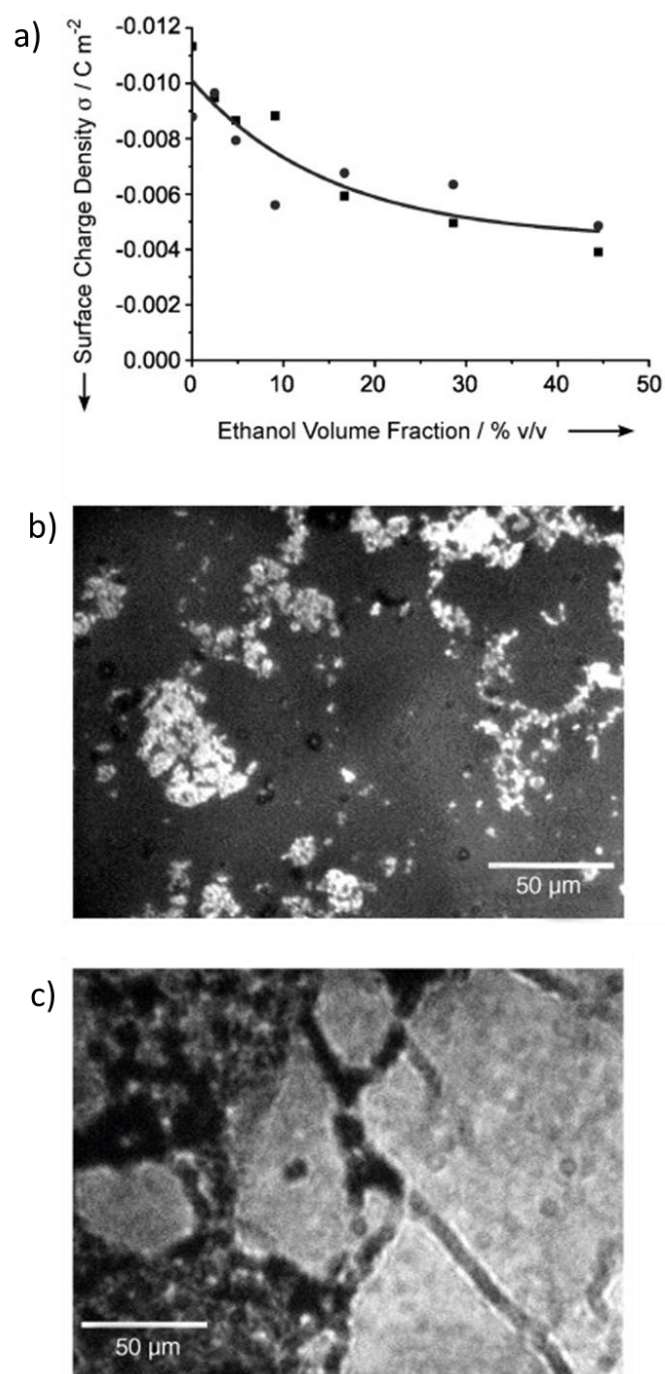
Figure 4.2 Formation of an interfacial monolayer of gold nanoparticles by charge reduction.[163] a) Decrease of the surface-charge density of the gold nanoparticles on adding ethanol to the aqueous sol consisting of Au nanoparticles with a diameter of (■) 4.5 nm and (•) 16 nm, respectively. b) Microscope image of the oil/water interface after addition of 17 vol% ethanol to gold sol: the coverage is low and islands of gold nanoparticles are visible. c) Microscope image of the oil/water interface after addition of 38 vol% of ethanol to gold sol: the gold nanocrystals form large domains that consist of a dense layer of nanocrystals.

A fixed ethanol concentration of 50 vol% was chosen for water/chloroform system. From Equations 5 in Section 4.1.1, when a nanoparticle array is formed at the liquid-liquid interface, the Helmholtz energy changed is influenced by the wettability of the particle(θ) and the particles dimension. Since CB[n] molecules will be introduced for binding analytes on gold nanoparticles surface, the nanoparticle arrays stability with CB[n] is very important before all the SERS sensing is carried out.

The contact angles (θ) of water/CHCl$_3$/Au systems, measured in water phase are shown in Figure 4.3. Au films were immersed in water phase (containing 50 vol% ethanol) and then a tiny drop of pure CHCl$_3$ were carefully injected on the Au film by syringe. Three different Au surface coating formats were analysed: uncoated, CB[7] coated and citrate coated, as shown in Figure 4.3 a, b and c respectively. CB[7] and citrate were coated on Au film surface by dipping the films in 1M CB[7] solution and 1M sodium citrate solution for 24h. The contact angles (θ) were obtained by measuring the angles in microscopic bright image photos (5X).

With the uncoated Au film (Figure 4.3a), the contact angle is significantly more than 90°, which means the Au has much higher affinity to oil than to water. According to Figure 4.1d, Au nanoparticles with no coatings have very low desorption energy from the interface to bulk phase, and they tend to be easy to move into oil phase. For Au film coated with CB[7] (Figure 4.3b), the contact angle is nearly equal to 90°, which means the CB[7] coated Au has as much affinity to oil as to water. Au nanoparticles coated with CB[7] have highest desorption energy from the water/chloroform interface to bulk solution, so they tend to stay at the interface. For Au film coated with citrate (Figure 4.3b), the contact angle is slightly less than but very close to 90°, which means the citrate coated Au (partially replace by ethanol molecules) has slightly larger affinity to water as to oil. In this case, Au nanoparticles have a moderate desorption energy from the water/chloroform interface to bulk solution, so they can form arrays at interface though less stable than CB[7] coated Au nanoparticles. Therefore, both CB[7] and citrate coated gold nanoparticles can form 2D arrays at water/chloroform interface in terms of contact angle and the adding of CB[7] can make the arrays even more stable.
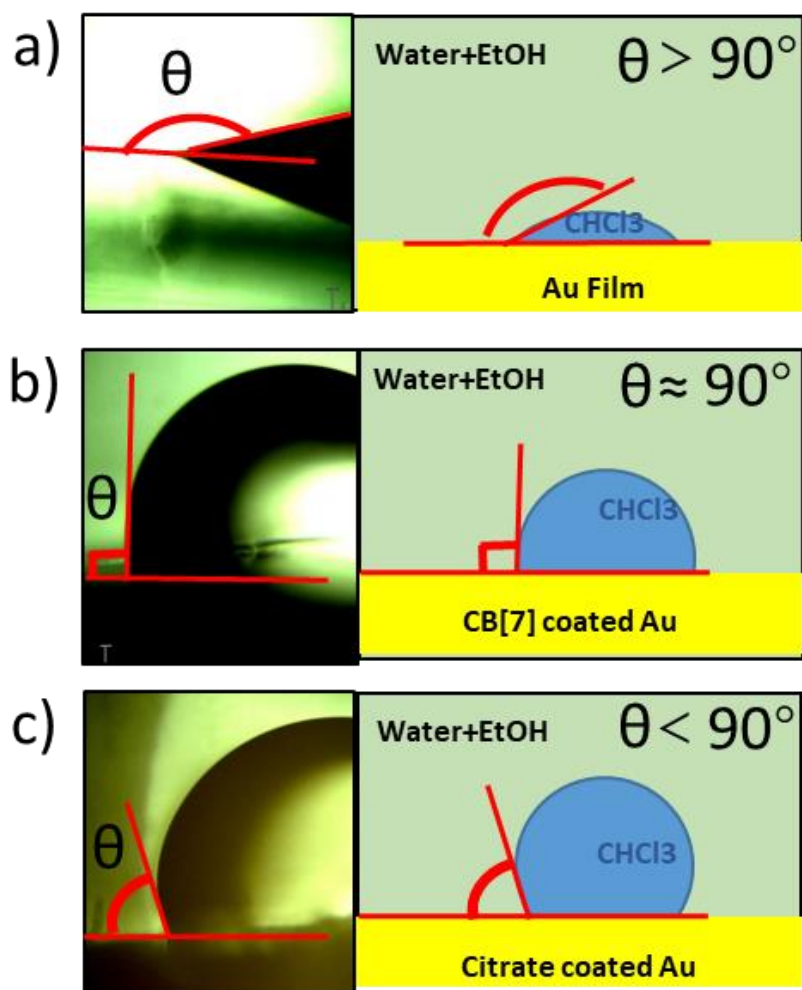
Figure 4.3 Bright field images and schematics of contact angles (θ) of water/CHCl3/Au systems, measured in water phase for different Au coating formats: a) uncoated Au by flame annealing; b) CB[7] coated Au; c) Citrate coated Au, respectively.

The second influential factor is the particle dimension and two different systems were compared: Au nanoparticles (initially coated with citrate) with and without CB[7] added.

For system with CB[7] involved, Au nanoparticles solution were firstly mixed with CB[7] solution in a Teflon tube. Then ethanol and chloroform were added, and after 10 seconds waiting, a black film was formed at the interface and the upper bulk water phase became colourless (Figure 4.4a), which indicates that all of the Au nanoparticles transferred to the interface from the water solution in seconds. After carefully removing most of the chloroform with syringe, the remained drop of chloroform surrounded by AuNPs film at the bottom of water phase was then taken out by a plastic pipet and dropped on a clean smooth gold substrate. After 24h, the Au nanoparticles film was dried out. The SEM images in Figure 4.4 b and c show that the film was formed by Au nanoparticles clusters ranging from nanometer scale (a few single nanoparticles) to sub-micron scale (a large number of

nanoparticles). In this case, a cluster as a whole, is the unit transferring from bulk phase to interface, so the *R* in equation 5 is the size of the cluster which ranges from nanometers to sub-micron.

However, for system without CB[7] involved, ethanol was directly added into Au nanoparticles solution before chloroform. The colour of the water phase remained red after shaking, as shown in Figure 4.4d, although a fine film was observed at the water/oil interface. It took 12h for all the Au nanoparticles to transfer from water phase to interface, making the water phase colourless, indicating that the film forming process without CB[7] is significantly slower and has much less driving force than the process with CB[7] involved. In SEM images of Figure 4.4e and f, the film was formed by single layer of individual Au nanoparticles and shows better uniformity than the large cluster formed film in Figure 4.4b and c. In this case, the *R* in equation 5 is the size of a single nanoparticle 30 nm, which is much less than the clusters size, making the Helmholtz energy change less than the clusters system, so the film formed by single nanoparticles is less stable than the one formed by large clusters.

Overall, CB[7] can help to stabilize the interfacial 2D Au nanoparticles arrays in two ways: one is to change the contact angle (θ) of water/CHCl3/Au systems to 90°, and another is to enlarge the cluster size *R* by making AuNPs into sub-micron scale aggregates. Addition of CB[7] can help to decrease the film formation time from 12h to 10s, making it a much quicker and more convenient process.
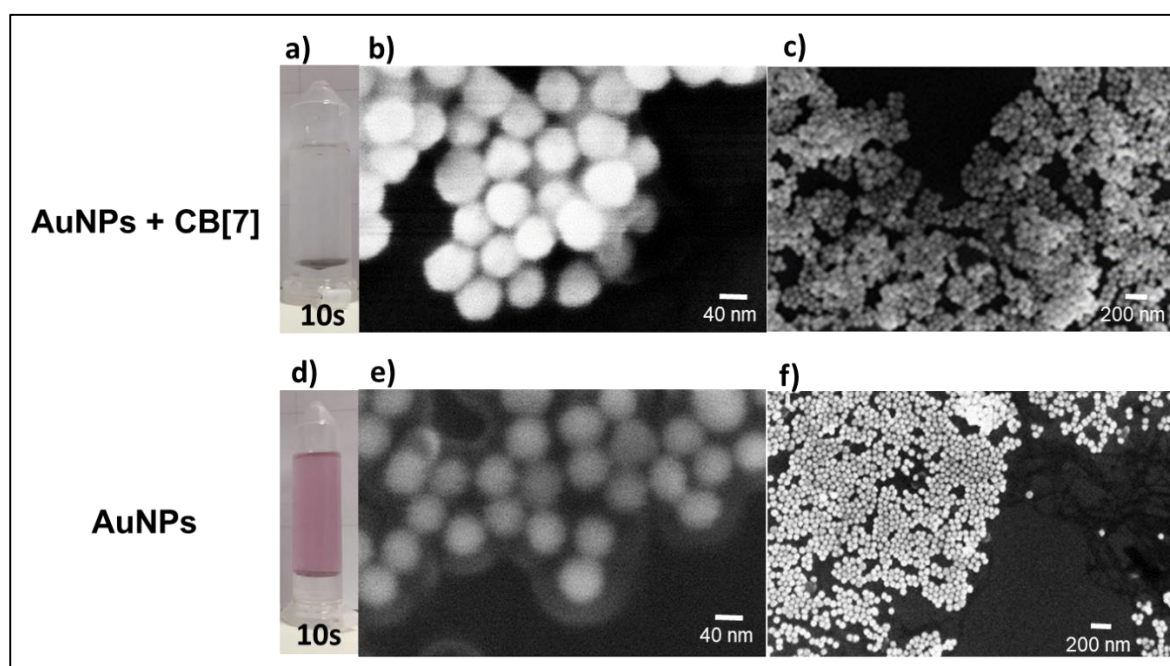
Figure 4.4 a) Image of AuNPs+CB[7] arrays at water/chloroform interface. 1 mL water solution of 60 nm Au nanoparticles coated with citrate were firstly mixed with 50 µL of CB[7] water solution (200 µM) in a Teflon tube (2 mL). The colour of the solution turned to purple immediately from red. Then 0.5 mL of pure ethanol and 0.5 mL of chloroform was added. After vigorously shaking and 10 seconds

waiting, a black film was formed at the interface and the upper bulk water phase became colourless, which indicates that all of the Au nanoparticles transferred to the interface from the water solution in seconds. b)&c), SEM images for dried arrays from AuNPs-CB[7] system; d) Image of AuNPs (without CB[7]) arrays at water/chloroform interface. Ethanol was directly added into Au nanoparticles solution before chloroform. The colour of the water phase remained red after shaking e)&f), SEM images for dried arrays of AuNPs (without CB[7]).

4.2.2 Interfacial substrates for SERS Sensing

SERS sensing was carried out on different formats of interfacial AuNPs arrays. The AuNPs arrays shown in Figure 4.4e&f, even though is very uniformly assembled, are too loose to remain stable under the laser, since the array exposed on the detecting spot tends to move apart once the laser is triggered. The Raman signal obtained, in this case, is too weak to be observed in-situ or in the water/chloroform interface. However, the arrays formed by aggregates clusters, as shown in Figure 4.4b&c, are stable enough under the laser shining point and can provide SERS signals of analytes as SERS substrates.

4.2.2.1 Wet SERS substrates

Two different methods were used to help make AuNPs aggregates to form stable cluster arrays at water/chloroform interface: CB[7] and NaCl. NaCl was used to aggregate Au nanoparticles before ethanol and chloroform were added (See Section 7.4 for more details). SERS was measured from the top of the Teflon container, with laser focusing on the surface of the film at water/chloroform interface through a 5X Nikon lens (See Figure 4.5, see Section 7.5 for experimental details).
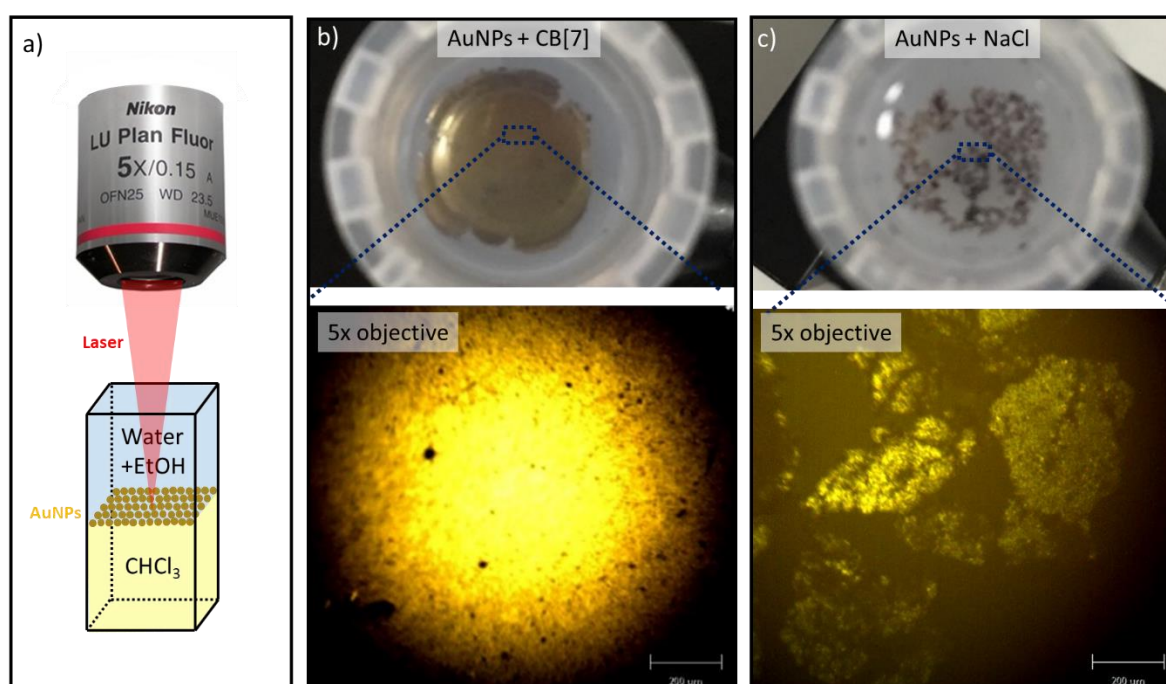
Figure 4.5 a) Schematic illustration of SERS measurement from the top of the container, with Raman detecting spot focusing on the AuNPs arrays at water/chloroform interface. b) Top: a picture of the water/chloroform interfacial arrays formed by AuNPs aggregated by CB[7], taken by mobile phone from the top of the Teflon container. Bottom: a microscopic bright field image of the arrays taken by 5X Nikon lens. c) Top: a picture of the water/chloroform interfacial arrays formed by AuNPs aggregated by NaCl. Bottom: a microscopic bright field image of the arrays taken by a 5X Nikon lens.

Dopamine was used as the SERS signal testing molecule for both systems (System for AuNPs aggregated by CB[7] see Figure 4.6a, and system for AuNPs aggregated by NaCl see Figure 4.6b) were added to the Teflon container after the aggregates film was formed. A concentration series from 0 to 100 μM were carried out. Each concentration SERS data was obtained by taking the average of 3 measurements. For both systems, the SERS spectra intensity increases with the concentration Dopamine characteristic SERS peak at 1640 cm^{-1} was specially analysed in Figure 4.7. For arrays formed by AuNPs aggregated by CB[7], the LOD is around 100 nM while the LOD is 10 nM for NaCl aggregated AuNPs system. However, the AuNPs-NaCl system shows larger error bar than the AuNPs-CB[7] system, which is because it has less compacted array structure than AuNPs-CB[7] system (as shown in Figure 4.5 b&c) and the film pieces tend to move around on the interface with the high laser energy, resulting in less consistency of the SERS sensing data. Moreover, the data of AuNPs-NaCl system saturated when the concentration is above 10μM, which means the detecting range is from 10 nM to 10 μM. However, the data for AuNPs-CB[7] system did not saturate at 10 μM, showing a higher upper sensing range.
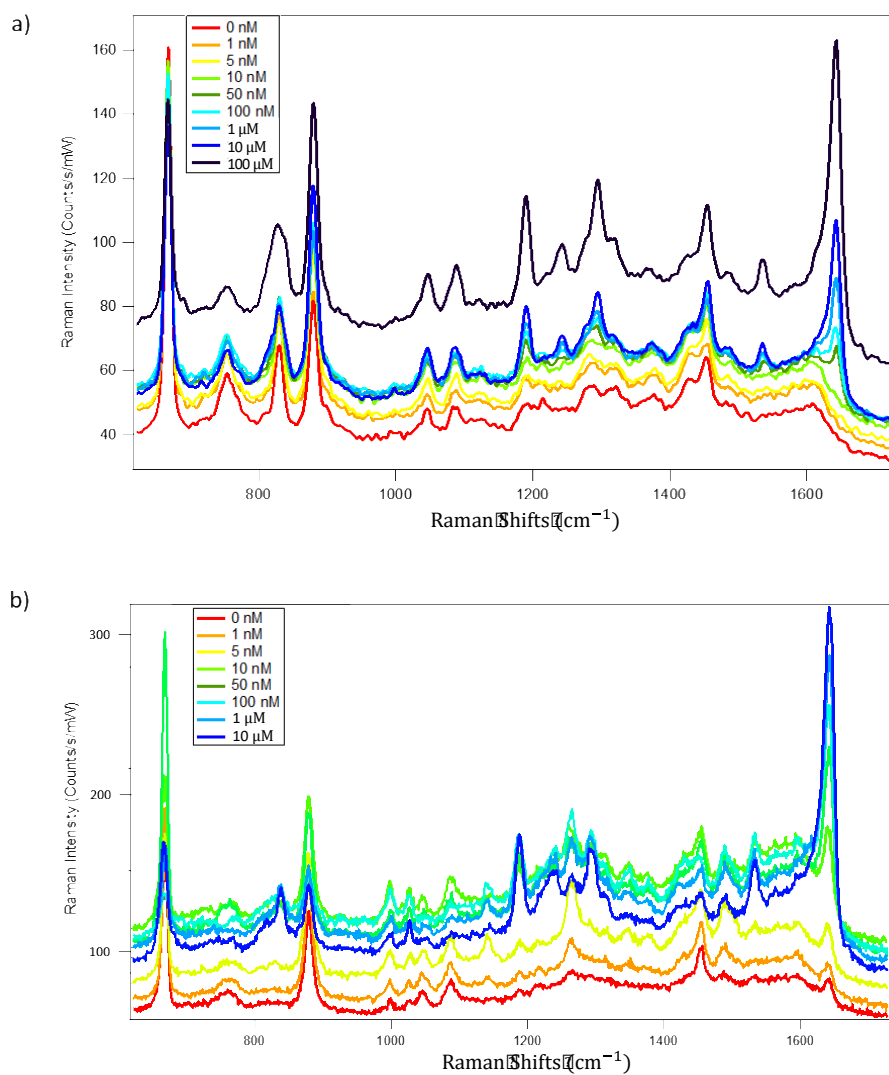
Figure 4.6 SERS spectra of dopamine (concentration from 0 to 100 μM) measured on AuNPs arrays at water/chloroform interface. a) AuNPs aggregated by CB[7]; b) AuNPs aggregated by NaCl.
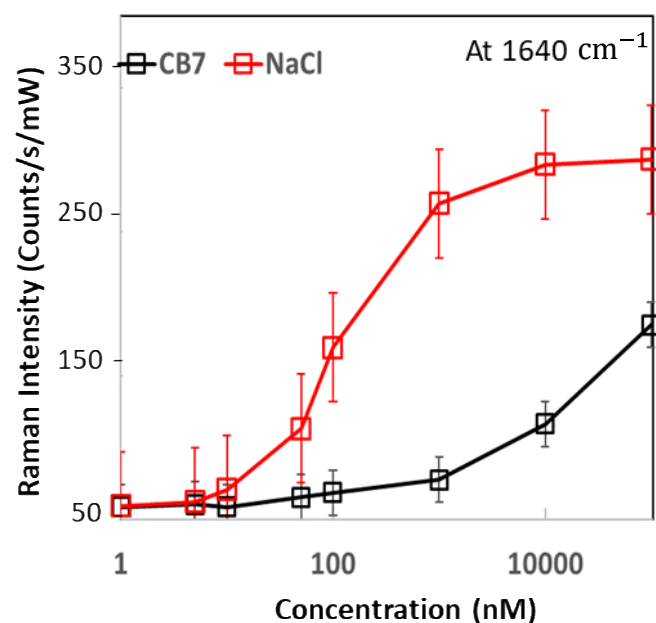
Figure 4.7 Dopamine characteristic SERS peak 1640 cm^{-1} increases with the increase of concentration. Black: LOD at 100 nM for AuNPs-CB[7] sytem; Red: LOD at 10 nM for AuNPs-NaCl system.

4.2.2.2 Dried SERS substrates

Even though the sensing of dopamine shows high sensitivity on wet interfacial AuNPs arrays, the data consistency is not perfect due to the arrays' high mobility on liquids interface while detecting. Potentially, dried AuNPs arrays could help solve the problem of mobility. The AuNPs arrays were taken onto a smooth gold surface and were dried out for 24 hours. The arrays' structure and sensing property as a SERS substrate were then analysed.

To compare the structures of AuNPs arrays from the two systems, tilted SEM images of 45° and 75° were carried out (See Section 7.6 for experimental details). The film can then be observed from the direction of its cross section (Figure 4.8). AuNPs arrays formed by AuNPs-CB[7] system tend to assemble as a compacted and uniform multilayer film, while the arrays tend to form a single layer film by NaCl aggregated AuNPs. This structure explains why the AuNPs-CB[7] arrays tend to stay in one piece in the wet state (Figure 4.5b) since the AuNPs show strong binding affinity to each other by CB[7]. However, NaCl does not help in the same way as CB[7], so the arrays tend to form a single layer with weaker affinity and stay in separate pieces in wet state (Figure 4.5c).

SEM Tilted Degree	CB[7]	NaCl
45°		
75°		
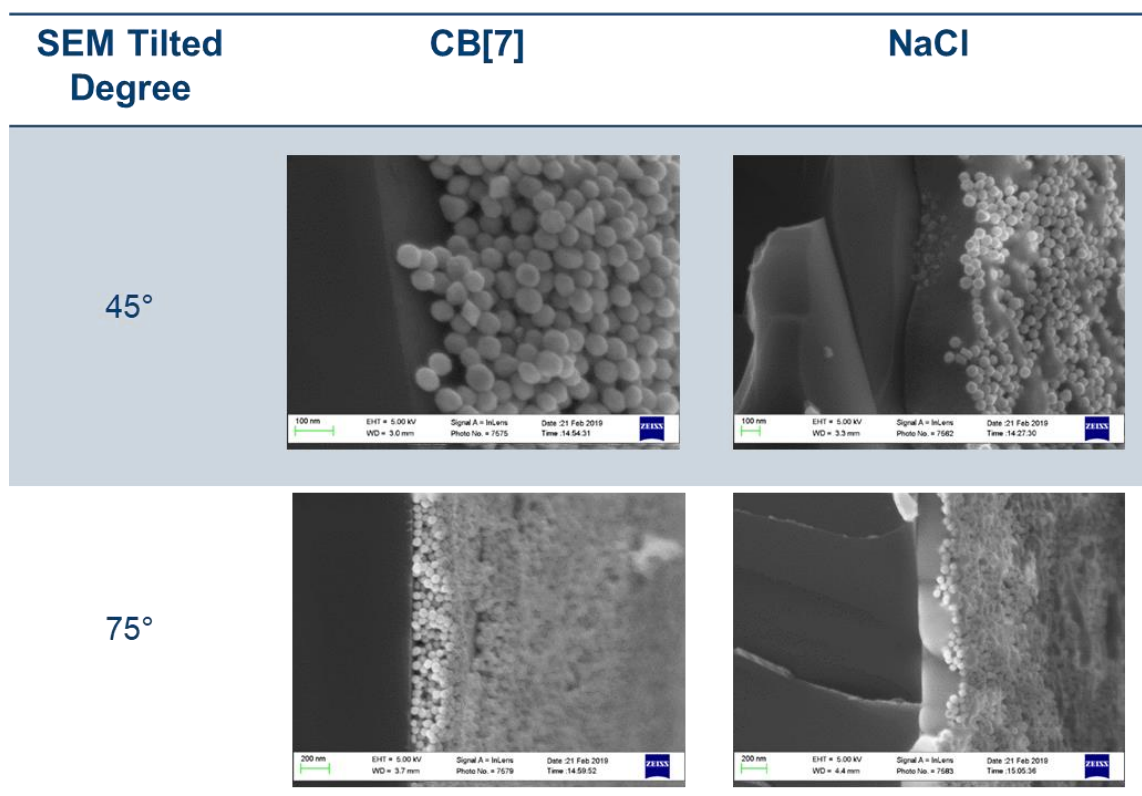
Figure 4.8 45° and 75° Tilted SEM images of AuNPs arrays formed by CB[7] triggered aggregates (left) and NaCl triggered aggregates (right).
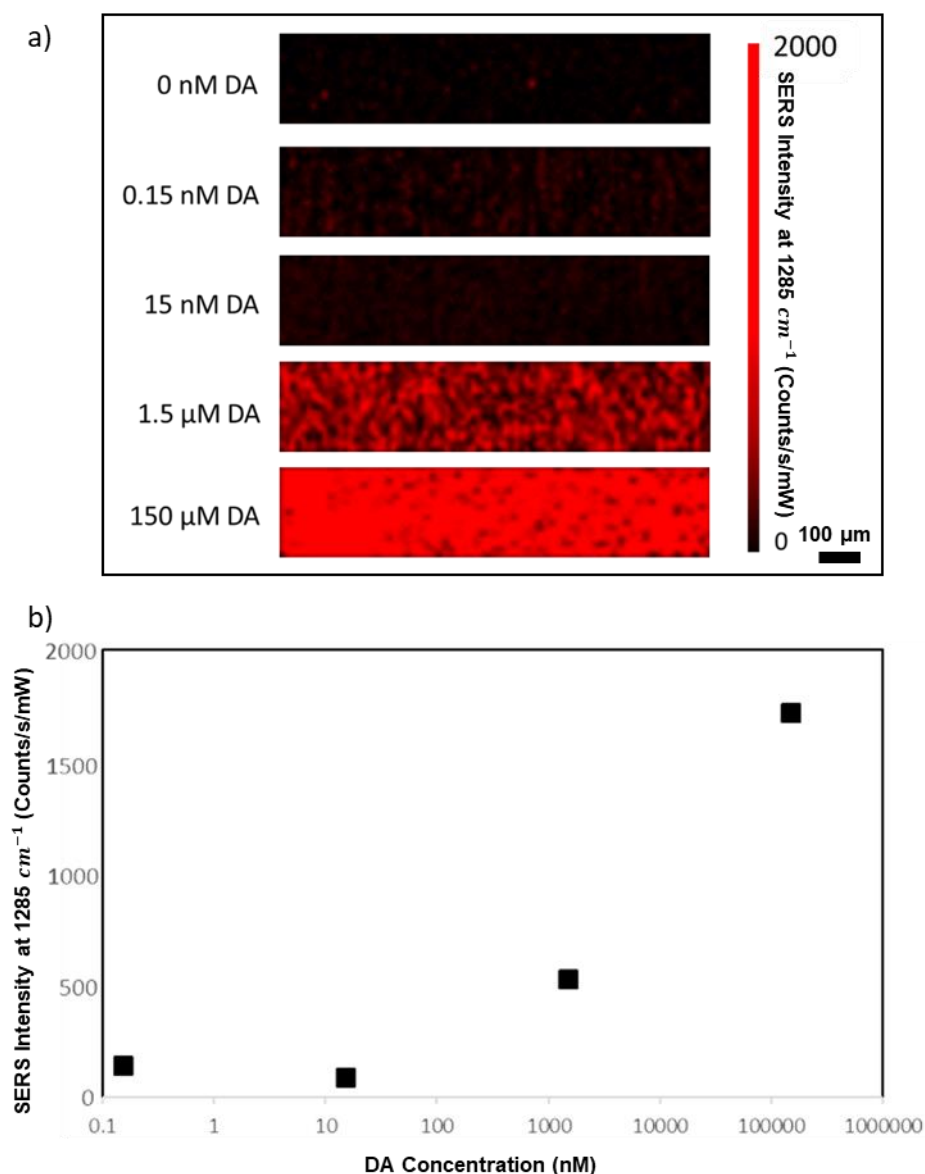
Figure 4.9 a) SERS mapping of dopamine's 1285 cm^{-1} peak across a 1200 μm × 200 μm area on dried AuNPs-CB[7] arrays for a series of samples (dopamine concentrations of 0 nM, 0.15 nM, 15 nM, 1.5 μM and 150 mM respectively); b) Averaged 1285 cm^{-1} peak intensity vs dopamine concentration on dried AuNPs-CB[7] arrays. The LOD is between 0.01-1 μM.

The uniformity of dried AuNPs arrays is not good enough to provide the same SERS data at different detecting spots. Therefore, taking SERS measurements over a certain array surface area and doing data average over this area can be a solution to overcome the poor data consistency at different spots. For dried AuNPs-CB[7] arrays, in order to get more accurate and consistent sensing data, SERS mapping was carried out for different concentrations of analytes dopamine. A series of dopamine samples were prepared (concentration of 0 nM, 0.15 nM, 15 nM, 1.5 μM and 150 mM respectively). For each concentration, 1 μl of the sample was drop-casted on the dried arrays and after the drop was

dried completely, SERS spectra were mapped across 1200 μm × 200 μm areas in 10 μm intervals, with 0.1 s integration time by a 785 nm laser and a 20X lens NA 0.75. As shown in Figure 4.9a, the SERS intensity of dopamine's 1285 cm^{-1} peak is extracted for each spatial position to give a map of SERS emission, normalized to the incident laser power. It is obvious that as the concentration of the samples increase, the overall peak intensity of dopamine increases. By calculating the average SERS intensity of 1285 cm-1 for the mapping area, the intensities of 1285 cm^{-1} vs concentration can be plotted as Figure 4.9b, in which we found that the LOD is between 10 nM to 1 μM.

The same protocol was explored with dried AuNPs-NaCl arrays, however the SERS mapping measurement was difficult for this system, since a large amount of NaCl crystals among the AuNPs arrays significantly influenced the data reproducibility. This SERS mapping method therefore, can only be applied to systems without salt.

4.2.2.3 Microdroplet interfacial substrates

Microfluidic droplets are an efficient tool to provide a confined space for chemical reactions, including the AuNPs-CB[7] aggregating process and the AuNPs assembly process at water/oil interface. Using microfluidics, a droplet interface as a template for SERS sensing provides a potential protocol for on-chip optical sensing. In this section, a simple microfluidics device was designed to generate interfacial AuNPs arrays on a microdroplets interface. As shown in Figure 4.10, AuNPs were firstly mixed with CB[7] solution to generate AuNPs aggregates. These aggregates in aqueous phase were then mixed with EtOH, before confronting the $CHCl_3$ oil phase. Then aqueous microdroplets were generated in continuous flowing oil phase of $CHCl_3$. The reason why EtOH was added after aggregates were formed, was that the EtOH could inhibit the aggregating process if it was added before CB[7], as the extinction spectra shown in Figure 4.10 b&c. In Figure 4.10b, with the rising aggregates band between 700 to 800 nm and decreasing mono mode at 530 nm, the extinction spectra trend shows that AuNPs can aggregate smoothly with CB[7], without EtOH involved. However, when EtOH was firstly mixed with AuNPs, the aggregating process did not happen even CB[7] was added afterwards, as shown in Figure 4.10c. See experimental details in Section 7.7 and 7.9.
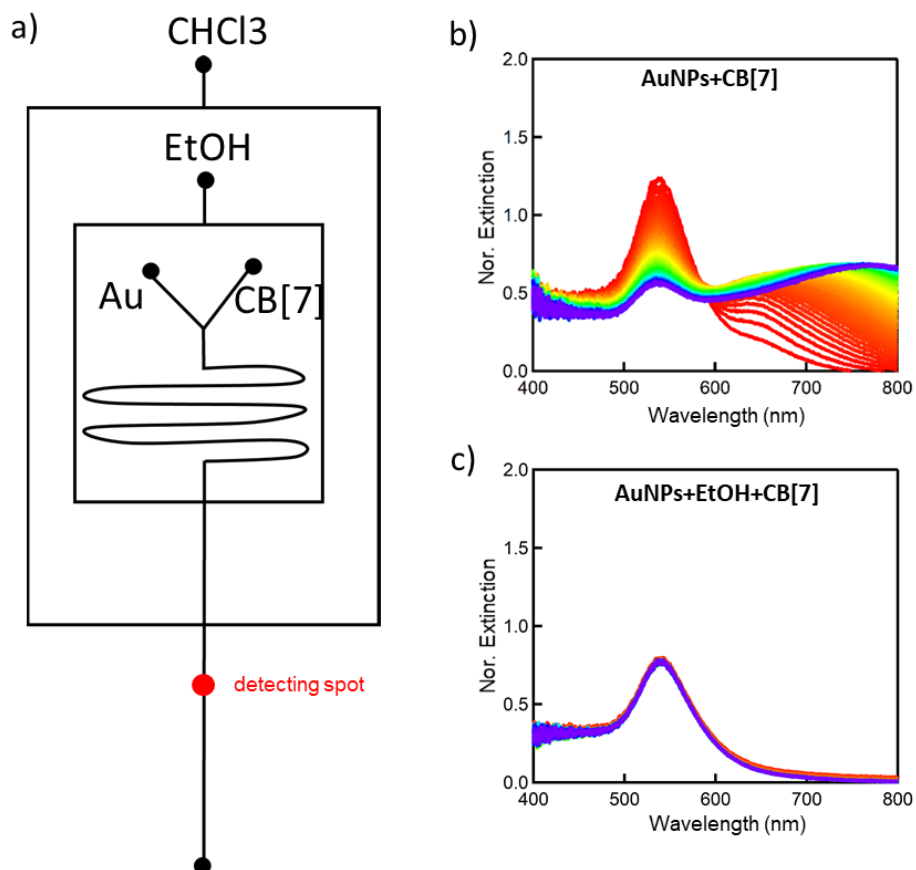
Figure 4.10 a) Microfluidic chip designed to generate aqueous droplets containing AuNPs-CB[7] arrays on water/chloroform interface. Detecting spot on the outlet channel marked with red dot. Microfluidic chip was designed with the help of Dr Ziyi Yu from Abell group and was generated in house. See chapter 7 for details. b) Extinction spectra of AuNPs solution after mixing with CB[7]. c) Extinction spectra of AuNPs solution mixed with EtOH, then mixing with CB[6].

The droplets were collected in a glass cuvette reservoir. The observing light path was changed by 90° in order to observe the droplet horizontally (see Section 7.9 for experimental). The bright field image of the droplet is shown in Figure 4.11a, where the AuNPs arrays on the bottom half of the droplet interface can be clearly observed via 5X lens. The droplet was not fully covered by the AuNPs arrays since the specific surface area is so large that the AuNPs extracted from the water droplet can only cover part of the droplet, even though the AuNPs were concentrated by 10 times before injected into the microfluidic channel.

SERS were measured from top of the droplet vertically with 5X lens. The CB[7] characteristic Raman peak at 830 cm^{-1} was mapped over the area of the droplet cross section at different horizontal planes (Z_0, Z_1 and Z_2 in Figure 4.11b). From the Figure 4.11 c, d and e, we can see that the bright half ring

representing concentrated CB[7] molecules on AuNPs arrays on the droplet interface, become smaller when the detecting z plane is from Z_0, Z_1 to Z_2. At horizon plane Z_2, the half ring becomes a bright spot since the only the bottom of the droplet was measured. This result shows that the AuNPs arrays can assembly at the water/oil microdroplet interface, and be as a SERS substrate for analytes from water phase (CB[7] in this experiment)
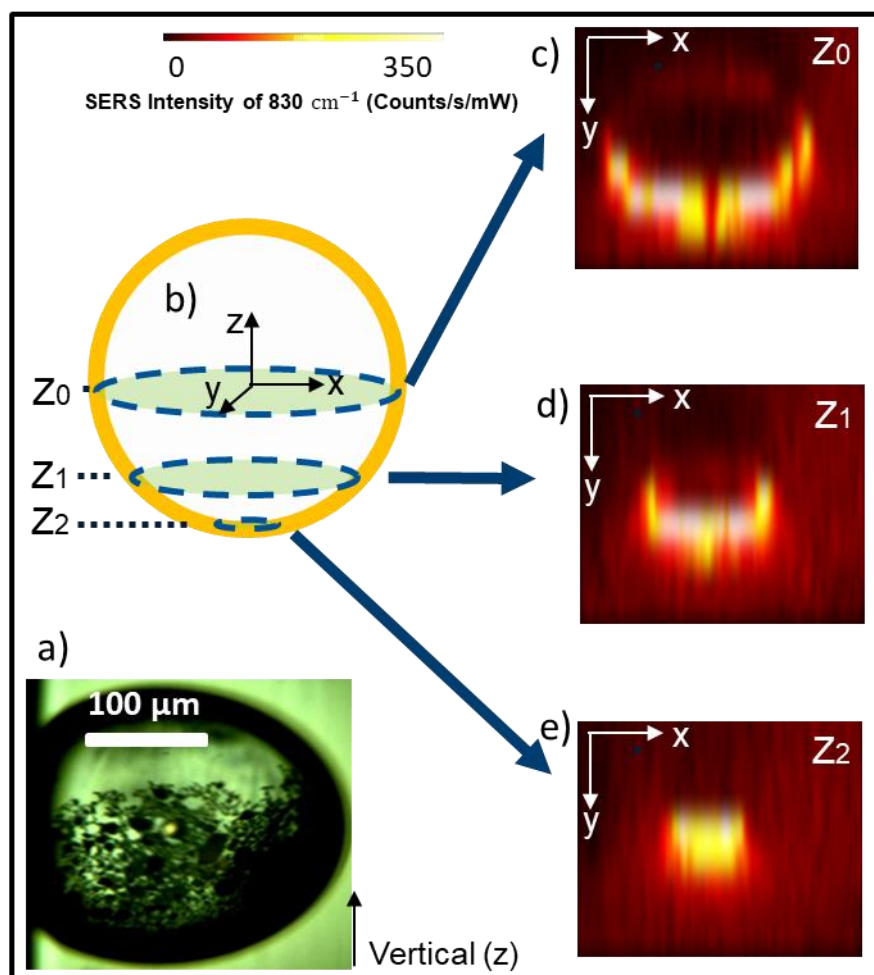
Figure 4.11 a) The bright field image of the droplet covered with AuNPs arrays at interface, observed horizontally. b) Droplet schematic showing SERS mapped horizon planes Z_0, Z_1 and Z_2. c, d, e) The SERS mapping of CB[7] Raman peak at 830 cm^{-1}, over the area of the droplet cross section at z = Z_0, Z_1 and Z_2 respectively.
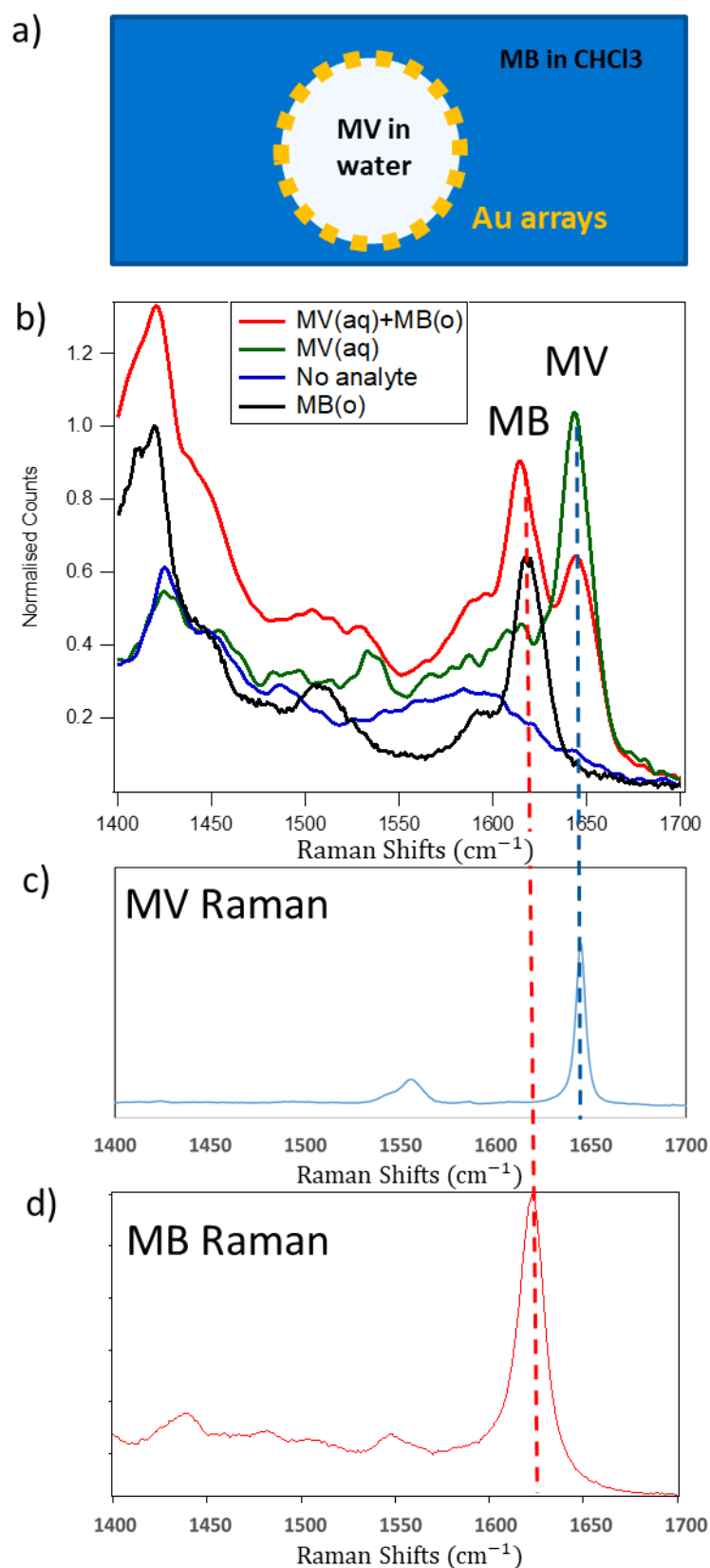
Figure 4.12 a) Schematic of simultaneous SERS sensing of MV in water phase and MB in chloroform

phase, by AuNPs arrays at microdroplet interface. b) SERS spectra of MV in water, MB in chloroform,

compared with none analytes involved. c) Raman spectra of pure MV solution. d) Raman spectra of pure MB solution.

Further exploration was implemented by dissolving methyl viologen dichloride (MV, 10 μM) and methylene blue (MB, 1 μM) into water and chloroform respectively before the liquids were injected into the microfluidic channels (Figure 4.12a). The SERS spectra (Figure 4.12b) detected on the droplet interfacial arrays shows that both MV in water phase and MB in oil phase can be clearly identified by corresponding to their characteristic Raman peaks (Figure 4.12 c and d). This provides a practical protocol for multiphase SERS sensing with microfluidic droplets.

4.3 Summary

In this chapter, Au nanoparticle 2D arrays were developed with the CB[n] molecules as well as by NaCl, and the arrays are analysed as SERS sensing substrates in different forms. The stability of the interfacial arrays was studied in terms of the influences from AuNPs surface wettability and AuNPs/clusters sizes. AuNPs covered CB[7] or citrate tend to stay at the water/chloroform interface and show high desorption energy. AuNPs clusters assembled by CB[7] are more stable at the interface than un-aggregated single AuNPs, due to higher Helmholtz energy change.

Quantitative SERS sensing was carried out on wet and dried AuNPs interfacial arrays, both of which showing a LOD down to nM levels. Furthermore, microdroplets interfaces were used as the gold nanoparticle array templet for SERS sensing, which provide huge potentials for its applications in microfluidic SERS sensing. SERS sensing of analytes from multiple phases were also analysed in this chapter to further widen its application scenarios. This method provides a versatile protocol for direct SERS sensing of various of analytes.

Chapter 5 SERS sensing in droplet-based microfluidics

5.1 Background and motivation

5.1.1 SERS in droplet-based microfluidics

Droplet-based microfluidics has been proved to be a promising platform for performing chemical and biological experiments with ultra-small volumes (picoliter to nanoliter) (see section 1.1). The ability to analyse the contents in a droplet qualitatively and quantitatively is crucial to broaden the applications of droplet-based microfluidic systems. Microfluidic approaches can provide consistent geometries, so detection in microchannels can be implemented in a strictly controlled environment, allowing repeatable signals be detected. As one of the optical sensing techniques used on microfluidic chips, SERS can be an alternative technique to fluorescence-based detection with its label-free detecting ability on the chemical structure of molecules. To implement SERS sensing in droplet-based microfluidics can help minimize the required sample volumes, the integration time, and decrease the damage to the target analytes, which is especially important for biological analytes. In chapters 2, 3 and 4, SERS sensing was analysed systematically and quantitatively by AuNPs aggregates in bulk aqueous solution and on assembled AuNPs arrays at water/oil interface. With all the understanding on the nature of AuNPs aggregates SERS measurements, integrating the AuNPs aggregates substrates with droplet-based microfluidics can potentially provide a powerful sensing platform for in-situ detection.

The first application of Raman spectroscopy in droplet-based microfluidics system was reported by Cristobal.[165] Two non-fluorescent compounds mixed within one droplet were detected at different points along the microfluidics channel, by using the high resolution Raman spectroscopy (Figure 5.1a). For other examples, chemical reaction processes[166] as well as UV-induced polymerization[167] were monitored in droplet microfluidics by Raman spectroscopy. Chemical synthesis was reported with SERS sensing with droplet-based microfluidics.[168] Silver nanoparticles (AgNPs) were used as the SERS substrates in nanolitre droplets to monitor the reactants injected by a co-focusing structure. SERS measurements were carried out at different positions along the channel, which represented different chemical reaction time scales. In this way, the time-resolved changes of characteristic Raman peak intensities can be obtained in each droplet. Hantzsch synthesis of 2-aminothiazoles were monitored within the droplets, and chemical reaction conditions were optimised. Similarity, Fenton degradation process of dyes was analysed by online SERS in droplets.[169] The sedimentation of iron ions was reduced efficiently in droplet system, compared to bulk solution system. The aggregation and sedimentation of the SERS substrate was also reduced, so that a stable reaction environment was provided within

droplets. The droplet-based microfluidic technique has also been proved to help improve the repeatability of SERS signals by eliminating the "memory effect", which is crucial for the development of most optical sensing technologies with microfluidic channels.[170]
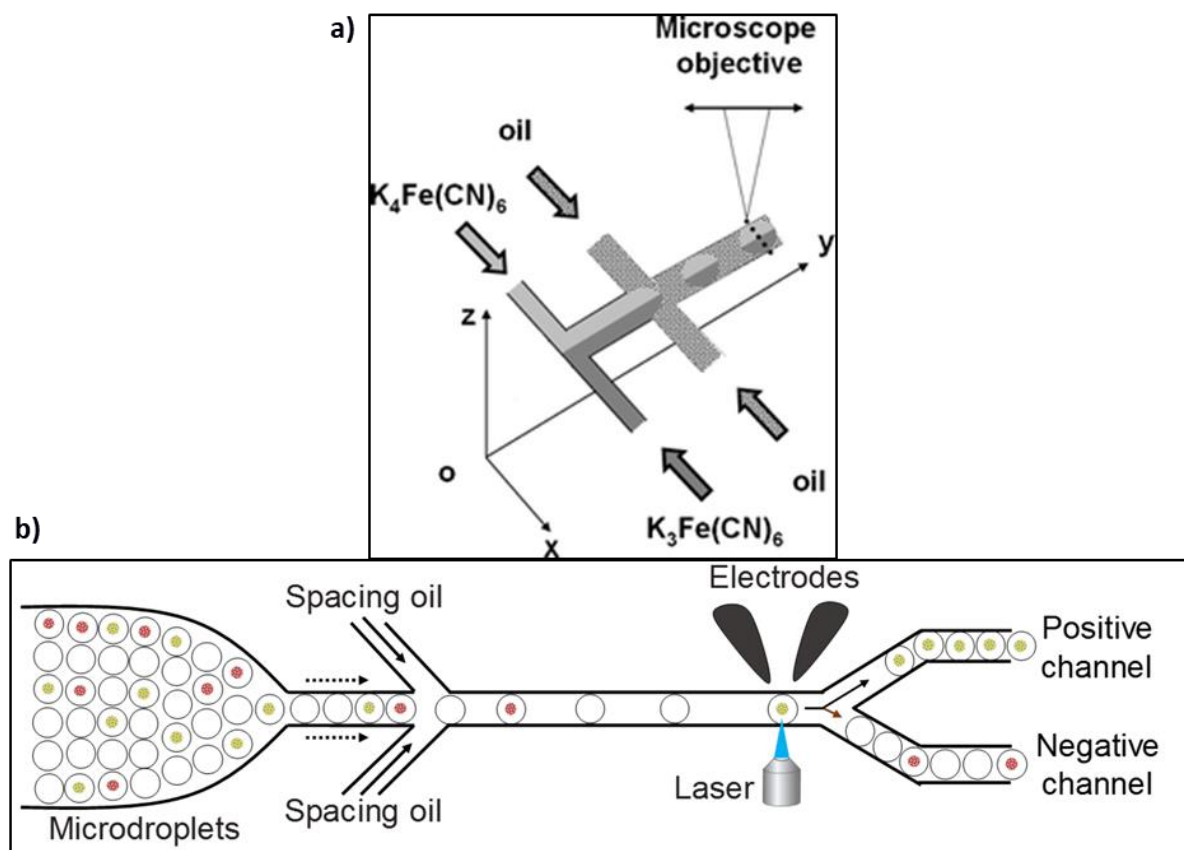
Figure 5.1 a) Two fluids co-flow and form droplets at a flow focusing junction, then detected by Raman spectroscopy. [165] b) Schematic representation of a platform for microfluidic sorting of encapsulated protoplasts.[171]

Microfluidic approaches can provide consistent geometries, so SERS detection in microchannels can be implemented in a strictly controlled environment, allowing repeatable signals be detected. The SERS measurement in droplet-based microfluidics can help minimize the required sample volumes, the integration time, and decrease the damage to the target analytes, which is especially important for biological analytes. In addition, the microfluidic-SERS systems can help to combine many fluids manipulation processes, such as sample preparation, target separation and in situ detection into one experiment, which can help to significantly improve the sensing platforms' effectiveness. Generally, microfluidic devices are made from glass, PDMS (polydimethylsiloxane) and other polymers, among which PDMS is the most widely used material. However, one problem with PDMS is that this is a Raman active material which may interfere with the SERS signal obtained from analytes in the channels. In order to solve this problem, confocal microscopy is usually applied as only a small volume

of sample is detected and the Raman signals of PDMS material can be effectively removed using this method.

In this chapter, the same method as described in chapters 2, 3 and 4 was used to generate the AuNPs aggregates using CB[n] in microdroplets as SERS substrates, which could be used for chemical sensing in a high throughput way. CB[n] molecules have advantageous properties such as defining the gap size as 0.91 nm and binding small molecules inside CB[n] molecules so that the analytes can sit exactly inside the hotspots of the substrates. The aggregating process will be analysed systematically by dark field and bright field microscopy. As the results of chapter 2&3 and 4, CB[n] molecules are helpful for controllable assembly of AuNPs so that quantitative sensing is possible within microdroplets. Methyl viologen (MV), a typical Raman active molecule, which can strongly bind to CB[7] and CB[8] will be applied as a test analyte for the microdroplets SERS sensing system. The MV SERS scanning in flowing droplets will also be discussed. Additionally, to understand the aggregates behaviour in droplets, the position of aggregates in microdroplets will be analysed based on the bright-field images, videos and SERS spectroscopy.

5.1.2 Droplet-based microfluidics high-throughput sorting

Recently, droplet-based microfluidics has gained increasing popularity as a platform for high-throughput culture, manipulation, sorting, and analysis of up to millions of individual cells under diverse conditions.[172–176] This approach is based on nanolitre-volume aqueous microdroplets which spatially separate individual cells from one another during processing. Different properties have been used for the quantitative analysis of chemicals inside droplets to trigger the dielectrophoretic force, for example, fluorescence spectroscopy which is successfully commercialised. Typically, as shown in Figure 5.1b, on-chip sorting of droplets containing protoplasts from wild type cells were implemented using dielectrophoresis force.[171] An optical detection setup integrated into the microfluidic channel was used for high-throughput quantification of fluorescence emitted by individual encapsulated protoplasts. As the microdroplets passed through the objective field of view, they were illuminated by a laser. The emitted fluorescence signal was collected and simultaneously, a pulse generator connected to a high-voltage power supply was triggered. The triggered electrode pulse could deform the fluorescent positive microdroplets and target them to a small 'positive' channel for collection. If the microdroplet was empty or contained protoplast lacking detectable fluorescent signals, the detector then sent no signal and the microdroplet passed through the larger 'negative' channel. The droplet-based microfluidic system integrated with electrodes in this way can rapidly measure and automated sort the individual encapsulated protoplasts based on their fluorescence intensity. To date, droplet-based microfluidics has primarily been applied to bacteria,[177–180] unicellular eukaryotes,[181,182]

and non-adhesive mammalian cells.[183,184] Other sensing techniques, such as absorption spectroscopy, Raman spectroscopy, and droplet morphology are actively under development for droplets screening. [185]

The aim of this project is to address some fundamental problems related to developing a microdroplets-SERS sensing system, which can potentially be built as an effective microdroplets high-throughput sorting system in the future. The prospect of utilizing this platform for characterization and screening of individual microdroplets is highly attractive. For example, microalgae are a potential source of sustainable biofuels because they have the ability to produce high value products, such as β-carotene, omega-3 oils and ethanol. In order to optimise the microalgae aquaculture, it is crucial to screen the most productive cell species and microdroplet based screening platform could be an efficient technique to achieve this.

There are several basic problems to solve in this project, for example, fundamental aspects of gold nanoparticle aggregation in microfluidics, SERS in microdroplets at one droplet scale and SERS scanning of flowing droplets. In this chapter, these fundamental problems are analysed systematically and thus we build a foundation for further research on microdroplets-SERS sensing sorting system.

5.2 AuNPs aggregates formation in microdroplets

AuNPs-CB[n] aggregates are important SERS substrates both in microdroplets and in microgels. Before examining the SERS sensing property of microdroplets and microgels, it is important to understand the SERS substrates assembly process and potential issues that may affect SERS sensing behaviour, such as refractive index matching between the water and oil phases.

Dark-field scattering (See Section 7.1.3) has been used to spectroscopically characterise the AuNPs self-assembly process with CB[5] both in bulk solution and in a microfluidic channel. Figure 5.2a shows that the formation of aggregations in bulk solution being tracked by dark-field spectra. In the experiment, CB[5]: AuNP concentration ratio was $20 \times 10^{-9} \, \mu M \, mL$, which means the assembly process was diffusion-limited (refer to Figure 2.1), with assembly time of 7 seconds. The 'monomer' mode at around 530 nm was observed, corresponding to the single nanoparticles or transverse mode of aggregates chains. 'Dimer' and 'aggregate' modes were observed upon adding CB[5] . The dominant spectra trend shows noticeable red shifts, which means long chains of AuNPs aggregates were formed with longer time. With the comparison of experimental data to simulated data (solid black dots, showing the wavelength of the scattering spectra versus the number of nanoparticles per chain on the right-hand axis, data supplied by Dr Andrew Salmon of Cavendish Lab NP group/ Abell research group), it indicates that several AuNPs form the active chains.

Based on the analysis of AuNPs assembly in bulk solution, the same process was examined in microfluidic droplets. Figure 5.2c shows the microfluidic device used in this research and the bright field image of the flowing droplets. The continuous oil phase is FC40 with surfactant Pico-Surf2. Due to the different reflective index of water (n = 1.333) and FC40 (n = 1.290), there is a strong reflection on curved water-oil interfaces under the light illumination. This reflection is a strong interference factor, compared to the relative weak dark-field spectroscopy from nano aggregations. Therefore, it is necessary to match the reflective index of oil phase to that of water phase. According to previous work in the group,[128] the refractive index of FC40 is matched by adding 33.2 v/v% 1,3-bis (trifluorometryl)-5-bromobenzene (n=1.427, Sigma-Aldrich). Figure 5.2b left and right show the microdroplets in reservoir in reflective index unmatched and matched oil respectively. The boundary of water and oil phases can be clearly seen when the oil is not refractive index-matched, while in the refractive index-matched oil, the boundary can be hardly seen.

The dark field spectra of droplets at different channel positions are shown in Figure 5.2d. When AuNPs and CB[5] was just mixed at the 'Y junction', only The 'monomer' mode was observed, which means the AuNPs have not been aggregated. After the droplets generated and flowed by position 1-4, the longer wavelength mode dominated the spectra, despite the fact that the 'monomer' mode still existed. The spectra measured from position 2, 3 and 4 were fairly the same, showing that there was no noticeable change on aggregates after position 2. The aggregation process finished before position 2 (distance from mixing point is approximately 250 µm), which took 2 ms flowing time from the mixing point. The time for aggregation process in microdroplets is much shorter (2 ms) than that in bulk solution (7 s), since the mass transfer is vastly accelerated within the flowing microdroplets due to the inner circular chaotic advection.

The AuNPs in microdroplets collected in the reservoir after the outlet channel are shown in Figure 5.2e and Figure 5.2f. Nothing can be observed in droplets when there is no CB[5] added (Figure 5.2e), however AuNPs aggregates (bright dots) can be clearly observed with CB[5] involved under the dark field microscope(Figure 5.2f). A possible sketch of aggregates with several AuNPs attached by CB[5] molecules is shown in Figure 5.2g.
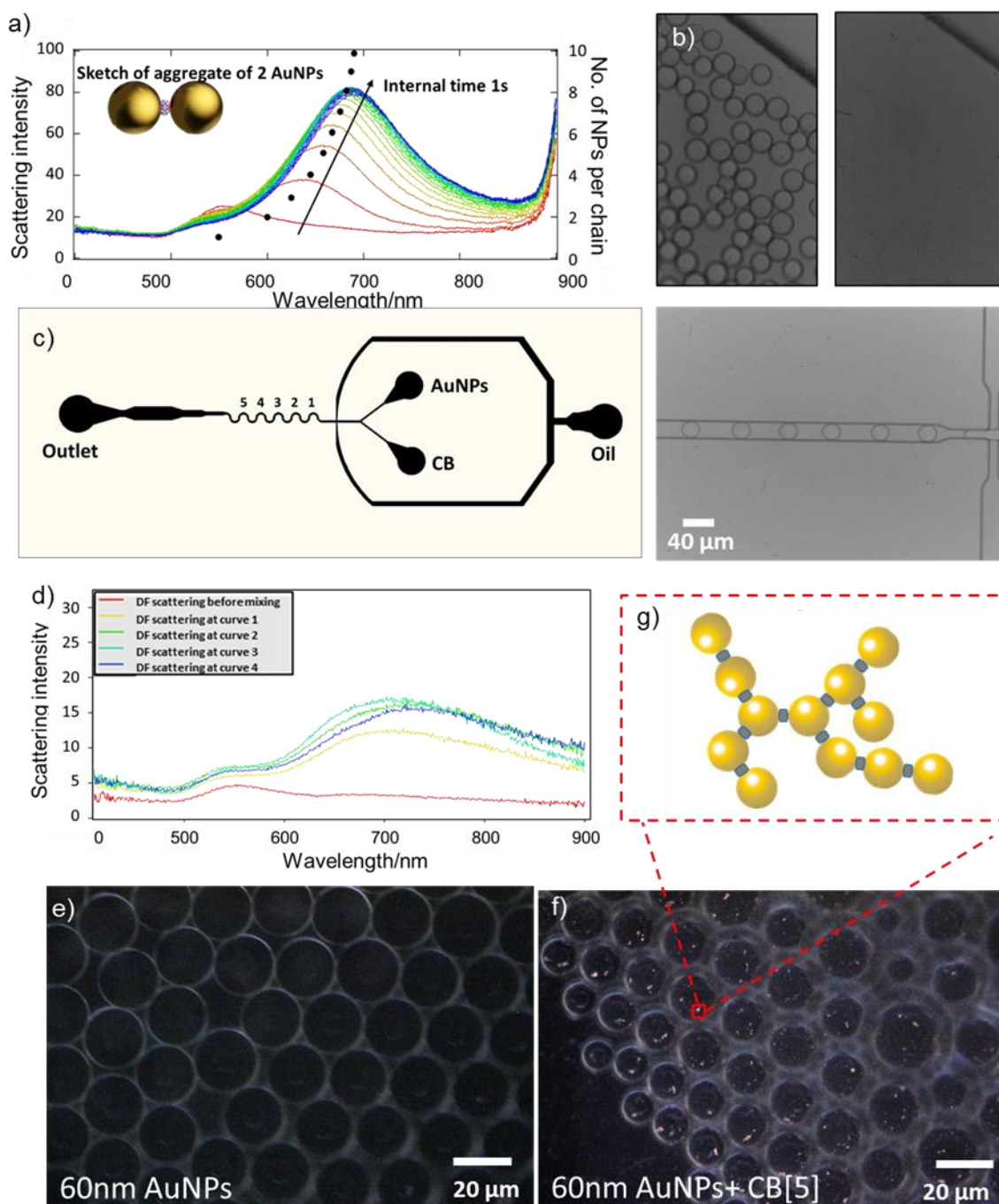
Figure 5.2 a) Dark field scattering spectra of AuNPs aggregating in bulk solution (left axis) and simulated wavelength of the scattering spectra versus the number of nanoparticles per chain (right axis, data supplied by Dr Andrew Salmon of Cavendish Lab NP group). 1 mL of 60 nm AuNPs from BBI was mixed with 100 μl of 1 mM CB[5], and scattering spectra were obtained with 1000 ms internal time and 3 ms integration time. b) Microdroplets in reflective index unmatched (left) and matched (right) oil FC40 (with 5 wt% Pico-Surf2, Dolomite). c) Microfluidic chip device (left) and bright-field image of flowing droplets in microfluidic device just after generated (right). The device was made by PDMS bonding to a glass base, with the main channel width of 20 μm and height 20 μm. There are

three flow inlets (AuNPs suspension, CB[n] solution and oil phase, respectively) and one flow outlet. The AuNPs are 60 nm purchased from BBI and the concentration of CB[5] is 10 mM, with the same flow rates of 100 μl/h. The flow rate of continuous oil phase is 250 μl/h. d) Darkfield scattering spectra of AuNPs aggregations in microfluidic droplets, measured at the microfluidic device positions 1, 2, 3, 4 as well as the 'Y junction' where AuNPs and CB[5] were mixed. e)&f) AuNPs in microdroplets collected in the reservoir after the outlet channel. e) No aggregates in droplets when there is no CB[5] added in droplets. f) AuNPs aggregates can be clearly observed under dark field microscope. g) A possible sketch of aggregates with several AuNPs attached by CB[5] molecules.

5.3 SERS in microfluidics

5.3.1 SERS in flowing droplets

As stated in previous, by putting target analytes inside CB[n] molecules, SERS can be detected by this aggregates-CB[n]-analytes complex. Before moving forward to the microfluidic SERS sensing for analytes that are of interest, some fundamental problems of microfluidic SERS sensing need to be solved first. These studies can be facilitated by using strong Raman-active analytes such as methyl viologen (MV). MV SERS detection in bulk solution, in microdroplets, and positioning aggregates in microdroplets will be discussed in this chapter.
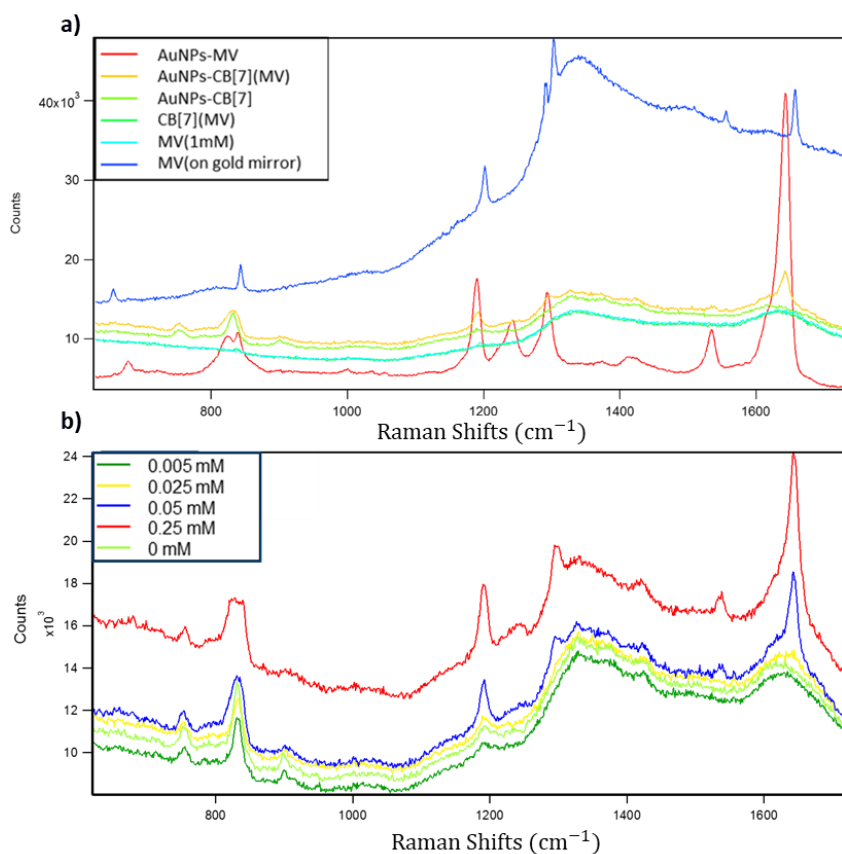
Figure 5.3 a) Raman/SERS spectra of CB[7] and MV in different conditions. CB[7] and MV solution are both 1 mM in water. b) SERS spectra of different MV concentrations detected by colloidal AuNPs-CB[7] aggregates. MV solution (25 μl) mixed with CB[7] solution (1 mM, 25 μl), then 250 μl of AuNPs (60 nm) were added.

Raman, as well as SERS spectra of CB[7] and MV in different conditions, are shown in Figure 5.3a. From SERS signals of MV on a gold mirror (blue), the strong peaks of 843, 1202, 130, 1658 cm^{-1} and weak peaks of 1291, 1556 cm^{-1} can be clearly observed. These peaks can also be obtained in the mixture solution of AuNPs and MV (red), although they are all blue shifted (842.9 to 839.6 cm^{-1}, 1202 to 1190 cm^{-1}, 1302 to 1293 cm^{-1}, 1556 to 1539 cm^{-1} and 1658 to 1643 cm^{-1}, respectively). The assignments of some of the above MV SERS peaks to chemical bonds are shown in Table 5.1. These blue-shifted peaks are also shown in the spectra of AuNPs-CB[7]-MV system, where CB[7] SERS signals (751, 831, and 1191 cm^{-1}) can simultaneously be observed by correlating with the AuNPs-CB[7] SERS spectra (light green). Among these 3 peaks of CB[7], 751 cm^{-1} is from CB[7] molecules, while 831 cm^{-1} slightly overlaps with MV's blue shifted 840 cm^{-1} peak and 1191 cm^{-1} overlaps with MV's blue shifted 1190 cm^{-1}. For the system of pure MV or MV-CB[7] mixture, no SERS signal can be observed as no gold substrates are involved.

1190	s (N-CH$_3$)
1293	δ (H-C-C)
1302	s (C-C)
1534	s (C-N) on ring
1643	s (C-C) on ring

Table 5.1 Assignments of the MV Raman peaks to chemical bonds

The Figure 5.3b shows SERS spectra of different concentrations of MV dissolved in 1 mM CB[7] solvent. Theses spectra are all measured in bulk solution without any microfluidic device. When the concentration is higher than 0.025 mM, all the five characteristic MV peaks can be clearly observed,

while with lower concentrations, peak 1293 cm^{-1}, 1535 cm^{-1} and 1643 cm^{-1} are weak. Therefore, the concentrations below 0.025 mM are not suitable for analysis of microfluidic SERS due to low signal intensities. A concentration of 0.25 mM was chosen to do the following microfluidic SERS analysis.
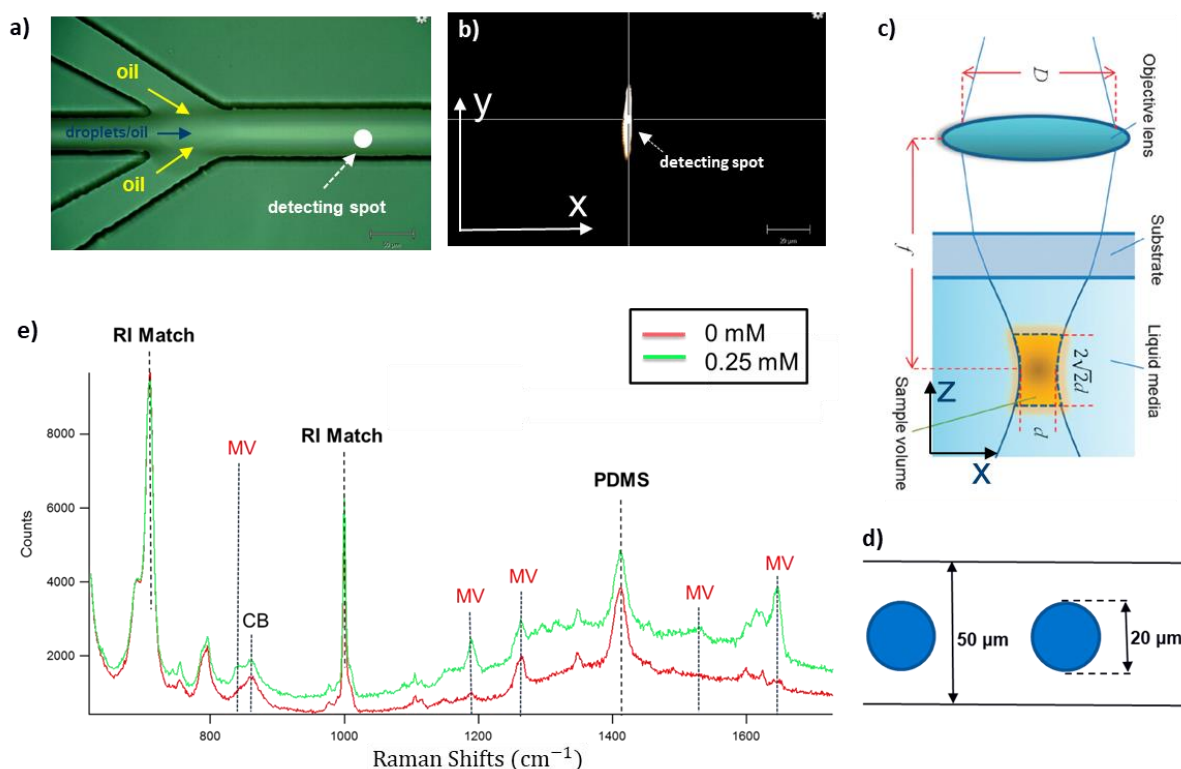
Figure 5.4 a) Microfluidic device for observing SERS. The channel width along Y axis is 55 μm, and the channel height along z axis (perpendicular to x-y plane) is 50 μm. The CB[7] concentration is 1 mM with 0.25 mM MV dissolved in it. b) The laser source through a lens in bright field image; c) the SERS detecting point of the system is in the shape of a column; d) scheme of droplets flowing in the channel; e) methyl viologen SERS in flowing microdroplets.

To observe the SERS signals from flowing droplets inside microfluidic chips, two different morphologies of microfluidic chips were used: one for droplet generation (Figure 5.2c, the flow rates for oil phase, AuNPs solvent and CB[7]@MV are 40 μL/h, 20 μL/h and 20 μL/h respectively) and another for observing the SERS signal (Figure 5.4a). The reason that different chips were used for generation and observing is that, the droplets size is highly correlated to droplets generation frequency, which means that the SERS detection frequency could hardly be tuned if the droplet size is fixed. In order to manipulate the detection speed and evaluate the factors affecting the detection of results, the flowing frequency should be tuneable while the size of the droplets is fixed. Therefore, a separated microfluidic device needs to be introduced for SERS detection. By analysing high-speed

video of the droplet generation, the generation frequency can be measured at approximately 1000 per second.

The droplets containing AuNPs aggregates then were collected into a 1ml plastic injection syringe, with small amount of oil phase prepared beforehand to prevent droplet deformation or coalescence during the collection process. These collected droplets in an oil mixture then were re-injected into the observation device as the dispersed flow, along with the same oil phase injected as the continuous flow to adjust the frequency of the droplet in the outlet channel where SERS signals were detected.

The detecting point of the system is in the shape of a column, as shown in Figure 5.4c, with the column base in x-y plane and height h along z axis. The diameter of the column base is defined as d, which can be calculated by equation $d = \frac{1.22\lambda}{NA}$,[186] where λ is the excitation laser wavelength and NA is the numerical aperture of the optical lens. The height h can be estimated approximately by $h = \frac{\pi d^2}{2\lambda}$. The SERS droplets detection process was observed with Raman microscope using an Olympus long-distance 50X objective with $NA = 0.5$, and 785 nm excitation laser. Therefore, the detection spot has a diameter d = 2 µm in x-y plane and h = 8 µm, which are all shorter than the channel dimensions, allowing the detection spot be fully embedded inside the channel. Figure 5.4b shows the laser source through a lens in bright field image, which is in a shape of a sheet rather than a spot. The sheet length in y-axis is around 35 µm and the width along x-axis is about 4 µm in the sheet centre. The sheet volume can also fully cover the detecting volume inside droplets.

Microdroplets containing Au aggregates with and without analyte MV were generated, collected and then injected into the detection device. One typical droplet size is 20 µm, whose flowing scheme in the channel is shown in Figure 5.4d. The SERS spectra of droplets with and without MV in flowing microdroplets in the detection device is shown in Figure 5.4e. The sample containing MV shows extra peaks at positions 840 cm^{-1}, 1293 cm^{-1}, 1535 cm^{-1} and 1643 cm^{-1} with a peak 1190 cm^{-1} overlapping with that of CB[7]. High concentration of AuNPs ($C = 2.6 \times 10^{12}/mL$) is crucial in this experiment since in microfluidic channels, low concentrations of AuNPs ($C = 2.6 \times 10^{11}/mL$) do not provide strong enough MV SERS signals that can compete with the complicated background signals from oil phase and PDMS.

5.3.2 Aggregates position in microdroplets

When carrying out SERS analysis in moving microdroplets, it is important to find the proper confocal plane of the droplets, where the AuNPs aggregates have the highest possibility to be located.

Aggregates from two different AuNPs concentrations were analysed. Figure 5.5a and b show images of flowing microdroplets in a microfluidic channel and reservoir respectively, with a high concentration of 60 nm AuNPs ($C = 2.6 \times 10^{11}/mL$). While flowing in the microfluidic channel, aggregates can hardly be observed with bright field microscopy because the aggregates are at a very early stage of the assembly so the size is too small. However, by the time the droplets were collected in the reservoir, the aggregates were always large in size, and can be observed under bright field microscopy (Figure 5.5b). With low concentration of AuNPs ($C = 2.6 \times 10^{10}/mL$), even after a long assembly time of 10 min, only small aggregates could be observed under dark field microscopy. In the video of droplets under darkfield microscopy, it was found that the aggregates move following a track of a circle in one half of the droplet, as illustrated in Figure 5.5d. In the microfluidic channels, the droplets inner flow is similar to those in the reservoir, and the AuNPs aggregates follow the half circulating movement in the droplets when they are in channels.
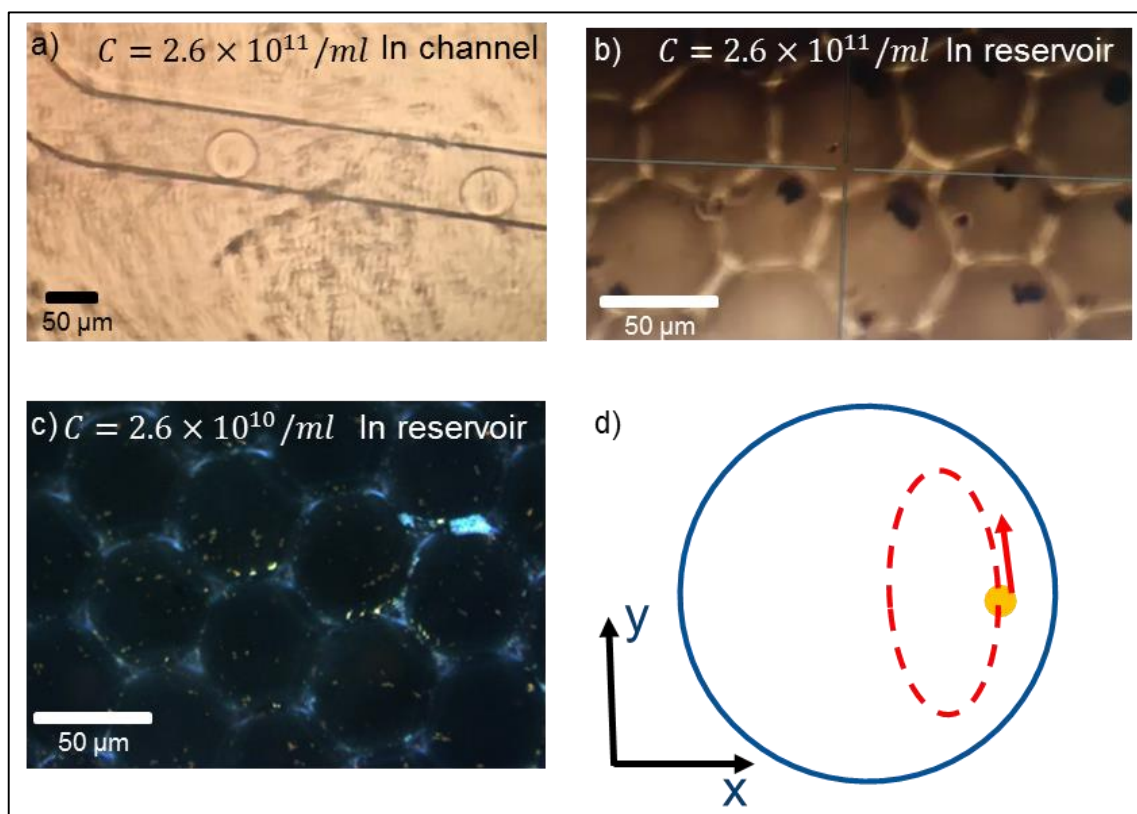
Figure 5.5 a-c) Images of microdroplets in microfluidic channels and reservoir. a) Microdroplets flowing in a microfluidic channel. Aggregates of AuNPs can be hardly observed with bright field microscopy because the aggregates are at a very early assembling stage and the aggregates size is too small to be observed. b) Droplets collected in the reservoir after 10 min since the AuNPs were mixed with CB[7]. The AuNPs aggregates were large enough (up to a few μm in dimension) to be observed under bright field microscopy. The inlet AuNPs concentration used was $C = 2.6 \times 10^{11}/mL$. c) With

a lower concentration ($C = 2.6 \times 10^{10}/mL$)of AuNPs, after the same assembly time 10 min, only small aggregates can could be observed under dark field microscopy. d) Sketch illustrating that the AuNPs aggregates follow a half circulating movement in the droplets in the x-y plane.

There is a question as to what is the position of aggregates along the z axis. After the microdroplets are resident in the reservoir for 1 hour, they stop moving and so do the aggregates (Figure 5.6a and b). By examination of the z axis SERS scanning at the point of the large aggregates (Figure 5.6c), MV was dissolved in CB[7] to be a SERS marker on the AuNPs aggregates in droplets. SERS spectra of MV along z axis were shown in Figure 5.6 e-f). The z = 0 position was found and set when the edges of all the microdroplets can be clearly seen in refractive index unmatched oil. Figure 5.6e-f shows that the spectral intensity increases as z increases when z is below 12 µm, but decreases as z decreases when z is above 12 µm. The position z = 12 µm shows the strongest SERS signal of MV, which means the AuNPs aggregates stay on the plane which is 12 µm under the sphere centre. Also, after plotting the SERS intensity of 1643.1 cm^{-1} (one of MV SERS peaks) versus z axis, position of the AuNPs aggregates can be clearly found at z = 12 µm. When z is over 10 µm, the signal intensity increases sharply as z increases, until z reaches 12 µm, but drops sharply when z is over 12 µm until z reaches 14 µm. Therefore, confocal planes at z = 10 µm to z = 14 µm are all good for detection by SERS, among which z = 12 µm is the best position.

In stationary microdroplets (d = 50 µm), the aggregates are observed moving in half circles on the confocal plane which is 12 µm below sphere centre. This conclusion was drawn from stationary microdroplets, however, in moving droplets, this detection plane might change due to the complex influences on aggregates from inner circulating flowing, gravity force and interfacial tension.
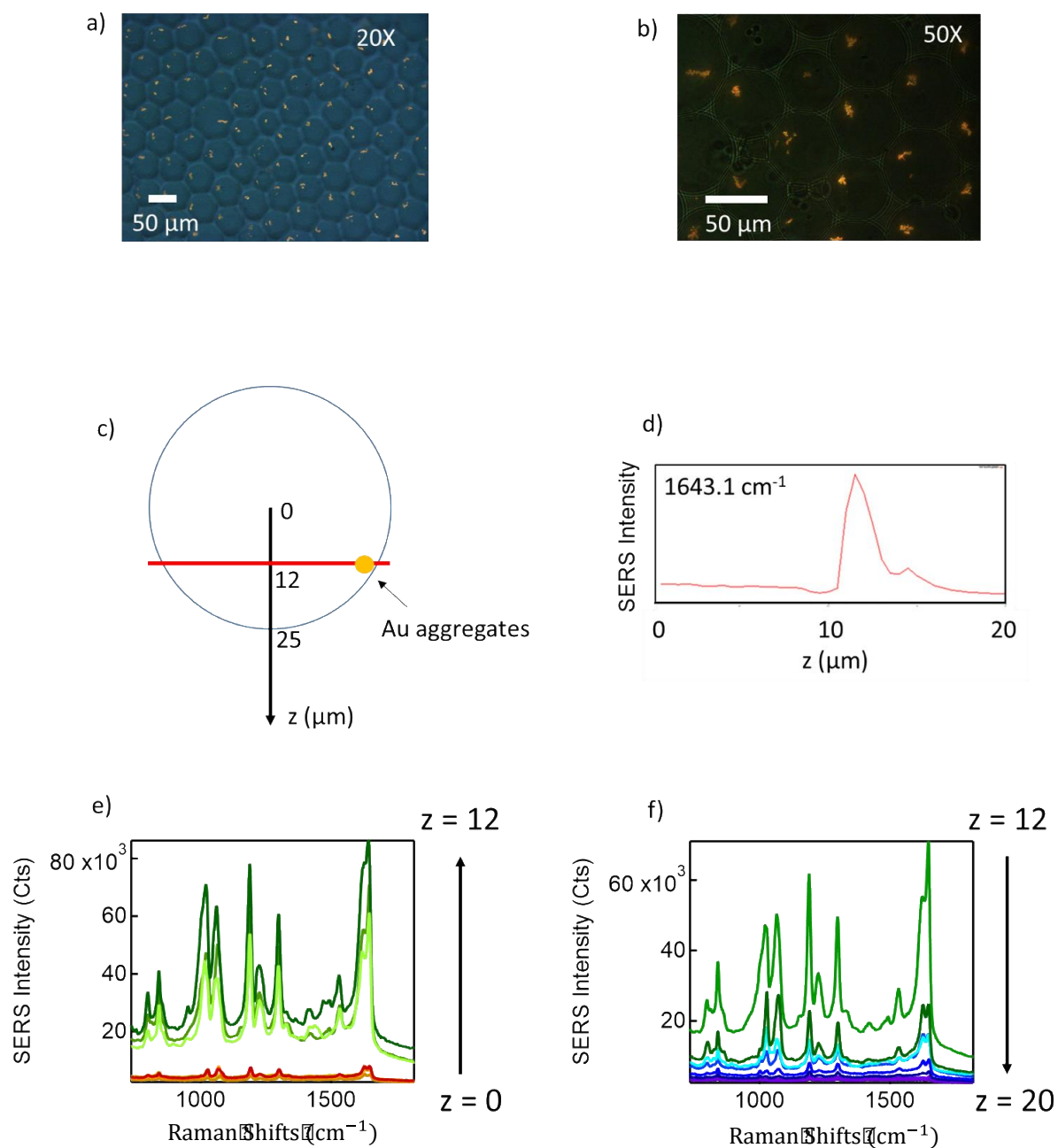
Figure 5.6 a-b) Images of stationary microdroplets under dark microscopy after the microdroplets were resident in the reservoir for 1 hour (20X and 50X magnification respectively). c) Sketch of z axis SERS scanning from z = 0 μm, which is the confocal plane of sphere centre. The scanning step was 1 μm. The yellow dot represents AuNPs aggregates in a stationary microdroplet. d) MV peak 1643.1 cm^{-1} SERS intensity versus z axis. 0.5 mM of MV was initially dissolved in 1 mM CB[7] solution to be a SERS spectra marker on the AuNPs aggregates in the droplets. e-f) Full MV SERS spectra results from z = 0 to 12 μm and 12 to 20 μm respectively.

5.3.3 SERS scanning of flowing microdroplets

SERS scanning of flowing microdroplets is a fundamental technique for high throughput droplet sorting based on SERS spectra in microfluidic channel. 0.5 mM MV was dissolved in 1 mM CB[7] as a SERS marker to be examined by SERS scanning in flowing microdroplets.

The Renishaw Raman Spectrometer has a minimum integration time 0.01s, and the minimum gap between every two scans is 0.02s. Consequently, to find the matched integration times for certain flowing rates is important. Here, different integration times were tested for stable slowly flowing droplets. A typical SERS scanning raw data is shown in Figure 5.7a, which shows 200 continuous SERS scans with an integration time of 0.01s, time intervals as 0.02s. In Figure 5.7a, the distinguishable peaks of MV, CB and oil phase can be easily observed with those spectra which have significantly high intensity. However, Figure 5.7a is not easy to analyse since a huge number of scans are put into one figure. The 200 SERS mapping along scans is shown in Figure 5.7b, which can be an alternative way to analyse the raw data. The colour bar represents the intensity on the certain Raman shifts, where the distinguishable peaks of MV, CB and oil phase can be easily observed. The droplets containing MV can be detected and distinguished in flowing assays.

Furthermore, since the background intensity is so high that it may cover some information in the scanning map, the background is subtracted by the smoothing curve of each spectrum. As shown in Figure 5.7c, the above spectrum is raw data, and the bottom one is the spectrum after background subtraction. Figure 5.7d shows the SERS intensity at peak 1646 cm^{-1} (MV) along with scans before and after background subtraction. The figure on the right shows a clearer signal intensity change along with continuous scans. Some of the scans show significantly high intensity which means that enough SERS aggregates and analytes are passing through the detecting spot during one measurement. Others showing little intensity are because no droplets are passing by during one measurement and only oil is detected. Those with medium intensity can be the measurements of combining oil and a small amount of SERS substrates which pass through the detecting spot.

Therefore, ideally, the signal of MV (eg 1646 cm^{-1}) and oil (eg 756 cm^{-1}) should show an inverse relationship. By using the same approach to obtain the intensity changes of oil peak at 756 cm-1, and combining the result with that of MV peak 1646 cm^{-1}, Figure 5.8 a-d represent the results of integration time 0.01s, 0.05s, 0.1s and 1s, respectively. The intensity of 1646 cm^{-1} vs intensity of 756 cm^{-1} was also plotted as shown in Figure 5.8 e-h, representing integration time of 0.01s, 0.05s, 0.1s and 1s respectively. By comparing the data of these four integration times, we can see that the inverse relationship between these two peak intensities gets less and less clear with the increase of integration time. Specifically, when the integration time is 0.01s or 0.05s, most data sit in the region

near the diagonal, close to the high intensity region of 756 cm^{-1}. This is mostly because the droplets space is quite large compared to the droplet diameter, and when the integration time is short, oil phase is more likely to be exposed in the detecting spot during measurements and water droplets are less likely to be detected even though they can potentially show higher intensity once detected. While for the case with long integration time such as 1 second, the volume of oil passing by the detecting spot is roughly the same for each scan. Therefore, the oil SERS intensity does not change significantly.

However, the intensity of MV still varies even though there are similar amounts of droplets passing through the detecting spot. This is because the AuNPs aggregates keep moving around inside the droplets while flowing, so the amount of aggregates passing by the detecting point is random. To address the problem, generating even smaller droplets could be an effective approach. Once the droplets containing aggregates are small enough (d < 2 μm), the detection spot can cover the whole droplets (along all x, y and z axis) and all the AuNPs aggregates inside droplets can be assured to be detected. Once this issue is solved, the absolutely quantitative SERS sensing within flowing microdroplets could be achieved so that SERS based microdroplets sorting system can be built and applied to further cell screening.
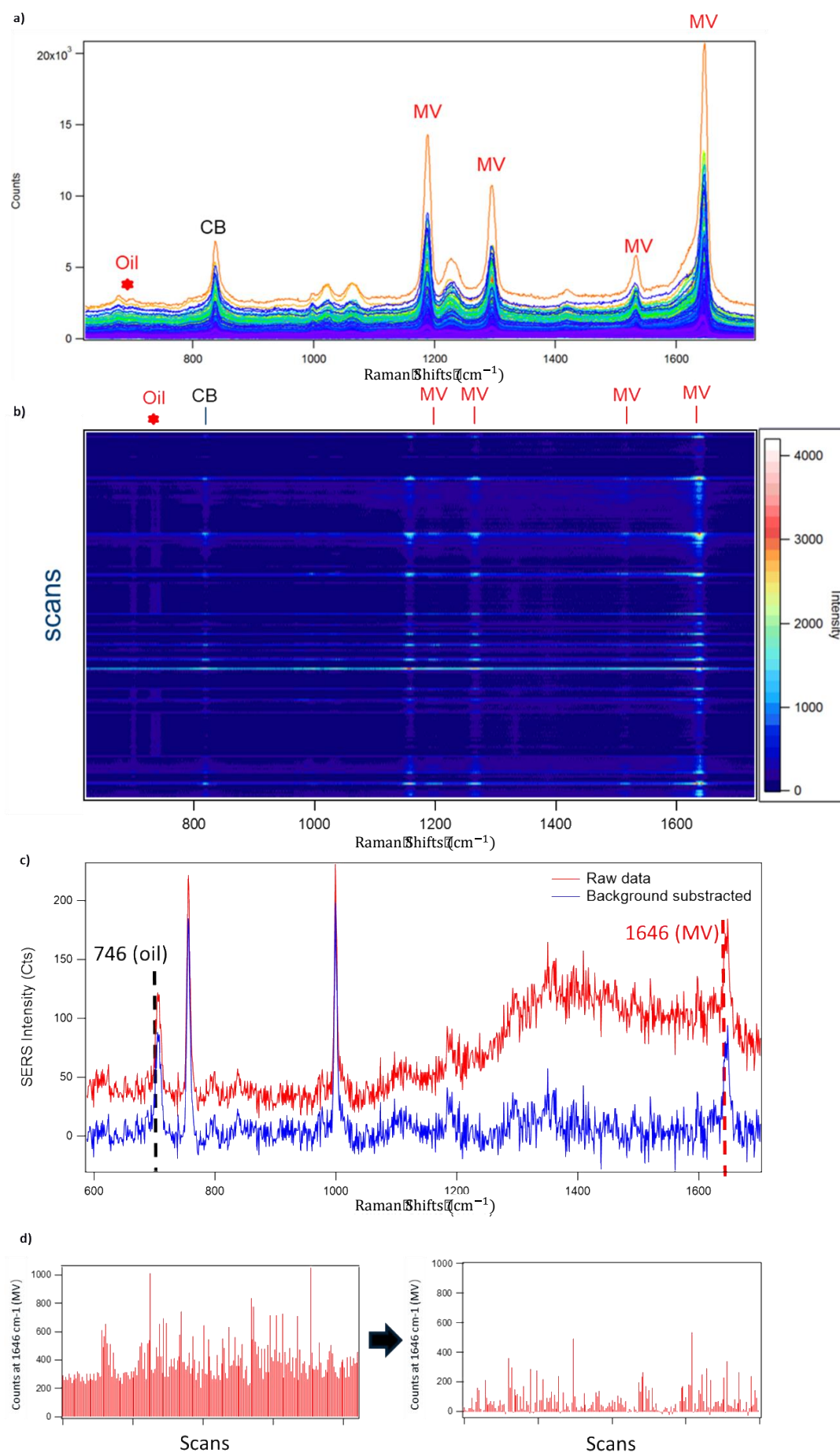
Figure 5.7 a) A typical SERS scanning of 200 continuous flowing droplets measured with an integration time of 0.01s, time intervals as 0.02s. 0.5 mM of MV was initially dissolved in 1 mM CB[7] solution to be a SERS spectra marker on the AuNPs aggregates in the droplets. Droplets generating frequency is about 25/s; b) SERS mapping along scans. The colour bar represents the intensity on the certain Raman shifts, where the distinguishable peaks of MV, CB and oil phase can be easily observed; c) Each SERS spectrum before and after background subtracted; d) MV SERS intensity at peak 1646 cm-1 of each spectrum along scans before and after background subtraction.
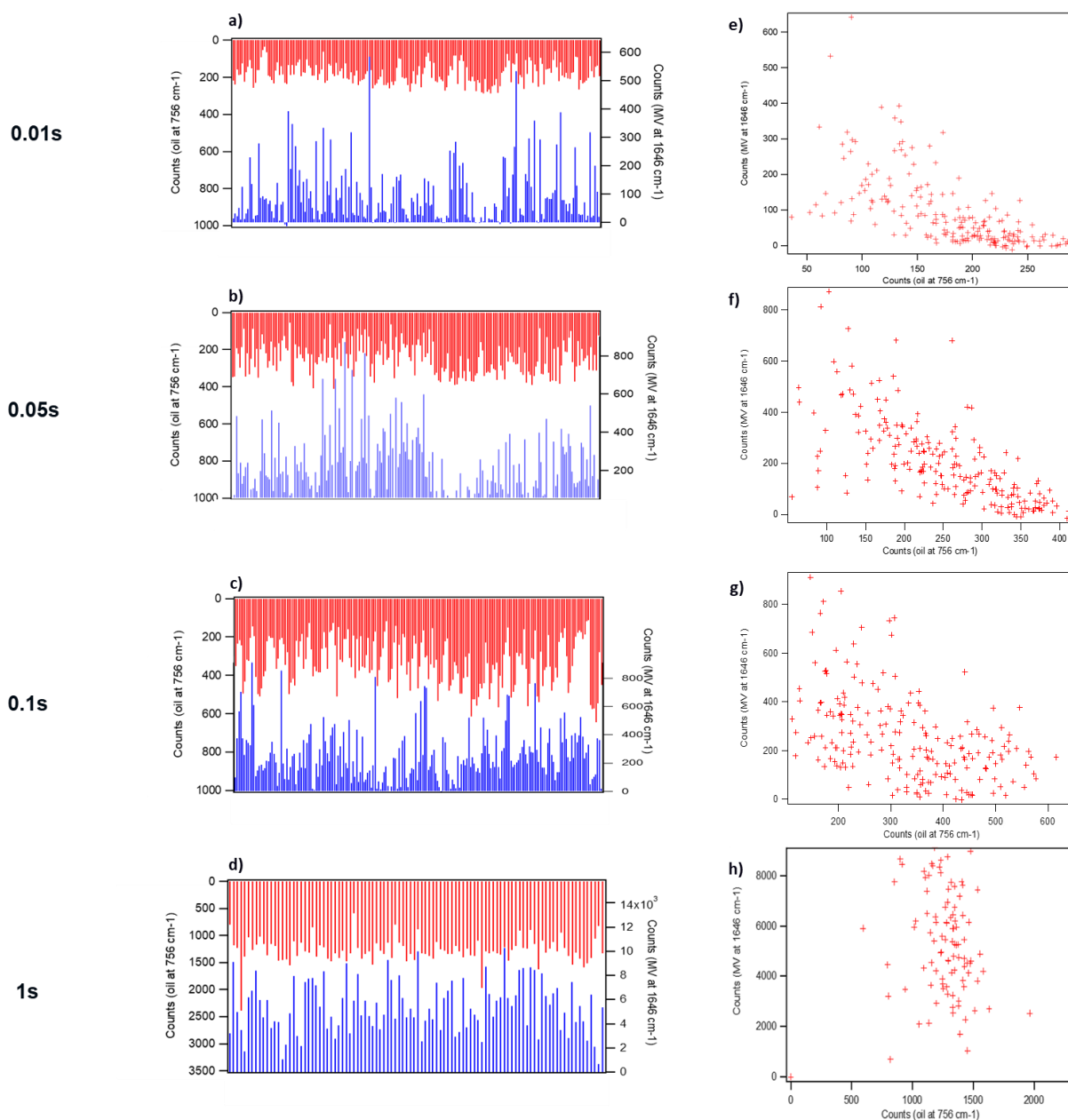
Figure 5.8 a-d) Intensity changes of oil peak at 756 cm^{-1} (red) and MV peak at 1646 cm-1 (blue), integration time is 0.01s, 0.05s, 0.1s and 1s respectively; e-h) intensity of 1646 cm-1 vs intensity of 756 cm-1, integration time is 0.01s, 0.05s, 0.1s and 1s respectively.

5.4 Summary and outlook

In this chapter, a number of fundamental problems related to droplet-based microfluidic SERS sensing were analysed. AuNPs aggregated by CB[n] were generated in microdroplets as SERS substrates, which could be used for chemical sensing in a high throughput way. The AuNPs aggregating process has been analysed systematically by dark field and bright field microscopy. SERS in microdroplets has been further explored. Methyl viologen, as a SERS marker, was tested in flowing microdroplets when the AuNPs are in high concentration. The position of aggregates in microdroplets has been explored based on the images, videos and spectra. In stationary microdroplets (d = 50 μm), the aggregates were shown to be moving in a half circulating movement on the confocal plane which is 12 μm below droplet sphere centre. The positioning of aggregates can help when detecting SERS signals from aggregates, helping to get the strongest spectrum of analytes. Then the inverse relationship between signal of MV and oil was observed by SERS scanning online in flowing droplets, when the integration time is as short as 0.01 to 0.05s.

These results can potentially be helpful for building an effective microdroplets high-throughput SERS sorting system in the future. For example, microalgae, which have ability to produce high value products such as ethanol, could be an application of this system. In order to optimise the microalgae aquaculture, it is crucial to screen the most productive cell species effectively and microdroplet based SERS screening platform could be an efficient label free sensing technique to achieve this. Using the similar protocol as neurotransmitters in Chapter 2&3, ethanol was systematically analysed in bulk solution by SERS using CB[6] as the host-guest molecule. The results show that with AuNPs-CB[6]-ethanol system, the ethanol detection limit can get down to 0.001 vol% in water solution. See Section 6.2.2 for details of SERS detection on trace ethanol in water solution. However, these explorations were implemented in bulk ethanol solution rather than in the microfluidic channel. There are still many challenges in order to detect trace ethanol in flowing microfluidic droplets quantitatively and even more challenges in order to detect the ethanol produced by microalgae cells encapsulated by flowing droplets. Apart from the challenges brought by the unmatched SERS integration time and the droplet flowing time, the challenges from the background noises, the system complexity and the SERS signal reproducibility all can provide interesting and meaningful research topics to future researchers.

Chapter 6 Summary and Outlook

6.1 Summary

Dopamine is one of the important catecholamine neurotransmitters, however its concentration in body fluid system is only 0.01-1 µM[138], and there are many kinds of interfering substances for example amino acids, nucleic acids, glucose, therefore it is difficult to distinguish dopamine from other molecules in body fluids by conventional detection methods. Raman spectroscopy can identify corresponding molecules based on the characteristic peaks of substances, so is a useful method to detect dopamine or other neurotransmitters.

In chapter 2, a simple and efficient 'mix-and-measure' method was used to form a liquid sensing platform by Raman/SERS. The basic research of dopamine Raman/SERS sensing in water solution was covered. Firstly, dopamine Raman spectra at different pH environments is discussed. Density functional theory (DFT) calculations were carried out to help understand the dopamine molecules' chemical bonds resonance modes. A Dopamine concentration series for Raman spectroscopy were carried out to determine the detection of limit of dopamine in pure water which was measured to be in the range of 250 mM.

Further, in order to decrease LOD of dopamine, the Raman signal was enhanced by surface enhance Raman spectroscopy (SERS). Gold nanoparticles were used as the SERS substrates for dopamine detection. The AuNPs assembly process, dopamine-AuNPs binding methods by either CB[n] molecules or Fe(III) ions and weak binding directly by dopamine molecule to Au surface was discussed. Time-resolved extinction spectroscopy was also applied to track the AuNPs aggregates formation process. CB[n]-induced and NaCl-induced AuNPs aggregation processes both show three extinction spectra features ('monomer' mode, 'dimer' mode, 'aggregate' mode) which indicate that the plasmonic modes of complex aggregates are governed by these three chain subunits. Dopamine LOD was 1 µM for NaCl-induced AuNPs aggregates SERS, and was 0.1 to 1 µM for CB[n]-induced AuNPs aggregations SERS, which reaches the level of physiological dopamine concentration in urine.

Iron (III) was also introduced as a binding agency for dopamine and AuNPs. Two distinct protocols ('PreNP' and 'PostNP') are compared, which differ in the steps for forming SERS sensing complexes, affecting both the LOD and the DA SERS intensities. Characterising complexation of Fe(III) and dopamine (DA) in different pH suggests that Fe(III)DA2 dominates in PostNP detection, whilst in PreNP it is the monomeric Fe(III)DA that is seen. When the pH in solution is extremely acidic (basic), protonation (deprotonation) of the hydroxyl bonds of DA becomes competitive to their binding to Fe(III), leading to a decrease (increase) in SERS. Consequently, the dopamine limits of detection 1 to

10 nM by dopamine-Fe(III)-AuNPs complex SERS, which enables to perform fast detection of multiplexed neurotransmitters (NTs) at physiological concentrations.

In chapter 3, other neurotransmitters including EPI, NEPI, DOPA and SERO are tested by SERS using the same complexes scheme of AuNPs-Citrate-Fe(III)-NTs. DA, EPI, and NEPI can all reach LOD at 1 nM, which is below the range of physiological concentration. DOPA and SERO however, show lower detecting sensitivity and the LOD is 100 nM.

In chapter 4, Au nanoparticle 2D arrays were developed with the CB[n] molecules and by using NaCl, and the arrays are analysed as SERS sensing substrates in different forms. The stability of the interfacial arrays was studied in terms of the influences from AuNPs surface wettability and AuNPs/clusters sizes. AuNPs covered CB[7] or citrate tend to stay at the water/chloroform interface and show high desorption energy. AuNPs clusters assembled by CB[7] are more stable at the interface than un-aggregated single AuNPs, due to higher Helmholtz energy change. Quantitative SERS sensing was carried out on wet and dried AuNPs interfacial arrays, both of which showing a LOD down to nM scale. Furthermore, microdroplet interfaces were used as the gold nanoparticle array templet for SERS sensing, which provide huge potential for its applications in microfluidic SERS sensing. SERS sensing of analytes from multiple phases were also analysed in this chapter to further widen its application scenarios. This method provides a versatile protocol for direct SERS sensing of various of analytes.

In chapter 5, a number of fundamental problems related to droplet-based microfluidic SERS sensing were discussed. AuNPs aggregated by CB[n] were generated in microdroplets as SERS substrates, which could be used for chemical sensing in a high throughput way. The AuNPs aggregating process has been analysed systematically by dark field and bright field microscopy. SERS in microdroplets has been further explored. Methyl viologen, as a SERS marker, was tested in flowing microdroplets when the AuNPs are in high concentration. The position of aggregates in microdroplets has been explored based on the images, videos and spectra. In flowing microdroplets (d = 50 μm), the aggregates were shown to be moving in a half circulating movement on the confocal plane which is 12 μm below droplet sphere centre. The positioning of aggregates can help when detecting SERS signals from aggregates, helping to get the strongest spectrum of analytes. Then the inverse relationship between signal of MV and oil was observed by SERS scanning online in flowing droplets, when the integration time is as short as 0.01 to 0.05s.

6.2 Future work

6.2.1 NT SERS sensing in body fluids

In chapter 2&3, the dopamine SERS sensing LOD is lower than 1 μM and other NTs are around 1 μM. However, these NTs were all analysed in pure water solution which makes the detecting environments much less complicated than real human body fluids. To further explore this sensing method for body fluids, artificial urine and artificial cerebrospinal fluid (ACSF) were introduced for dopamine SERS sensing with CB[7]. The results in Figure 6.1 and 6.2 show that the DA LOD could reach 1 μM in artificial urine and 0.1 μM in ACSF by PCA analysis. However, the nature of DA SERS sensing within these complicated environments is not clearly understood. Future work could focus on the understanding of interactions among the main contents in urine or ACSF while SERS sensing with AuNPs aggregates. Improving the LOD for different NTs in body fluids could be a further research aim on the basis of above fundamental principles.

Figure 6.1 a) SERS spectra of DA in artificial urine. 294 μL of 60 nm AuNPs was firstly mixed with 6 μL of 1 mM CB[7] solution in plate well holder. 15 μL of DA sample dissolved in 15 μL artificial urine in different concentrations were then added to the AuNPs-CB[7] mixture. SERS were measured with 1 s integration time with 798 nm trigger laser under 5X lens. b) PC1 scores vs DA concentrations in urine after PCA analysis.
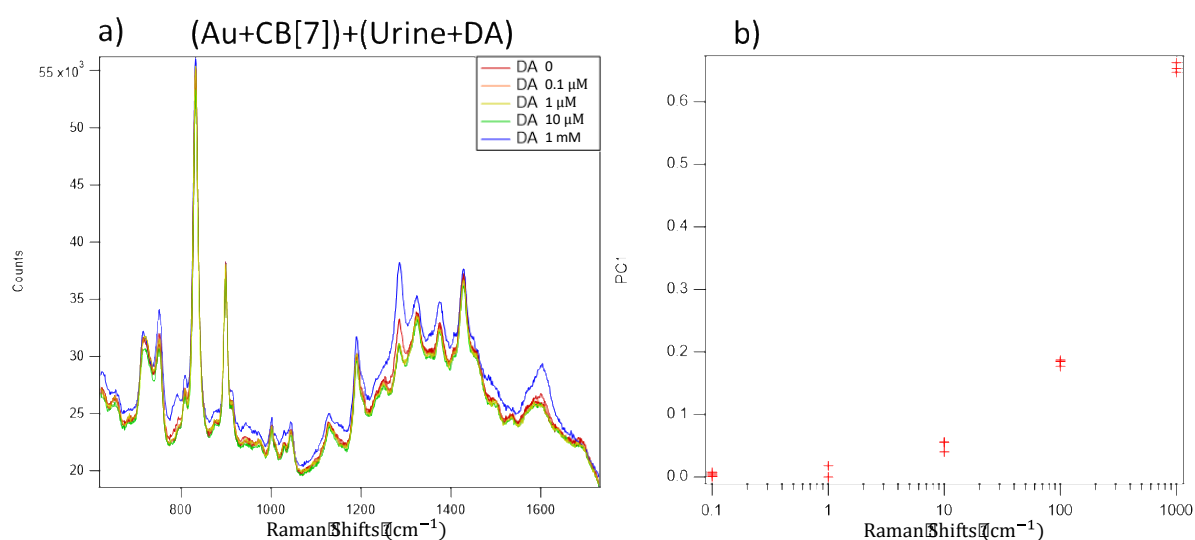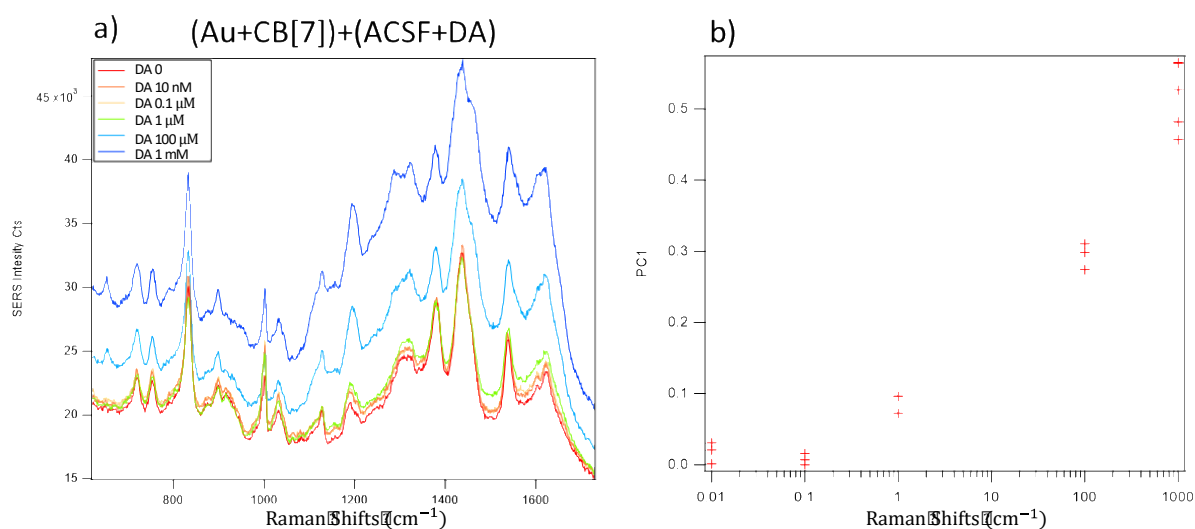
Figure 6.2 a) SERS spectra of DA in ACSF. 294 μL of 60 nm AuNPs was firstly mixed with 6 μL of 1 mM CB[7] solution in plate well holder. 15 μL DA sample dissolved in 15 μL ACSF in different concentrations were then added to the AuNPs-CB[7] mixture. SERS were measured with 1 s integration time with 798 nm trigger laser under 5X lens. b) PC1 scores vs DA concentrations in ACSF after PCA analysis.

6.2.2 SERS sensing of algal metabolite ethanol in microdroplets

The results of chapter 5 are potentially helpful for building an effective microdroplets high-throughput SERS sorting system in the future. Traditionally, fluorescent spectroscopy was used for cell soring in microfluidics.[175] SERS could be an alternative technology which can bring many advantages such as getting rid of labelling procedures and reducing the complexity of sorting. Microalgae, which have ability to produce high value products, such as ethanol, could be an application target of this system, since microalgae can be cultured in microdroplets.[187] In order to optimise the microalgae aquaculture, it is crucial to screen the most productive cell species effectively and microdroplet based SERS screening platform could be an efficient label free sensing technique to achieve this.

Using the similar protocol as NTs in Chapters 2&3, ethanol, one of algae's metabolites, was preliminarily analysed in bulk solution by SERS using CB[n] as the host-guest molecule. Scherman and co-workers, have described that among CB[n] family members, CB[6] has a weak binding constant to ethanol (lg1.5 - lg1.9) detected by ITC, while CB[5], CB[7] and CB[8] have not been reported any binding effects with ethanol[188]. Therefore, it was decided to examine AuNPs-CB[6] system with low concentrations of ethanol. The following section will show some fundamental research results about ethanol SERS sensing, while there are still a number of challenges remaining for the future research in order to achieve the final goal of algae cell screening by microfluidic droplets SERS sensing.

Firstly, the Raman spectrum of pure ethanol was analysed, as well as the SERS spectrum of AuNPs-ethanol system, as shown in Figure 6.3. The Raman spectrum of pure ethanol, shows 4 strong characteristic peaks at 876, 1043, 1082 and 1453 cm^{-1}. Different concentrations of ethanol in water were tested, from 0.01 vol% to 10 vol%, as shown in Figure 6.3b. The four characteristic Raman peaks can be clearly found when the ethanol concentration is over 2.5 vol%. A linear relationship between the 876 cm^{-1} peak intensity and ethanol concentration (above 1 vol%) can be found as shown in Figure 6.3c.

When 80 vol% of 60 nm AuNPs solution was added to ethanol solutions, same concentration series was carried out as shown in Figure 6.3d. The same characteristics peaks of ethanol were observed and the same LOD can be found as 2.5 vol%. The 876 cm^{-1} peak intensity is linear to ethanol concentration when it is above 1 vol%, which shows that adding AuNPs is not able to help increase the ethanol detection limit, nor enhance the ethanol Raman intensity significantly, even though a small amount of AuNPs aggregates appeared in the samples since the change of AuNPs environment.

The significant increasing of peak 1000 cm^{-1} intensity (signal from the polystyrene holder) as AuNPs were added in, was due to the change of the contact angle among aqueous solvent, AuNPs and the polypropylene holder. When the ethanol concentration is high (above 2.5 vol%), AuNPs tend to stay at the interface between the liquid and the solid holder to keep the lowest surface energy. Due to the AuNPs attached to the holder, when the sample is illuminated by the 875 nm laser, a strong SERS signal of the polypropylene at 1000 cm^{-1} can be detected. While when there is no AuNPs involved, only a weak signal of Raman at 1000 cm^{-1} can be detected.
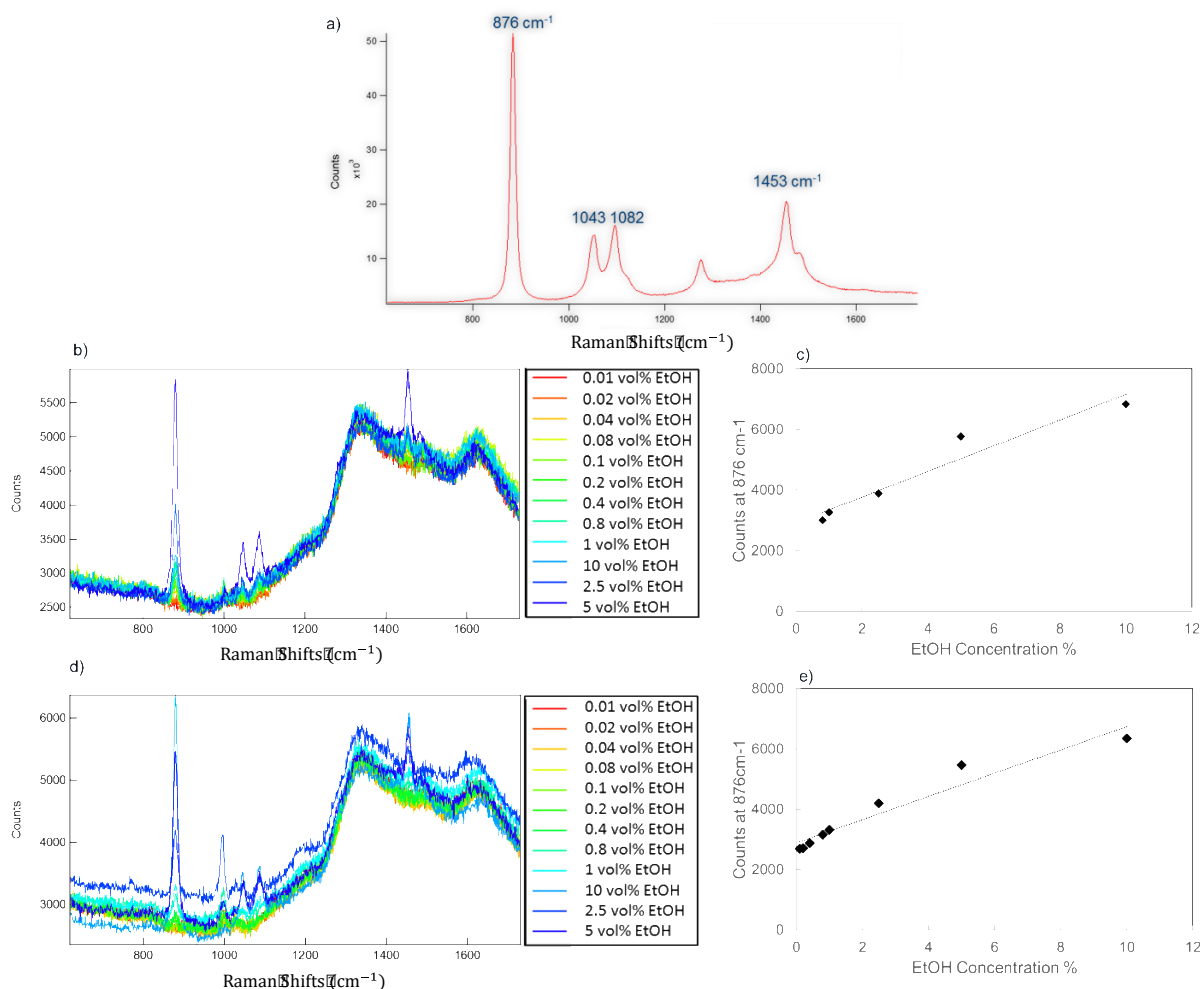
Figure 6.3 a) Raman spectrum of 100% ethanol. b)&d) Raman spectra concentration series of ethanol in aqueous solution with (b) and without (d) AuNPs. c)&e) Relationship of 876 cm^{-1} intensities with ethanol concentrations without (c) and with (e) AuNPs.

Introducing binding molecule CB[6] is an option to improve the detecting limit, which can aggregate AuNPs and locate ethanol molecules to the aggregates hotspots. PCA was used to process the SERS data (Figure 6.4). By correlating to the ethanol Raman spectrum (Figure 6.3a), the CB[6] SERS spectrum (Figure 6.4b) with components PC0 and PC1 (Figure 6.4a), the following conclusion can be drawn: PC0 shows similar spectrum as CB[6], so PC0 mostly attributes to CB[6]. PC1 is similar to the Raman spectrum of pure ethanol, so PC1 attributes to the adding of ethanol. For the quantitative discussion, the relationship of PCs scores with ethanol concentrations are shown in Figure 6.4c and d. The PC0 scores were kept constant as the ethanol concentration increases. PC1 shows a linear relationship when the ethanol concentration is above 1 vol%, and has a low-slope linear relationship when the ethanol concentration is below 1 vol%. By comparing this trend with that of the ethanol Raman spectra (Figure 6.4c and e), it can be seen that the spectra show the same trend at the high concentration

117

region (over 1 vol%) and this suggests that the PC1 is dominated by the ethanol Raman spectrum. With CB[6] as the binding molecule, even with a lower ethanol concentration (below 1 vol%), PC1 increases as the ethanol concentration increases and the detection limit can go down to 0.001 vol%. Therefore, adding CB[6] is helpful for trace ethanol detection. However, since the slope at low concentration is low, it is possible that the background noise could overlap with the ethanol signals when the detection environment is complex, so that quantitative detection can become difficult. Even though this system provides a possibility for quantitative trace ethanol detection, the requirement for the operating environment is demanding.
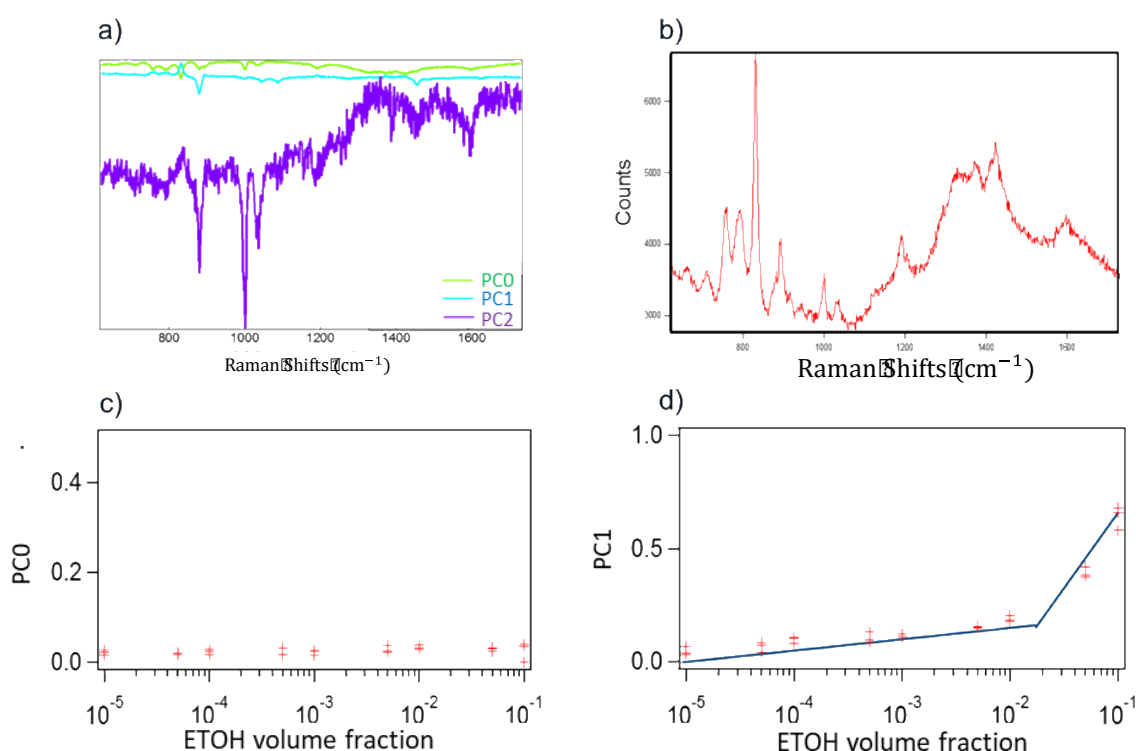
Figure 6.4 a) PC0, PC1 and PC2 of AuNPs (60 nm, $= 2.6 \times 10^{10}/ml$)-CB[6]-ethanol system. 250 µL of AuNPs solution was firstly mixed with 20 Ml of CB[6] solution (1 mM). After waiting for 10 min, different concentration of ethanol solutions in water (from 0 to 10 vol%) were added to the mixture. SERS spectra were obtained with Renishaw. b) CB[6] SERS. c,d) PC0 and PC1 scores vs. ethanol concentrations.

All the above experiments were implemented in bulk ethanol solution rather than in the microfluidic channel. There are still many challenges in order to detect trace ethanol in flowing microfluidic droplets quantitatively and even more challenges in order to detect the ethanol produced by microalgae cells encapsulated by flowing droplets. Apart from the challenges brought by the unmatched SERS integration time and the droplet flowing time, the challenges from the background

noises, the system complexity and the SERS signal reproducibility all can provide interesting and meaningful research topics to future researchers.

Chapter 7 Experimental

7.1 General

7.1.1 Materials

All of the materials mentioned in this thesis were used as purchased unless specified otherwise. Sodium chloride (NaCl), iron(III) nitrate nonahydrate (Fe(NO$_3$)$_3 \cdot$ 9H$_2$O), dopamine hydrochloride (C$_8$H$_{11}$NO$_2 \cdot$ HCl), epinephrine hydrochloride (C$_9$H$_{13}$NO$_3 \cdot$ HCl), norepinephrine hydrochloride (C$_8$H$_{11}$NO$_3 \cdot$ HCl), dihydroxyphenylalanine (DOPA, C$_9$H$_{11}$NO$_4$), serotonin hydrochloride (C$_{10}$H$_{12}$N$_2$O $\cdot$ HCl), artificial urine, ACSF, chloroform (CHCl$_3$), ethanol (EtOH), methyl viologen dichloride (MV), methylene blue (MB), hydrochloric acid (HCl) and sodium hydroxide (NaOH) were purchased from Sigma Aldrich and used without further purification. Batches of 60 nm AuNPs (100 mL) were purchased from BBI Solutions. Cucurbituril's (CB[n]) were supplied from Professor Oren Sherman's group in the Yusuf Hamied Department of Chemistry, University of Cambridge. Trichloro(1H,1H,2H,2H-perfluorooctyl) silane was purchased from Alfa Aesar. Silicon Elastomer base polydimethylsiloxane(PDMS) and curing agent were purchased from Dow Corning. 60 nm ($C = 2.6 \times 10^{10}/ml$) and 80 nm ($C = 1.1 \times 10^{10}/ml$) gold nanoparticles in aqueous solvent were purchased from British Biocell International.

7.1.2 Principal component analysis (PCA)

Previous research in our group has proven that by using PCA, 0.1% methanol in water can be detected by AuNPs-CB[5] aggregates.[81] In this thesis, principal component analysis (PCA) is widely applied to analyse the concentration series data for both Raman (Section 2.2) and SERS (Section 2.4, 2.5 and 2.6) spectra. Herein, the data of dopamine SERS spectra with AuNPs-CB[7] complex (Figure 2.16 a,c&e in section 2.4) will be used to demonstrate how PCA works.

In Figure 2.16a, as higher concentration of DA was added, new peaks arise from some form of interaction with the CB[7]–AuNPs constructs. Quantifying such effects has proven difficult as SERS spectra suffer from inherent background fluctuations, preventing simple comparisons among peak intensities. By using PCA we can accurately identify and quantify the individual analyte components and correlate SERS intensities with analyte concentrations to extract new information. PCA expresses data in a new basis set of mathematically orthogonal components in order of decreasing variability, with the aim of detecting trends in noisy, variable data such as SERS spectra.[81] This is particularly useful when we scan the concentration *m* of one analyte. In the case of this series of spectra, each component consists of an 'eigenspectrum' *Ei(v)* (a set of spectral components which change together)

and a weight c_i (often known as a PCA 'score') which gives the contribution of its associated Eigen spectrum to the measured spectrum. The contribution y_i of a single component to the full spectrum at concentration *m* is then

$$y_i(m) = c_i(m)E_i \qquad (1)$$

Combining all the contributions yields the counts at each wavelength, reconstructing the measured spectrum

$$y_{tot}(\nu) = \sum_{i=1}^{N} c_i E_i(\nu) \qquad (2)$$

where y_{tot} is the SERS emission at wavenumber ν. Igor was used to program the raw SERS spectra data and procedures were provided by Dr Bart de Nijs from Physics department.

In Figure 2.16, the Eigen spectrum of the first component obtained using PCA (PC0, E_1) closely resembles the spectra of sample without analytes (Figure 2.16c). The eigenspectrum of the second major component (PC1, E_2) is attributed to DA since a steady increase in its corresponding scores is observed with the addition of analyte (Figure 2.16e).

7.1.3 Optical Microscopy and Spectroscopy

Various optical setups were used in the research. Au-CB aggregations were analyzed using an optical microscope (Olympus BX51 upright or Olympus IX71 inverted, Figure7.1), by both bright field and dark field microscopy. 5X, 20X and 50X MPLFLN-BD Olympus objectives were applied for imaging and spectroscopy. Infiniti cameras were coupled to the microscopes and the software Infinity Capture was used for image analysis. An Ocean Optics QE65000 spectrometer (300 – 1000 nm) was connected to optical microscopes by optical fibers (Ocean Optics QP600-2-VIS-BX), so that the scattering spectra could be detected from a confined optical spot (d = 40 μm) from samples. Tungsten-halogen lamps were used as the light source for reflective dark field scattering spectra and a white reflectance standard was used as a reference for spectra normalization.

For the flowing microdroplets observation and analysis, a high-speed Phantom fast camera (V72, Vision Research) was used with transmission illumination. An Ocean Optics DH-2000-BAL spectrometer was used to perform bulk solution spectroscopy with UV-NIR transmission light source. Deionized water was used as a reference for spectra normalization in polystyrene cuvettes.

Measurements of Raman scattering used an inVia™ confocal Raman microscope (Figure 7.2) using 5X, 20X and 50X objectives. The 785 nm laser was first filtered by a clean-up filter, followed by reflection at a dichroic beam splitter and then focusing though the objective in order to excite from above a

target sample, which was placed on a motorised 3-axis microscope stage. Simultaneously, the scattering Raman signal from the excitation spot was collected through the same light path travelling back through the objective, passing through the dichroic beam splitter and a high-pass filter, and the signal dispersed by a grating and focussed on a TE-cooled back-thinned charge-coupled device (CCD) sensor collecting spectra on computer for post-analysis. The optimised depth below the surface of the liquid sample for laser excitation was determined by finding the maximum strength of the Raman signal by automated z-axis scanning.

For liquid sample SERS measuring, 5X Nikon lens with 0.2 NA was normally used and full laser power (131.6 mW) was used. A black plastic multi-well plate (Figure 7.3) or a cuvette was used as container for analytes, and the acquisition time was normally 1s. For SERS in in-situ microdroplets, acquisition time was normally 10 seconds. For solid samples, 20X or 50X lenses were utilized with lower laser power (less than 5 mW) in order to avoid sample 'burning' by strong laser energy.

Figure 7.1 Olympus IX71 inverted and injection pumps

Figure 7.2 Renishow InVia confocal Raman microscope.

Figure 7.3 Multi-well plate used as liquid SERS sample container.

7.1.4 AuNPs-CB[7] aggregates formation in solution

1 mL citrate-stabilized AuNPs (60nm) was mixed with 100 µL of 1 mM CB[7] provided by the Sherman group. The CB[7] solution was bubbled with nitrogen for 30 min. Sample mixtures were prepared by mixing AuNPs solution with other host guest molecule solutions or NaCl solution in 1mL quartz cuvettes. Extinction spectra were obtained with 1000 ms interval time and 3 ms integration time. All the extinction data were normalized to a white background reference.

7.2 Two protocols of PreNP and PostNP

PreNP: 2 μL of 100 mM $Fe(NO_3)_3 \cdot 9H_2O$ was first pre-incubated with 1998 μL of 0.288 mM 60 nm AuNPs for 10 min to form complexes of Fe(III)and citrate on the surface of AuNPs in an Eppendorf tube. 250 μL of these Fe(III)-coated AuNPs was aggregated with 50 μL of saturated NaCl for 5 min in a black polypropylene 96 well microplate (Greiner Bio-One Ltd). Subsequently, one or mixed types of NTs in water was pipetted into the well and mixed thoroughly and then left for 10 min. Finally, 23.7 mW of 785 nm laser was loosely focused at an optimised depth below the liquid surface in the well and the acquisition of SERS was integrated for 10 sec.

PostNP: Similarly, 10 μL of 45 mM $Fe(NO_3)_3 \cdot 9H_2O$ was pre-incubated with 10 μL of NTs and 980 μL DI water for 10 min to form complexes of Fe(III)and NTs in an Eppendorf tube. 250 μL of 0.288 mM 60 nm AuNPs was aggregated with 50 μL of saturated NaCl for 5 min in a well microplate. Afterwards, the complex of Fe(III) and NTs was pipetted into the well and mixed thoroughly, and the sample solution remained undisturbed for 5 min. Consequently, 23.7 mW of 785 nm laser was used to excite the solution at an optimised focusing depth and SERS was collected for 10 seconds.

7.3 Characterisation of Fe(III)-DA complexes in solution at various pH

On the condition of Fe(III)/dopamine mole ratio as 1/6, pH of the Fe(III)-dopamine mixture (2 mL) was tuned from 3.0 to 12.1 by gradually adding 1 μL of KOH (1 M). Then 1 μL of HCl (0.2 M) was gradually added to tune down the pH from 12.2 to 2.8.

7.4 Water/chloroform interfacial Au arrays by NaCl aggregated AuNPs clusters.

Saturated NaCl solution was made by mixing an excess of salt into distilled water. 1 ml water solution of 60 nm Au nanoparticles from BBI coated with citrate were firstly mixed with 1 μl of saturated NaCl in a Teflon tube (2 ml). After the colour of the solution turned to purple from red, 0.5 ml of pure ethanol was added to the Teflon tube. After mixing by shaking, 0.5ml of chloroform was added.

7.5 SERS measured on the surface of the wet AuNPs film at water/chloroform interface

Analytes (DA, MV or MB) were added after the AuNPs arrays were formed. For SERS measuring, 5X Nikon lens with 0.20 NA was used with Renishaw InVia confocal Raman microscope. Each SERS measurement was taken with 785 nm laser with 131.6 mW laser power and 1s integration time. Apart from adjusting the x-y-z stage, the Au film horizontal level in the Teflon tube can be tuned by removing the volume of top water phase and adding the volume of bottom chloroform phase.

To carry out a systematic concentration series SERS sensing of dopamine, a set of dopamine solution samples of different concentrations (0, 1, 5, 10, 50, 100, 1000, 10000, 100000, 1000000 nM) were firstly prepared. 1 µL of each sample was added in the Teflon tube for measurements. Each SERS data was obtained by taking the average of 3 measurements on the same spot for each dopamine concentration.

7.6 Tilted SEM images of AuNPs arrays

After carefully removal of most of the bulk chloroform with syringe, the remained drop of chloroform surrounded by AuNPs film at the bottom of water phase was then taken out by a hydrophobic plastic pipet and dropped on a clean smooth gold substrate surface. After 24 h, the Au nanoparticles film was dried out. The gold substrate, along with the dried Au nanoparticles film, was cut by a silicon knife carefully through the middle of the dried arrays, in order to let the cross section of the film be exposed and detected by SEM. The gold substrate holding the dried film was then place on tilted SEM holders (45° and 75°) and the images were taken from a titled direction of the sample's cross section by SEM (FEI FEG XL30).

Smooth gold substrates are prepared by e-beam evaporation of 100 nm gold layers onto a clean silicon wafer (Silicon wafers are purchased from SiMat). This is then heated to 60 °C, and small pieces of silicon glued to it and then cured before being peeled off to reveal a ultra-smooth gold surface.

7.7 Microfluidics chips fabrication

AutoCAD 2010 (Autodest Inc.) was used to design the device and Microlithography was used for the dark-field mask printing. SU-8 2025 was spin-coated on a silicon wafer and then after baking, UV light was used on the wafer for the initiation of cross-linking of SU-8. After post-baking, propylene glycol monomethyl ether acetate was used to remove the non-cross linked SU-8 and then the designed masters were ready for next procedures. The above masters for the microfluidic chips were provided by Dr Ziyi Yu from the Abell research group, Yusuf Hamied Department of Chemistry, University of Cambridge.

The microfluidic device was produced via standard soft lithography by pouring poly- (dimethylsiloxane) (PDMS, 20 g) along with a crosslinker (Sylgard 184 elastomer kit, Dow Corning, pre-polymer : crosslinker = 10 : 1 by weight) onto a silicon wafer patterned with SU-8 photoresist.[189] It was then placed in vacuum for half an hour to remove dissolved gas. The PDMS was allowed to solidify at 90 ∘C for 12 h before being peeled off, after which holes punched for inlets and outlets using a 1 mm diameter biopsy punch. The enclosed microfluidic channels were formed by attaching the moulded PDMS replica onto a clean glass slide after exposure to oxygen plasma for 10 s in a Femto plasma

cleaner. To ensure permanent bonding, the complete device was baked overnight at 110 °C. The inner surface of the microchannels was hydrophobic modified by flushing 0.5 vol% trichloro(1H,1H,2H,2H-perfluorooctyl) silane in FC40 through the channels. The channels were then dried in oven for over 20 min at 75 °C. Plastic tubes (PORTEX, polyethene 1.09 mm OD), which were connected to 1 mL syringes (NORM-JECT), were used to inject liquids into microchips by pumps (Harvard Apparatus: PHD 2000; New Era: NE-4002x, NE-1000). The microchannels could be fabricated to various shapes and length, to satisfy the requirement of inlets orders.

7.8 UV-Vis extinction spectra

Extinction spectroscopy was performed on millilitre scale samples in standard UV-cuvettes with light path of 10 mm (volume 1.5–3 mL, Sigma-Aldrich) filled with a liquid sample, fixed in a cuvette holder. The extinction is defined by the attenuation of the incident light, I_0, as:

$E(\lambda) = \log(I_0(\lambda)/I(\lambda))$

where E is the extinction and I is the transmitted intensity.

7.9 AuNPs arrays on the droplet interface observed horizontally

The droplets flowing from the outlet microfluidic channel were collected in a 1ml quartz cuvette filled with chloroform. Most of the droplets sink to the bottom of the cuvette and some attach to the side walls. The droplet shown in Figure 4.11a was the one attached on side wall which can be observed horizontally without interfere from other droplets. The cuvette was then put on the stage as in Figure7.2. The observing light path was adjusted by 90° with a 5X lens, so that the image can be taken from a horizontal direction.

References

1. Elmqvist Rune. Measuring instrument of the recording type. 2566443 (1951).

2. Le, H. P. Progress and trends in ink-jet printing technology. *J. Imaging Sci. Technol.* **42**, 49–62 (1998).

3. Guo, W., Tang, L., Zhou, B. & Fung, Y. Fundamental studies of rapidly fabricated on-chip passive micromixer for modular microfluidics. *Micromachines* **12**, 1–16 (2021).

4. Arockiam, S., Cheng, Y. H., Armenante, P. M. & Basuray, S. Experimental determination and computational prediction of the mixing efficiency of a simple, continuous, serpentine-channel microdevice. *Chem. Eng. Res. Des.* **167**, 303–317 (2021).

5. Tiboni, M. *et al.* Microfluidics for nanomedicines manufacturing: An affordable and low-cost 3D printing approach. *Int. J. Pharm.* **599**, 120–129 (2021).

6. Lee, J. J., Berthier, J., Kearney, K. E., Berthier, E. & Theberge, A. B. Open-Channel Capillary Trees and Capillary Pumping. *Langmuir* **36**, 389–394 (2020).

7. Li, C. *et al.* Under oil open-channel microfluidics empowered by exclusive liquid repellency. *Sci. Adv.* **6**, 465–471 (2020).

8. Cui, Z. *et al.* A fishbone-inspired liquid splitter enables directional droplet transportation and spontaneous separation. *J. Mater. Chem. A* 55–63 (2021). doi:10.1039/d1ta00927c

9. Mashaghi, S., Abbaspourrad, A., Weitz, D. A. & van Oijen, A. M. Droplet microfluidics: A tool for biology, chemistry and nanotechnology. *TrAC - Trends in Analytical Chemistry* **82**, 118–125 (2016).

10. Mashaghi, S., Abbaspourrad, A., Weitz, D. A. & van Oijen, A. M. Droplet microfluidics: A tool for biology, chemistry and nanotechnology. *TrAC - Trends in Analytical Chemistry* **82**, 118–125 (2016).

11. Zhu, Z. & Yang, C. J. Hydrogel droplet microfluidics for high-throughput single molecule/cell analysis. *Acc. Chem. Res.* **50**, 22–31 (2017).

12. Song, Y., Hormes, J. & Kumar, C. S. S. R. Microfluidic synthesis of nanomaterials. *Small* **4**, 698–711 (2008).

13. Xu, B. Bin, Zhang, Y. L., Wei, S., Ding, H. & Sun, H. B. On-Chip catalytic microreactors for modern catalysis research. *ChemCatChem* **5**, 2091–2099 (2013).

14.   Herranz-Blanco, B. *et al.* Microfluidic assembly of multistage porous silicon-lipid vesicles for controlled drug release. *Lab Chip* **14**, 1083–1086 (2014).

15.   Velve-Casquillas, G., Le Berre, M., Piel, M. & Tran, P. T. Microfluidic tools for cell biological research. *Nano Today* **5**, 28–47 (2010).

16.   Huebner, A. *et al.* Microdroplets: A sea of applications? *Lab on a Chip* **8**, 1244–1254 (2008).

17.   Zhu, P. & Wang, L. Passive and active droplet generation with microfluidics: a review. *Lab Chip* **17**, 34–75 (2017).

18.   Liu, W. wen & Zhu, Y. "Development and application of analytical detection techniques for droplet-based microfluidics"-A review. *Analytica Chimica Acta* **1113**, 66–84 (2020).

19.   Fornell, A., Liu, Z. & Tenje, M. Optimisation of the droplet split design for high acoustic particle enrichment in droplet microfluidics. *Microelectron. Eng.* **226**, 734–745 (2020).

20.   Rezaei Nejad, H. & Hoorfar, M. Purification of a droplet using negative dielectrophoresis traps in digital microfluidics. *Microfluid. Nanofluidics* **18**, 483–492 (2015).

21.   Sesen, M. & Whyte, G. Image-Based Single Cell Sorting Automation in Droplet Microfluidics. *Sci. Rep.* **10**, 678–682 (2020).

22.   Zhu, Y. & Fang, Q. Analytical detection techniques for droplet microfluidics-A review. *Analytica Chimica Acta* **787**, 24–35 (2013).

23.   Joensson, H. N. & Andersson Svahn, H. Droplet microfluidics-A tool for single-cell analysis. *Angewandte Chemie - International Edition* **51**, 12176–12192 (2012).

24.   Wang, J., Chao, P. H., Hanet, S. & Van Dam, R. M. Performing multi-step chemical reactions in microliter-sized droplets by leveraging a simple passive transport mechanism. *Lab Chip* **17**, 4342–4355 (2017).

25.   Kim, H. S. *et al.* High-throughput droplet microfluidics screening platform for selecting fast-growing and high lipid-producing microalgae from a mutant library. *Plant Direct* **1**, (2017).

26.   Rho, H. S. *et al.* Programmable droplet-based microfluidic serial dilutor. *J. Ind. Eng. Chem.* **91**, 231–239 (2020).

27.   Pompano, R. R., Liu, W., Du, W. & Ismagilov, R. F. Microfluidics using spatially defined arrays of droplets in one, two, and three dimensions. *Annual Review of Analytical Chemistry* **4**, 59–81 (2011).

28.   Zhou, Y., Huang, J., Chen, Z., Wang, Y. & Xu, J. Controlled retention of droplets and the enhancement of mass transfer in microchannel with multi-groove structure. *Chem. Eng. Sci.* **209**, (2019).

29.   Sripadaraja, K., Umesh, G. & Satyanarayan, M. N. Simulation studies on picolitre volume droplets generation and trapping in T-junction microchannels. *SN Appl. Sci.* **2**, 56–67 (2020).

30.   Yang, L., Li, S., Liu, J. & Cheng, J. Fluid mixing in droplet-based microfluidics with T junction and convergent–divergent sinusoidal microchannels. *Electrophoresis* **39**, 512–520 (2018).

31.   Mastiani, M., Seo, S., Riou, B. & Kim, M. High inertial microfluidics for droplet generation in a flow-focusing geometry. *Biomed. Microdevices* **21**, 345–351 (2019).

32.   Peretzki, A. J. & Belder, D. On-chip integration of normal phase high-performance liquid chromatography and droplet microfluidics introducing ethylene glycol as polar continuous phase for the compartmentalization of n-heptane eluents. *J. Chromatogr. A* **1612**, 875–884 (2020).

33.   Thorsen, T., Roberts, R. W., Arnold, F. H. & Quake, S. R. Dynamic pattern formation in a vesicle-generating microfluidic device. *Phys. Rev. Lett.* **86**, 4163–4166 (2001).

34.   Xu, J. H., Luo, G. S., Chen, G. G. & Wang, J. D. Experimental and theoretical approaches on droplet formation from a micrometer screen hole. *J. Memb. Sci.* **266**, 121–131 (2005).

35.   Liu, H. & Crooks, R. M. Highly reproducible chronoamperometric analysis in microdroplets. *Lab Chip* **13**, 1364–1370 (2013).

36.   Gu, S. *et al.* Droplet-based microfluidics for dose-response assay of enzyme inhibitors by electrochemical method. *Anal. Chim. Acta* **796**, 68–74 (2013).

37.   Hatakeyama, T., Chen, D. L. & Ismagilov, R. F. Microgram-scale testing of reaction conditions in solution using nanoliter plugs in microfluidics with detection by MALDI-MS. *J. Am. Chem. Soc.* **128**, 2518–2519 (2006).

38.   Mazutis, L. *et al.* Droplet-based microfluidic systems for high-throughput single DNA molecule isothermal amplification and analysis. *Anal. Chem.* **81**, 4813–4821 (2009).

39.   März, A., Henkel, T., Cialla, D., Schmitt, M. & Popp, J. Droplet formation via flow-through microdevices in Raman and surface enhanced Raman spectroscopy - Concepts and applications. *Lab Chip* **11**, 3584–3592 (2011).

40.   Fleischmann, M., Hendra, P. J. & McQuillan, A. J. Raman spectra of pyridine adsorbed at a silver

electrode. *Chem. Phys. Lett.* **26**, 163–166 (1974).

41. Le Ru, E. C., Blackie, E., Meyer, M. & Etchegoint, P. G. Surface enhanced raman scattering enhancement factors: A comprehensive study. *J. Phys. Chem. C* **111**, 13794–13803 (2007).

42. Nie, S. & Emory, S. R. Probing single molecules and single nanoparticles by surface-enhanced Raman scattering. *Science (80-.).* **275**, 1102–1106 (1997).

43. Gopinath, A., Boriskina, S. V, Reinhard, B. M. & Dal Negro, L. Deterministic aperiodic arrays of metal nanoparticles for surface-enhanced Raman scattering (SERS). *Opt. Express* **17**, 3741–3753 (2009).

44. Ko, H., Singamaneni, S. & Tsukruk, V. V. Nanostructured Surfaces and Assemblies as SERS Media. *Small* **4**, 1576–1599 (2008).

45. Maitani, M. M. *et al.* Study of SERS chemical enhancement factors using buffer layer assisted growth of metal nanoparticles on self-assembled monolayers. *J. Am. Chem. Soc.* **131**, (2009).

46. Moskovits, M. Persistent misconceptions regarding SERS. *Phys. Chem. Chem. Phys.* **15**, 5301–5311 (2013).

47. Langer, J. *et al.* Present and future of surface-enhanced Raman scattering. *ACS Nano* **14**, 28–117 (2020).

48. K Kneipp, M MOSKOVITS, A. h kNEIPP. Surface-Enhanced Raman Scattering: Physics and Applications. *Springer* (2006).

49. Hao, E. & Schatz, G. C. Electromagnetic fields around silver nanoparticles and dimers. *J. Chem. Phys.* **120**, 357–366 (2004).

50. Israelsen, N. D., Hanson, C. & Vargis, E. Nanoparticle properties and synthesis effects on surface-enhanced Raman scattering enhancement factor: An introduction. *Scientific World Journal* **2015**, (2015).

51. Natan, M. J. Concluding remarks: Surface enhanced Raman scattering. in *Faraday Discussions* **132**, 321–328 (2006).

52. Mosier-Boss, P. A. Review of SERS substrates for chemical sensing. *Nanomaterials* **7**, (2017).

53. Wiley, B., Sun, Y., Mayers, B. & Xia, Y. Shape-controlled synthesis of metal nanostructures: The case of silver. *Chemistry - A European Journal* **11**, 454–463 (2005).

54. Tian, F., Bonnier, F., Casey, A., Shanahan, A. E. & Byrne, H. J. Surface enhanced Raman

scattering with gold nanoparticles: Effect of particle shape. *Anal. Methods* **6**, 9116–9123 (2014).

55. Benz, F. *et al.* SERS of Individual Nanoparticles on a Mirror: Size Does Matter, but so Does Shape. *J. Phys. Chem. Lett.* **7**, (2016).

56. Cowart, D. A., Guida, S. M., Ismat Shah, S. & Marsh, A. G. Effects of Ag nanoparticles on survival and oxygen consumption of zebra fish embryos, Danio rerio. *J. Environ. Sci. Heal. - Part A Toxic/Hazardous Subst. Environ. Eng.* **46**, 1122–1128 (2011).

57. Jimenez De Aberasturi, D. *et al.* Surface Enhanced Raman Scattering Encoded Gold Nanostars for Multiplexed Cell Discrimination. *Chem. Mater.* **28**, 6779–6790 (2016).

58. Péron, O., Rinnert, E., Lehaitre, M., Crassous, P. & Compère, C. Detection of polycyclic aromatic hydrocarbon (PAH) compounds in artificial sea-water using surface-enhanced Raman scattering (SERS). *Talanta* **79**, 199–204 (2009).

59. Poston, P. E. & Harris, J. M. Stable, dispersible surface-enhanced Raman scattering substrate capable of detecting molecules bound to silica-immobilized ligands. *Appl. Spectrosc.* **64**, 1238–1243 (2010).

60. Fierro-Mercado, P. M. & Hernández-Rivera, S. P. Highly Sensitive Filter Paper Substrate for SERS Trace Explosives Detection. *Int. J. Spectrosc.* **2012**, 1–7 (2012).

61. He, S., Chua, J., Tan, E. K. M. & Kah, J. C. Y. Optimizing the SERS enhancement of a facile gold nanostar immobilized paper-based SERS substrate. *RSC Adv.* **7**, 16264–16272 (2017).

62. Muniz-Miranda, M. *et al.* Nanostructured films of metal particles obtained by laser ablation. *Thin Solid Films* **543**, 118–121 (2013).

63. Walsh, R. J. & Chumanov, G. Silver coated porous alumina as a new substrate for surface-enhanced Raman scattering. *Appl. Spectrosc.* **55**, 1695–1700 (2001).

64. Bryche, J. F. *et al.* Surface enhanced Raman scattering improvement of gold triangular nanoprisms by a gold reflective underlayer for chemical sensing. *Sensors Actuators, B Chem.* **228**, 31–35 (2016).

65. Jahn, M. *et al.* Plasmonic nanostructures for surface enhanced spectroscopic methods. *Analyst* **141**, 756–793 (2016).

66. Wu, D. Y., Li, J. F., Ren, B. & Tian, Z. Q. Electrochemical surface-enhanced Raman spectroscopy of nanostructures. *Chem. Soc. Rev.* **37**, 1025–1041 (2008).

67.   Jubb, A. M., Jiao, Y., Eres, G., Retterer, S. T. & Gu, B. Elevated gold ellipse nanoantenna dimers as sensitive and tunable surface enhanced Raman spectroscopy substrates. *Nanoscale* **8**, 5641–5648 (2016).

68.   Hatab, N. A. *et al.* Free-standing optical gold bowtie nanoantenna with variable gap size for enhanced Raman spectroscopy. *Nano Lett.* **10**, 4952–4955 (2010).

69.   Yue, W. *et al.* Electron-beam lithography of gold nanostructures for surface-enhanced Raman scattering. *J. Micromechanics Microengineering* **22**, 456–459 (2012).

70.   Alvarez-Puebla, R. A. & Liz-Marzán, L. M. Traps and cages for universal SERS detection. *Chem. Soc. Rev.* **41**, 43–51 (2012).

71.   Schlücker, S. Surface-enhanced raman spectroscopy: Concepts and chemical applications. *Angewandte Chemie - International Edition* **53**, 4756–4795 (2014).

72.   Ding, S. Y., You, E. M., Tian, Z. Q. & Moskovits, M. Electromagnetic theories of surface-enhanced Raman spectroscopy. *Chemical Society Reviews* **46**, 4042–4076 (2017).

73.   Bantz, K. C. *et al.* Recent progress in SERS biosensing. *Physical Chemistry Chemical Physics* **13**, 11551–11567 (2011).

74.   Zong, C. *et al.* Surface-Enhanced Raman Spectroscopy for Bioanalysis: Reliability and Challenges. *Chemical Reviews* **118**, 4946–4980 (2018).

75.   Tao, C. A. *et al.* Cucurbit[n]urils as a SERS hot-spot nanocontainer through bridging gold nanoparticles. *Chem. Commun.* **47**, (2011).

76.   Álvarez-Puebla, R. A., Contreras-Cáceres, R., Pastoriza-Santos, I., Pérez-Juste, J. & Liz-Marzán, L. M. Au@pNIPAM colloids as molecular traps for surface-enhanced, spectroscopic, ultra-sensitive analysis. *Angew. Chemie - Int. Ed.* **48**, 138–143 (2009).

77.   Contreras-Cáceres, R. *et al.* Multifunctional microgel magnetic/optical traps for SERS ultradetection. *Langmuir* **27**, 4520–4525 (2011).

78.   Mahajan, S. *et al.* Raman and SERS spectroscopy of cucurbit[n]urils. *Phys. Chem. Chem. Phys.* **12**, (2010).

79.   Jones, S. T. *et al.* Gold nanorods with sub-nanometer separation using cucurbit[n]uril for SERS applications. *Small* **10**, 4298–4303 (2014).

80.   Kasera, S., Biedermann, F., Baumberg, J. J., Scherman, O. A. & Mahajan, S. Quantitative SERS

using the sequestration of small molecules inside precise plasmonic nanoconstructs. *Nano Lett.* **12**, 5924–5928 (2012).

81. De Nijs, B. *et al.* Smart supramolecular sensing with cucurbit[: N] urils: Probing hydrogen bonding with SERS. *Faraday Discuss.* **205**, 505–515 (2017).

82. Wang, J., Liu, K., Jin, S., Jiang, L. & Liang, P. A Review of Chinese Raman Spectroscopy Research Over the Past Twenty Years. *Appl. Spectrosc.* **74**, (2020).

83. Xie, Y. *et al.* Sensing of polycyclic aromatic hydrocarbons with cyclodextrin inclusion complexes on silver nanoparticles by surface-enhanced Raman scattering. *Analyst* **135**, 1389–1394 (2010).

84. Strickland, A. D. & Batt, C. A. Detection of carbendazim by surface-enhanced raman scattering using cyclodextrin inclusion complexes on gold nanorods. *Anal. Chem.* **81**, 2895–2903 (2009).

85. Lagona, J., Mukhopadhyay, P., Chakrabarti, S. & Isaacs, L. The cucurbit[n]uril family. *Angewandte Chemie - International Edition* **44**, 4844–4870 (2005).

86. Del Puerto, E., Sánchez-Cortés, S., García-Ramos, J. V. & Domingo, C. Solution SERS of an insoluble synthetic organic pigment-quinacridone quinone-employing calixarenes as dispersive cavitands. *Chem. Commun.* **47**, 1854–1856 (2011).

87. Grzelczak, M.; Vermant, J.; Furst, E. M.; Liz-Marzán, L. M. Directed Self-Assembly of Nanoparticles.pdf. 4, 3591–3605 (2010). doi:https://doi.org/10.1021/nn100869j

88. Skalski, J. H. & Kuch, J. Polish thread in the history of circulatory physiology. *Journal of Physiology and Pharmacology* **57**, 5–41 (2006).

89. Holtz, P. Dopadecarboxylase. *Naturwissenschaften* **27**, 724–725 (1939).

90. Niyonambaza, S. D. *et al.* A Review of neurotransmitters sensing methods for neuro-engineering research. *Applied Sciences (Switzerland)* **9**, (2019).

91. Wise, R. A. Dopamine, learning and motivation. *Nature Reviews Neuroscience* **5**, 483–494 (2004).

92. Meisenzahl, E. M., Schmitt, G. J., Scheuerecker, J. & Möller, H. J. The role of dopamine for the pathophysiology of schizophrenia. *International Review of Psychiatry* **19**, 337–345 (2007).

93. A. Kato, T. *et al.* Neurotransmitters, Psychotropic Drugs and Microglia: Clinical Implications for Psychiatry. *Curr. Med. Chem.* **20**, 331–344 (2013).

94. Lucki, I. The spectrum of behaviors influenced by serotonin. *Biol. Psychiatry* **44**, 151–162 (1998).

95.   Sembulingam, P. *Essentials of Medical Physiology*. *Essentials of Medical Physiology* (2012). doi:10.5005/jp/books/11696

96.   Drevets, W. C. *et al.* PET measures of amphetamine-induced dopamine release in ventral versus dorsal striatum. *Neuropsychopharmacology* **21**, 694–709 (1999).

97.   Laruelle, M. *et al.* SPECT imaging of striatal dopamine release after amphetamine challenge. *J. Nucl. Med.* **36**, 1182–1190 (1995).

98.   Keithley, R. B. *et al.* Higher sensitivity dopamine measurements with faster-scan cyclic voltammetry. *Anal. Chem.* **83**, 3563–3571 (2011).

99.   Bruns, D. Detection of transmitter release with carbon fiber electrodes. *Methods* **33**, 312–321 (2004).

100.   Snyder, S. H. & Kim, P. M. D-amino acids as putative neurotransmitters: Focus on D-serine. *Neurochem. Res.* **25**, 553–560 (2000).

101.   Zhao, X. E. & Suo, Y. R. Simultaneous determination of monoamine and amino acid neurotransmitters in rat endbrain tissues by pre-column derivatization with high-performance liquid chromatographic fluorescence detection and mass spectrometric identification. *Talanta* **76**, 690–697 (2008).

102.   Nirogi, R., Mudigonda, K., Kandikere, V. & Ponnamaneni, R. Quantification of acetylcholine, an essential neurotransmitter, in brain microdialysis samples by liquid chromatography mass spectrometry. *Biomedical Chromatography* **24**, 39–48 (2010).

103.   Schmerberg, C. M. & Li, L. Mass spectrometric detection of neuropeptides using affinity-enhanced microdialysis with antibody-coated magnetic nanoparticles. *Anal. Chem.* **85**, 915–922 (2013).

104.   Zestos, A. G. & Kennedy, R. T. Microdialysis Coupled with LC-MS/MS for In Vivo Neurochemical Monitoring. *AAPS J.* **19**, 1284–1293 (2017).

105.   Kennedy, R. T., Watson, C. J., Haskins, W. E., Powell, D. H. & Strecker, R. E. In vivo neurochemical monitoring by microdialysis and capillary separations. *Current Opinion in Chemical Biology* **6**, 659–665 (2002).

106.   Ceccarini, J. *et al.* Optimized in vivo detection of dopamine release using18F- fallypride PET. *J. Nucl. Med.* **53**, 1565–1572 (2012).

107.   Phillips, P. E. M. & Wightman, R. M. Critical guidelines for validation of the selectivity of in-vivo

chemical microsensors. in *TrAC - Trends in Analytical Chemistry* **22**, 509–514 (2003).

108. Njagi, J., Chernov, M. M., Leiter, J. C. & Andreescu, S. Amperometric detection of dopamine in vivo with an enzyme based carbon fiber microbiosensor. *Anal. Chem.* **82**, 989–996 (2010).

109. Nakatsuka, N. *et al.* Aptamer–field-effect transistors overcome Debye length limitations for small-molecule sensing. *Science (80-.).* **362**, 319–324 (2018).

110. Le Ru, E. C. & Etchegoin, P. G. Single-molecule surface-enhanced raman spectroscopy. *Annual Review of Physical Chemistry* **63**, 65–87 (2012).

111. Nguyen, B. H., Nguyen, V. H. & Tran, H. N. Rich variety of substrates for surface enhanced raman spectroscopy. *Advances in Natural Sciences: Nanoscience and Nanotechnology* **7**, (2016).

112. Kyba, E. P. *et al.* Host-Guest Complexation. 1. Concept and Illustration. *J. Am. Chem. Soc.* **99**, 2564–2571 (1977).

113. W.A.Freeman, W.L.Mock, N. Y. S. Cucurbituril. *JACS* **103**, 7367–7368 (1981).

114. Behrend, R., Meyer, E. & Rusche, F. I. Ueber Condensationsproducte aus Glycoluril und Formaldehyd. *Justus Liebigs Ann. Chem.* **339**, 1–37 (1905).

115. Day, A. I. *et al.* A cucurbituril-based gyroscane: A new supramolecular form. *Angew. Chemie - Int. Ed.* **41**, 275–277 (2002).

116. Liu, S. *et al.* The cucurbit[n]uril family: Prime components for self-sorting systems. *J. Am. Chem. Soc.* **127**, 15959–15967 (2005).

117. Day, A., Arnold, A. P., Blanch, R. J. & Snushall, B. Controlling factors in the synthesis of cucurbituril and its homologues. *J. Org. Chem.* **66**, 8094–8100 (2001).

118. Zhou, Y. *et al.* Host properties of cucurbit [7] uril: Fluorescence enhancement of acridine orange. *J. Incl. Phenom. Macrocycl. Chem.* **61**, 259–264 (2008).

119. Cheng, X. J. *et al.* Twisted cucurbit[14]uril. *Angew. Chemie - Int. Ed.* **52**, 7252–7255 (2013).

120. Barrow, S. J., Kasera, S., Rowland, M. J., Del Barrio, J. & Scherman, O. A. Cucurbituril-Based Molecular Recognition. *Chemical Reviews* **115**, 12320–12406 (2015).

121. Jason Lagona Pritam Mukhopadhyay Dr. Sriparna Chakrabarti Dr. Lyle Isaacs Prof. Dr. The Cucurbit[n]uril Family. *Angew Chem Int Ed.* **44**, 4844–4870 (2005).

122. Das, D. & Scherman, O. A. Cucurbituril: At the interface of small molecule host-guest chemistry and dynamic aggregates. *Israel Journal of Chemistry* **51**, 537–550 (2011).

123. Lü, J., Lin, J. X., Cao, M. N. & Cao, R. Cucurbituril: A promising organic building block for the design of coordination compounds and beyond. *Coordination Chemistry Reviews* **257**, 1334–1356 (2013).

124. Assaf, K. I. & Nau, W. M. Cucurbiturils: From synthesis to high-affinity binding and catalysis. *Chemical Society Reviews* **44**, 394–418 (2015).

125. Biedermann, F., Uzunova, V. D., Scherman, O. A., Nau, W. M. & De Simone, A. Release of high-energy water as an essential driving force for the high-affinity binding of cucurbit[n]urils. *J. Am. Chem. Soc.* **134**, 15318–15323 (2012).

126. Lee, J. W., Samal, S., Selvapalam, N., Kim, H. J. & Kim, K. Cucurbituril homologues and derivatives: New opportunities in supramolecular chemistry. *Accounts of Chemical Research* **36**, 621–630 (2003).

127. An, Q. *et al.* A general and efficient method to form self-assembled cucurbit[n]uril monolayers on gold surfaces. *Chem. Commun.* 1989–1991 (2008). doi:10.1039/b719927a

128. Salmon, A. R. *et al.* Monitoring Early-Stage Nanoparticle Assembly in Microdroplets by Optical Spectroscopy and SERS. *Small* **12**, 1788–1796 (2016).

129. Taylor, R. W. *et al.* Precise subnanometer plasmonic junctions for SERS within gold nanoparticle assemblies using cucurbit[n]uril 'glue'. *ACS Nano* **5**, 3878–3887 (2011).

130. Lee, N. soo, Hsieh, Y. zung, Paisley, R. F. & Morris, M. D. Surface-Enhanced Raman Spectroscopy of the Catecholamine Neurotransmitters and Related Compounds. *Anal. Chem.* **60**, 442–446 (1988).

131. Kneipp, K., Wang, Y., Dasari, R. R. & Feld, M. S. Near-infrared surface-enhanced Raman scattering (NIR-SERS) of neurotransmitters in colloidal silver solutions. *Spectrochim. Acta Part A Mol. Biomol. Spectrosc.* **51**, 481–487 (1995).

132. Xu, C. *et al.* Dopamine as a robust anchor to immobilize functional molecules on the iron oxide shell of magnetic nanoparticles. *J. Am. Chem. Soc.* **126**, 9938–9939 (2004).

133. Dutta Chowdhury, A. & Doong, R. A. Highly Sensitive and Selective Detection of Nanomolar Ferric Ions Using Dopamine Functionalized Graphene Quantum Dots. *ACS Appl. Mater. Interfaces* **8**, 21002–21010 (2016).

134. Kaya, M. & Volkan, M. New approach for the surface enhanced resonance Raman scattering (SERRS) detection of dopamine at picomolar (pM) levels in the presence of ascorbic acid. *Anal.*

Chem. **84**, 7729–7735 (2012).

135. Li, P. *et al.* Functionalized Acupuncture Needle as Surface-Enhanced Resonance Raman Spectroscopy Sensor for Rapid and Sensitive Detection of Dopamine in Serum and Cerebrospinal Fluid. *Chem. - A Eur. J.* **23**, 14278–14285 (2017).

136. Charkoudian, L. K. & Franz, K. J. Fe(III)-coordinatior properties of neuromelanin components: 5,6-dihydroxyindole and 5,6-dihydroxyindole-2-carboxylic acid. *Inorg. Chem.* **45**, 3657–3664 (2006).

137. Silva, A. M. N., Kong, X., Parkin, M. C., Cammack, R. & Hider, R. C. Iron(iii) citrate speciation in aqueous solution. *Dalt. Trans.* 8616–8625 (2009). doi:10.1039/b910970f

138. Li, Y., Li, J., Shangguan, E. & Li, Q. The effect of acidity, hydrogen bond catalysis and auxiliary electrode reaction on the oxidation peak current for dopamine, uric acid and tryptophan. *Anal. Methods* **7**, 2636–2644 (2015).

139. Shahbakhsh, M., Saravani, H., Hashemzaei, Z. & Narouie, S. Nature inspired poly (dopamine quinone –vanadyl) as new modifier for voltammetric determination of uric acid. *Microchim. Acta* **187**, (2020).

140. Guo, Y. *et al.* Label-free colorimetric detection of cadmium ions in rice samples using gold nanoparticles. *Anal. Chem.* **86**, 8530–8534 (2014).

141. Yang, F. K. & Zhao, B. Adhesion Properties of Self-Polymerized Dopamine Thin Film. *Open Surf. Sci. J.* **3**, 115–122 (2014).

142. Si, B. & Song, E. Recent advances in the detection of neurotransmitters. *Chemosensors* **6**, (2018).

143. O'Neill, H. A. A review on the involvement of catecholamines in animal behaviour. *South African J. Anim. Sci.* **49**, 1–8 (2019).

144. Pan, X. *et al.* Catecholamines in Alzheimer's Disease: A Systematic Review and Meta-Analysis. *Frontiers in Aging Neuroscience* **12**, (2020).

145. Edel, J. B., Kornyshev, A. A. & Urbakh, M. Self-assembly of nanoparticle arrays for use as mirrors, sensors, and antennas. *ACS Nano* **7**, 9526–9532 (2013).

146. Ramsden, W. Separation of solids in the surface-layers of solutions and 'suspensions' - preliminary account. *Proc. R. Soc.* **72**, 156–164 (1903).

147. Pickering, S. U. CXCVI. - Emulsions. *Journal of the Chemical Society, Transactions* **91**, 2001–2021

(1907).

148. Kim, S.-H., Lee, S. Y. & Yang, S.-M. Janus Microspheres for a Highly Flexible and Impregnable Water-Repelling Interface. *Angew. Chemie* **122**, 2589–2592 (2010).

149. Shi, S. & Russell, T. P. Nanoparticle Assembly at Liquid–Liquid Interfaces: From the Nanoscale to Mesoscale. *Advanced Materials* **30**, 122–129 (2018).

150. Finkle, P., Draper, H. D. & Hildebrand, J. H. The theory of emulsification. *J. Am. Chem. Soc.* **45**, 2780–2788 (1923).

151. Pieranski, P. Two-dimensional interfacial colloidal crystals. *Phys. Rev. Lett.* **45**, 569–572 (1980).

152. Binks, B. P. & Lumsdon, S. O. Influence of particle wettability on the type and stability of surfactant-free emulsions. *Langmuir* **16**, 8622–8631 (2000).

153. Lin, Y. *et al.* Nanoparticle assembly at fluid interfaces: Structure and dynamics. *Langmuir* **21**, 191–194 (2005).

154. Lin, Y., Skaff, H., Emrick, T., Dinsmore, A. D. & Russell, T. P. Nanoparticle assembly and transport at liquid-liquid interfaces. *Science (80-.).* **299**, 226–229 (2003).

155. Duan, H., Wang, D., Kurth, D. G. & Möhwald, H. Directing self-assembly of nanoparticles at water/oil interfaces. *Angew. Chemie - Int. Ed.* **43**, 5639–5642 (2004).

156. Yang, P., Sun, W., Hu, S. & Chen, Z. Self-assembly of nanoparticles at interfaces. *Progress in Chemistry* **26**, 1107–1119 (2014).

157. Phan-Quang, G. C., Lee, H. K., Phang, I. Y. & Ling, X. Y. Plasmonic Colloidosomes as Three-Dimensional SERS Platforms with Enhanced Surface Area for Multiphase Sub-Microliter Toxin Sensing. *Angew. Chemie - Int. Ed.* **54**, 9691–9695 (2015).

158. Luo, W. *et al.* Liquid Phase Interfacial Surface-Enhanced Raman Scattering Platform for Ratiometric Detection of MicroRNA 155. *Anal. Chem.* **92**, 15573–15578 (2020).

159. Cecchini, M. P., Turek, V. A., Paget, J., Kornyshev, A. A. & Edel, J. B. Self-Assembled Nanoparticle Arrays for Multiphase Trace Analyte Detection. *Nat. Mater.* **12**, 165–171 (2012).

160. Cecchini, M. P., Turek, V. A., Paget, J., Kornyshev, A. A. & Edel, J. B. Self-assembled nanoparticle arrays for multiphase trace analyte detection. *Nat. Mater.* **12**, 165–171 (2013).

161. Kim, B., Tripp, S. L. & Wei, A. Tuning the Optical Properties of Large Gold Nanoparticle Arrays. **676**, 1–7 (2001).

162. Zhang, K., Ji, J., Li, Y. & Liu, B. Interfacial self-assembled functional nanoparticle array: A facile surface-enhanced raman scattering sensor for specific detection of trace analytes. *Anal. Chem.* **86**, 6660–6665 (2014).

163. Reincke, F., Hickey, S. G., Kegel, W. K. & Vanmaekelbergh, D. Spontaneous Assembly of a Monolayer of Charged Gold Nanocrystals at the Water/Oil Interface. *Angew. Chemie - Int. Ed.* **43**, 458–462 (2004).

164. Reincke, F. *et al.* Electrochemical and topological characterization of gold(111)|oligo(cyclohexylidene)|gold nanocrystal interfaces. *J. Electroanal. Chem.* **522**, 2–10 (2002).

165. Cristobal, G. *et al.* On-line laser Raman spectroscopic probing of droplets engineered in microfluidic devices. *Lab Chip* **6**, 1140–1146 (2006).

166. Sarrazin, F., Salmon, J. B., Talaga, D. & Servant, L. Chemical reaction imaging within microfluidic devices using confocal raman spectroscopy: The case of water and deuterium oxide as a model system. *Anal. Chem.* **80**, 1689–1695 (2008).

167. Barnes, S. E., Cygan, Z. T., Yates, J. K., Beers, K. L. & Amis, E. J. Raman spectroscopic monitoring of droplet polymerization in a microfluidic device. *Analyst* **131**, 1027–1033 (2006).

168. Meier, T. A. *et al.* On-chip monitoring of chemical syntheses in microdroplets via surface-enhanced Raman spectroscopy. *Chem. Commun.* **51**, 8588–8591 (2015).

169. Yue, S., Ye, W. & Xu, Z. SERS monitoring of the Fenton degradation reaction based on microfluidic droplets and alginate microparticles. *Analyst* **144**, 5882–5889 (2019).

170. Strehle, K. R. *et al.* A reproducible surface-enhanced Raman spectroscopy approach. Online SERS measurements in a segmented microfluidic system. *Anal. Chem.* **79**, 1542–1547 (2007).

171. Yu, Z. *et al.* Droplet-based microfluidic analysis and screening of single plant cells. *PLoS One* **13**, (2018).

172. Best, R. J. *et al.* Label-Free Analysis and Sorting of Microalgae and Cyanobacteria in Microdroplets by Intrinsic Chlorophyll Fluorescence for the Identification of Fast Growing Strains. *Anal. Chem.* **88**, 10445–10451 (2016).

173. Wyatt Shields Iv, C., Reyes, C. D. & López, G. P. Microfluidic cell sorting: A review of the advances in the separation of cells from debulking to rare cell isolation. *Lab on a Chip* **15**, 1230–1249 (2015).

174.   Wang, B. L. *et al.* Microfluidic high-throughput culturing of single cells for selection based on extracellular metabolite production or consumption. *Nat. Biotechnol.* **32**, 473–478 (2014).

175.   Mazutis, L. *et al.* Single-cell analysis and sorting using droplet-based microfluidics. *Nat. Protoc.* **8**, 870–891 (2013).

176.   Autebert, J. *et al.* Microfluidic: An innovative tool for efficient cell sorting. *Methods* **57**, 297–307 (2012).

177.   Gach, P. C. *et al.* A Droplet Microfluidic Platform for Automating Genetic Engineering. *ACS Synth. Biol.* **5**, 426–433 (2016).

178.   Lim, J. W., Shin, K. S., Moon, J., Lee, S. K. & Kim, T. A Microfluidic Platform for High-Throughput Screening of Small Mutant Libraries. *Anal. Chem.* **88**, 5234–5242 (2016).

179.   Huebner, A. *et al.* Quantitative detection of protein expression in single cells using droplet microfluidics. *Chem. Commun.* 1218–1220 (2007). doi:10.1039/b618570c

180.   Martin, K. *et al.* Generation of larger numbers of separated microbial populations by cultivation in segmented-flow microdevices. *Lab Chip* **3**, 202–207 (2003).

181.   Terekhov, S. S. *et al.* Microfluidic droplet platform for ultrahigh-throughput single-cell screening of biodiversity. *Proc. Natl. Acad. Sci. U. S. A.* **114**, 2550–2555 (2017).

182.   Oh, H. J., Kim, S. H., Baek, J. Y., Seong, G. H. & Lee, S. H. Hydrodynamic micro-encapsulation of aqueous fluids and cells via 'on the fly' photopolymerization. *J. Micromechanics Microengineering* **16**, 285–291 (2006).

183.   He, M. *et al.* Selective encapsulation of single cells and subcellular organelles into picoliter- and femtoliter-volume droplets. *Anal. Chem.* **77**, 1539–1544 (2005).

184.   Sakai, S., Kawabata, K., Ono, T., Ijima, H. & Kawakami, K. Higher viscous solution induces smaller droplets for cell-enclosing capsules in a co-flowing stream. *Biotechnol. Prog.* **21**, 994–997 (2005).

185.   Cecchini, M. P. *et al.* Ultrafast surface enhanced resonance raman scattering detection in droplet-based microfluidic systems. *Anal. Chem.* **83**, 3076–3081 (2011).

186.   Davidson, M. W. Resolution. *Nikon's Microsc.*

187.   Pan, J. *et al.* Quantitative tracking of the growth of individual algal cells in microdroplet compartments. *Integr. Biol.* **3**, 1043–1051 (2011).

188. Barrow, S. J., Kasera, S., Rowland, M. J., Del Barrio, J. & Scherman, O. A. Cucurbituril-Based Molecular Recognition. *Chem. Rev.* **115**, 12320–12406 (2015).

189. Yu, Z. *et al.* Supramolecular hydrogel microcapsules via cucurbit[8]uril host-guest interactions with triggered and UV-controlled molecular permeability. *Chem. Sci.* **6**, 4929–4933 (2015).